

Influence of the Channelrhodopsin-2 Distribution on Optogenetic Excitability in a CA1 Pyramidal Neuron

Maren Baltussen

Student number: 01702039

Supervisors: Prof. dr. ir. Emmeric Tanghe, Prof. dr. ir. Wout Joseph
Counsellors: Ir. Ruben Schoeters, Dr. ir. Thomas Tarnaud

Master's dissertation submitted in order to obtain the academic degree of
Master of Science in Biomedical Engineering

Academic year 2021-2022

Influence of the Channelrhodopsin-2 Distribution on Optogenetic Excitability in a CA1 Pyramidal Neuron

Maren Baltussen

Student number: 01702039

Supervisors: Prof. dr. ir. Emmeric Tanghe, Prof. dr. ir. Wout Joseph
Counsellors: Ir. Ruben Schoeters, Dr. ir. Thomas Tarnaud

Master's dissertation submitted in order to obtain the academic degree of
Master of Science in Biomedical Engineering

Academic year 2021-2022

Acknowledgements

Throughout my master's degree, neuro-engineering science has always piqued my curiosity. The complexity of our brain is endless, however neuroscience advances and step by step, the mystery of the brain is unravelled. Optogenetics, in particular, is in my opinion a very promising technique which has a lot of potential in further examining the brain. I am very glad to be a little part of the research of optogenetics. Most importantly, I want to thank Ruben Schoeters and Thomas Tarnaud for guiding me throughout my thesis. Our weekly meetings helped me forward and new challenges were brought up. They steered me in the right direction and enriched my thesis with their advice. Prof. dr. ir. Emmeric Tanghe and prof. dr. ir. Wout Joseph made this research possible and allowed me to work on this subject, for which I am very thankful.

I want to thank my sister, Liesje Baltussen, and friend, Vita De Vos, for reading my thesis and correcting the typos. Furthermore, I want to thank my roommates, Kaat and Sofie, for listening to me, supporting me, and entertaining me in my study breaks.

Finally, a special thanks to Lydie Bekaert, who accompanied me in the journey of biomedical engineering. I will always remember the beautiful years we had, sometimes struggling, but mostly with a lot of joy.

Permission for usage

The author gives permission to make this master dissertation available for consultation and to copy parts of this master dissertation for personal use.

This master's dissertation is part of an exam. Any comments formulated by the assessment committee during the oral presentation of the master's dissertation are not included in this text.

Maren Baltussen, June 2022

Abstract

The influence of the Channelrhodopsin-2 variant ChR2(H134R) distribution on the optogenetic excitability in a CA1 pyramidal neuron is studied in this dissertation. An extensive comparison is made between the response of this neuron on optogenetic stimuli for different ChR2(H134R) distributions in view of finding distributions that will improve the efficiency and selectivity of the optogenetic stimulation. The neuronal response is computationally obtained by combining a model of ChR2(H134R) and a CA1 pyramidal neuron model. ChR2(H134R) was modeled by the double two-state model of Schoeters et al. (2021). Two neuron models of different complexities are used to model the neuron: a modified version of the reduced-morphology model of Cutsuridis and Poirazi (2015) by Tomko et al. (2021) (CP15TK21 model) and the full-morphology model of Migliore et al. (2018) (M18 model). This was done to investigate the impact of the neuronal model's complexity on the obtained results. For both models, the results show that an optogenetic stimulation of the apical dendritic tuft region leads to the highest mean firing rates measured in the soma.

Keywords Optogenetics, CA1 pyramidal neuron, Channelrhodopsin-2 distribution, computational study

Influence of the Channelrhodopsin-2 Distribution on Optogenetic Excitability in a CA1 Pyramidal Neuron

Maren Baltussen

Supervisors: Prof. dr. ir. Emmeric Tanghe, Prof. dr. ir. Wout Joseph

Counsellors: Ir. Ruben Schoeters, Dr. ir. Thomas Tarnaud

The influence of the Channelrhodopsin-2 variant ChR2(H134R) distribution on the optogenetic excitability in a CA1 pyramidal neuron is studied. An extensive comparison is made between the response of this neuron on optogenetic stimuli for different ChR2(H134R) distributions in view of finding distributions that will improve the efficiency of the optogenetic stimulation. The neuronal response is computationally obtained by combining a model of ChR2(H134R) and a CA1 pyramidal neuron model. ChR2(H134R) was modeled by the double two-state model of Schoeters et al. (2021). Two neuron models of different complexities are used to model the neuron: a modified version of the reduced-morphology model of Cutsuridis and Poirazi (2015) by Tomko et al. (2021) (CP15TK21 model) and the full-morphology model of Migliore et al. (2018) (M18 model). This was done to investigate the impact of the neuronal model's complexity on the obtained results. For both models, the results show that an optogenetic stimulation of the apical dendritic tuft region leads to the highest mean firing rates measured in the soma.

Keywords: Optogenetics, CA1 pyramidal neuron, Channelrhodopsin-2 distribution, computational study

Yearly, millions of people are affected by neurological diseases like epilepsy, schizophrenia, and Parkinson's disease. Some of them do not react to pharmacological treatment, others are not eligible for resection (Tønnesen and Kokaia, 2017; White et al., 2020). Optogenetics is a promising brain stimulation technique in which molecules are genetically expressed in target cells with the aim of controlling their activity by exposing them to pulses of appropriate wavelengths (He, 2020). The main advantages over other neurological techniques are the cell-type specificity and a higher spatiotemporal resolution (Tønnesen and Kokaia, 2017). However, clinical trials for the use of optogenetics within the brain still face a lot of challenges (White et al., 2020). Here we aimed at finding optogenetic stimulation strategies that can improve the efficiency of optogenetic excitation of the CA1 pyramidal neuron. In this computational study, the well-known Channelrhodopsin-2 variant ChR2(H134R) is expressed on six different locations across the neuron: the soma, the axon, a basal dendrite section, an apical trunk section, a radial oblique dendrite section, and an apical dendritic tuft section. The opsin is modeled by the double two-state opsin model of (Schoeters et al., 2021) because of its high precision simulations and computational speed. This model was already fitted to and tested on ChR2(H134R). Two neuron models of different complexities are used to model the CA1 pyramidal neuron: a modified version of the reduced-morphology model of Cutsuridis and Poirazi (2015) by Tomko et al. (2021) (CP15TK21 model) and the full-morphology model of Migliore et al. (2018) (M18 model). The models are implemented in the NEURON simulation platform (Carnevale and Hines, 2006). A comparative analysis is done of the cell response on optogenetic stimulations with different opsin distributions and subsequently compared for both neuronal models.

METHODS

Neuron model of Cutsuridis and Poirazi by Tomko

The first neuronal model that is used to model the CA1 pyramidal neuron is the reduced-morphology model of Cutsuridis and Poirazi (2015) modified by Tomko et al. (2021) (CP15TK21). A representation of the morphology is shown in Figure 1, together with the names of the nine sections on which the opsin will be expressed. These are inspired by the corresponding sublayer of the cornu ammonis, one of the main zones of the hippocampus, in which they are located. The morphology is symmetric and the right and left side are respectively indicated by suffix one and two.

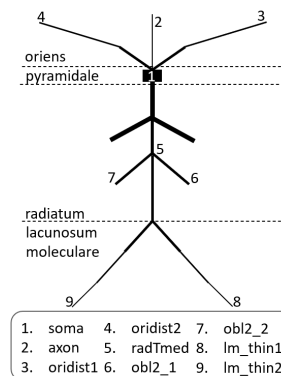


Figure 1: CA1 pyramidal neuron morphology of the CP15TK21 model with the corresponding section names (Cutsuridis and Poirazi, 2015).

The original model of Cutsuridis and Poirazi (2015) (CP15) had a low excitability, which was not ideal in the analysis of the subcellular optogenetic stimulation effects. Recently, Tomko et al. (2021) proposed to replace the content of the ion channels with those of the full-morphology model of Migliore et al. (2018). This new model, CP15TK21, was more ex-

citable, had improved physiological properties, and was able to capture key physiological features of CA1 pyramidal neurons. It can be found on modelDB¹. The neuron includes eleven active conductances: a voltage gated Na⁺ conductance (G_{Na}), a delayed rectifier K⁺ conductance (G_{Kdr}), two A-type K⁺ conductances (G_{Ka}), an M-type K⁺ conductance (G_{Kmb}), a H conductance (G_{Hd}), two Ca²⁺-activated K⁺ (G_{Kca}) conductances, three Ca²⁺ conductances (G_{Ca}), and a calcium accumulation mechanism. The currents are described according to the Hodgkin-Huxley model. All sections containing calcium channels also include a simple calcium accumulation mechanism, with a single exponential decay of 100 ms (Migliore et al., 2018).

Neuron model of Migliore et al.

A second, more complex model was used to study the effects of the morphological complexity on the results: the model of Migliore et al. (2018) (M18). This model can be found on modelDB under accession number 244688. The 165 sections compared to the 19 sections of CP15TK21 make it a morphological realistic model. Both models can be compared in Figure 2. However, the computational time increases with complexity. The biophysics of M18 are similar to those of CP15TK21.

Uniform distribution

A characteristic of the ChR2(H134R) channel is its adaptation to both light and darkness. Light adapted molecules have a lower conductance than dark adapted ones. In the double two-state model of Schoeters et al. (2021) \bar{g}_{ChR2} is the maximal specific conductance in mS/cm² of a fully dark adapted channel. The opsin distribution can be controlled by adapting this parameter. It can be seen as the opsin density. The higher the maximal specific conductance, and the higher the transmembrane current for a certain optogenetic stimulus intensity (I) and pulse duration (PD).

Simulations were done via the NEURON simulation platform (Carnevale and Hines, 2006). The opsin model is inserted in the CP15TK21 model and implemented in the NEURON 8.0.0 environment in Python 3.7.11. In each simulation, the opsin is expressed on a different section, also called stimulation location. These include the soma (1), the axon (2), a basal dendritic section (3 or 4), an apical trunk section (5), a radial oblique section (6 or 7), and an apical dendritic tuft section (8 or 9). If the opsin is simultaneously expressed on the symmetrical sections (e.g. oridist1 and oridist2), it will be referred to by the same name without suffix (e.g. 'oridist'). In order to compare the optogenetic stimulation of locations with different surface areas, the maximal specific conductance is scaled according to Eq. 1, with the soma as reference. This ensures an equal maximal conductance (\bar{G}_{ChR2}) for all

stimulation locations.

$$\bar{g}_{ChR2,section} = \bar{g}_{ChR2,soma} \frac{A_{soma}}{A_{section}} \quad (1)$$

With A_{soma} and $A_{section}$ the surface area of respectively the soma and the section for which the maximal specific conductance is scaled.

Gaussian distribution

Section	Reference point	M18		Reference Point(s)	CP15TK21	
		μ (μ m)	σ (μ m)		μ (μ m)	σ (μ m)
soma	soma	0	25	soma	0	25
axon	axon	0	75	axon	0	125
oridist	soma	285.00	75	oridist	0	100
radTmed	soma	188.33	25	radTmed	0	50
obl2	soma	288.33	25	obl2	0	75
lm_thin	soma	630.00	25	lm_thin	0	100

Table I: The mean (μ) and standard deviation (σ) used for the normal distribution of the maximal specific conductance of ChR2(H134R) in M18 and CP15TK21, corresponding with the stimulation locations.

For the full-morphology model (M18), it is not useful to look at separate sections as was done for the CP15TK21 model since there are 165 sections. The maximal specific conductance now follows a normal distribution in function of the distance to a reference point. The general form of a Gaussian probability density function is given by:

$$\bar{g}_{ChR2}(x) = \bar{g}_{ChR2,max} \cdot e^{-\frac{1}{2} \left(\frac{x-\mu}{\sigma} \right)^2} \quad (2)$$

with x the path distance between the segment for which \bar{g}_{ChR2} is determined and the reference point, not the distance between the vectors. For reasons elaborated on later, the soma is the reference point for all stimulation location except of the axon. There are two parameters: the mean (μ) and the standard deviation (σ). The mean of the distribution is the distance to the reference point where $\bar{g}_{ChR2}(\mu) = \bar{g}_{ChR2,max}$. To target similar locations as in CP15TK21, the distances to the soma of the stimulation locations of CP15TK21 are determined and used as mean values for the corresponding stimulation locations of M18. They can be found in Table I. $\bar{g}_{ChR2,max}$ is defined such that all stimulation locations have an equal maximal conductance (\bar{G}_{ChR2}) for all locations:

$$\bar{g}_{ChR2,max} = \frac{\bar{G}_{ChR2}}{\sum_{sec} \sum_{seg} e^{-\frac{1}{2} \left(\frac{x-\mu}{\sigma} \right)^2} \cdot \frac{A_{sec}}{n_{seg}}} \quad (3)$$

Where the sum is evaluated for all segments of the 165 sections and x is the distance between the segment and the reference point. A_{sec} is the surface area of the section and n_{seg} the number of segments in that section.

¹ <https://github.com/tomko-neuron/HippoUnit>

The axon is a special case, because it is one specific part of the neuron. Applying the same methodology as for the other sections results in a high \bar{g}_{ChR2} in all basal and apical sections at the same distance from the soma as the axon, which is not desired. To solve this, the axon itself is used as reference point and μ is set to zero. So, x is now the distance between the segment in question and the axon. The standard deviations were chosen such that the maximal specific conductance is within the range of 0-200 mS/cm² for $\bar{G}_{\text{ChR2,desired}} = 0.7\pi \mu\text{S}$. Table I lists the chosen standard deviation for every stimulation location. In the following, the same names as used for the stimulation locations of CP15TK21 will be designated to the corresponding stimulation locations of M18.

The transition to a normal distributed maximal specific conductance is also made for CP15TK21. A similar methodology as for the axon is used, i.e. the section itself as reference point and a mean of zero. The distance between the section itself and the segment in question is x . The standard deviations are again adapted for every case in order to have similar \bar{g}_{ChR2} ranges. The values can be found in Table I. The Gaussian maximal specific conductance distribution around an apical trunk dendrite (radTmed) is plotted for both models in Figure 2.

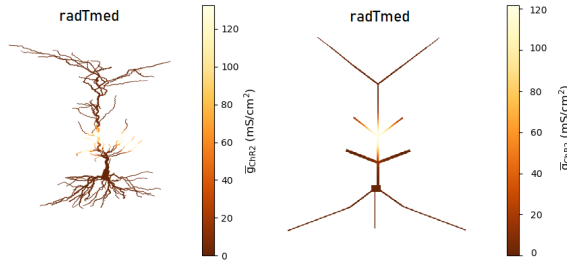


Figure 2: Distribution of the maximal specific conductance for an apical trunk stimulation (radTmed) for the M18 (left) and CP15TK18 (right) model. A desired maximal conductance of $0.7\pi \mu\text{S}$ was used. The maximal specific conductance follows a normal distribution with parameters μ, σ , given in Table I, and scalingsfactor C.

RESULTS

Uniform distribution

The opsin is consecutively inserted in the soma, axon, oridist1, radTmed, obl2_1, and lm_thin1. It is uniformly distributed along the section. The mean firing rate (FR) is defined as the number of peaks measured during the stimulation time, divided by the pulse duration (PD). It is calculated for a set of optogenetic pulse intensities and maximal specific conductances of the ChR2(H134R) channel with a pulse duration of 500 ms. The results are visualized in 2D colorplots in Figure 3.

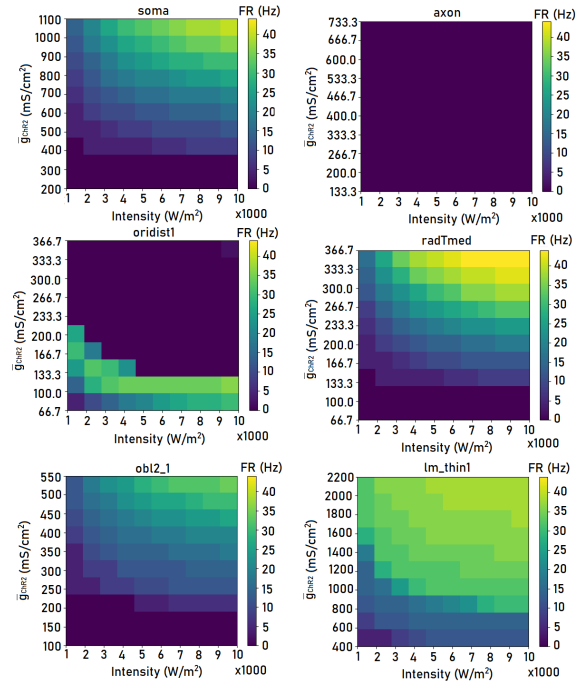


Figure 3: 2D colorplots of the mean firing rate in function of the optogenetic pulse intensity and maximal specific conductance of ChR2(H134R). A continuous pulse of 500 ms is used. The mean firing rates are recorded in the soma and the opsin is uniformly distributed along the indicated section of CP15TK21.

The sections have different values on the y-axis because of the surface area scaling factor (Eq. 1). In general, the mean firing rate increases for increasing values of intensity and maximal specific conductance. Placement of the opsin in the axon gives zero mean firing rates for all intensities and maximal conductances, while the membrane potential is at a constant depolarized level (see also Figure 4 b)). The same is observed for oridist1 for maximal specific conductances above 133.3 mS/cm². This phenomenon is described as a depolarization block. Lastly, a remarkably higher mean firing rate is observed for lm_thin1 compared to obl2_1.

The mean firing rate reveals only a part of the membrane potential trace. Figure 4 shows the membrane potential traces for $I = 10000 \text{ W/m}^2$ and $\bar{G}_{\text{ChR2}} = 0.5\pi \mu\text{S}$. The optogenetic pulse is continuous with a duration of 500 ms. The upper plot consists of the sections in which more than one action potential (AP) was measured. Targeting of the soma, the apical trunk dendrite (radTmed) and the radial oblique dendrite (obl2_1) results in an equal spiking pattern. The optogenetic pulse is characterized by an initial peak current. This is reflected in the initial burst seen in the spiking pattern for the different sections. Thereafter, the neuron adjusts until a steady-state is reached. If the steady-state optogenetic current is sufficient, a continuous firing is observed. The higher the pulse intensity and conductance of the opsin channel, the more current injection and the shorter the period of silence in

between the initial burst and the steady-state continuous firing. The firing rate increases. *Im_thin1* has a remarkably higher equilibrium potential and an increased mean firing rate compared to the other stimulation locations. The membrane potentials of the other two sections are shown in Figure 4 (b). Stimulation of both sections results in one AP, followed by a depolarized membrane potential during the stimulus time.

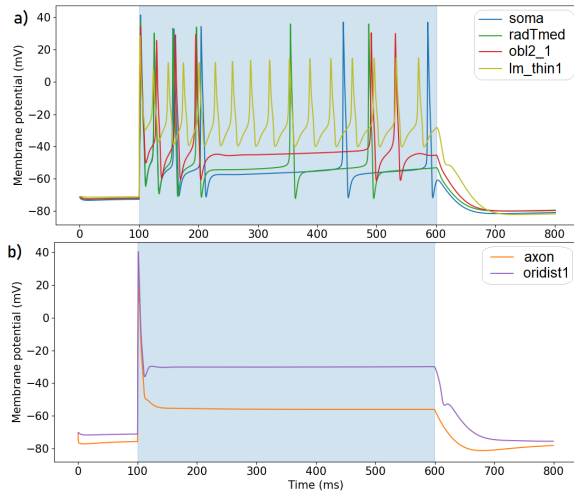


Figure 4: The membrane potential trace for a continuous optogenetic pulse of 500 ms and 10000 W/m^2 (blue area). The opsin is located in the section indicated in the legend with a maximal Chr2(H134R) conductance of $0.5\pi \mu\text{S}$. The membrane potential is measured at the center of this section. The sections for which more than one AP was measured are plotted in (a), the others in (b).

In a second test, the opsin was placed in both symmetrical sections and the mean firing rate was similarly determined. For example, *oridist1* and *oridist2* are both targeted instead of only *oridist1*. The results were mostly similar. Most importantly, the increased FR that was observed for *Im_thin1* is even more pronounced when both *Im_thin1* and *Im_thin2* are targeted.

Normally, excitatory postsynaptic potentials (EPSPs) from different synapse inputs are integrated at the soma and can result in an action potential. It is also possible that the action potential was actually initiated in the dendrite, which is called a dendritic action potential. In order to investigate the AP initiation, the time of the first AP in the soma and stimulation location are compared and the delay is calculated. Figure 5 shows the result. The pulse intensity and maximal conductance have limited impact on the delay. All delays are positive, leading to the conclusion that the action potential is initiated at the stimulation location. The observations are expandable to all observed action potentials. The spiking pattern measured at the soma resembles the spiking pattern measured at the stimulation location, with a slight delay due to the propagation of the action potential. If the stimulation location is distinct from the soma and axon, we can say that the

measured spikes are dendritic spikes. Figure 4 (a) illustrates one of the characteristics of dendritic spikes: a more depolarized action potential voltage threshold compared to the soma (Gasparini, 2004).

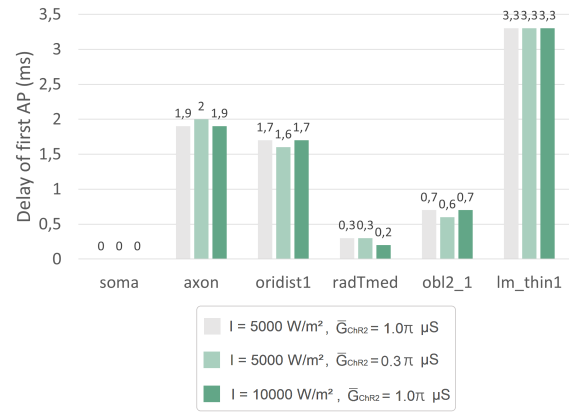


Figure 5: Delay between an AP measured in the indicated section and in the soma. The opsin is located in the same section. The optogenetic pulse is continuous with a pulse duration of 500 ms. The indicated values are used for the pulse intensity and Chr2(H134R) maximal conductance.

Another way to compare different locations is by comparing their strength-duration curves. The rheobase intensities and strength-duration time constants are calculated for the different opsin locations in function of the maximal conductance and plotted in respectively Figure 6 (a) and (b). The strength-duration time constant is determined as follows:

$$\tau_{SD} = \frac{I[0] \cdot PD[0]}{I_{RH}} \quad (4)$$

With $PD[0]$ the shortest pulse duration, $I[0]$ the corresponding intensity, and I_{RH} the rheobase. All recordings were done in the soma. Strength-duration curves reveal information about the excitability of a stimulation location. Optogenetic stimulation of a distal basal dendrite (*oridist1*) or apical dendritic tuft dendrite (*Im_thin1*) result in rheobases that are on average 79% lower than those obtained for the other sections. These two sections are therefore more excitable and will trigger a somatic AP already for lower pulse intensities. The other four sections have comparable strength-duration time constants but their rheobase differ. The highest rheobase and lowest strength-duration time constant is observed when the opsin is located in the axon. For all sections applies that a higher maximal conductance decreases the rheobase because a higher maximal conductance means that for the same optogenetic pulse intensity, more current is injected into the section. An AP will thus be evoked for lower optogenetic intensities. The increasing strength-duration time constant is slightly more complex to understand. In Eq. 4 $PD[0]$, the shortest pulse duration, remains

unchanged. I_{RH} and $I[0]$, the intensity corresponding with the smallest pulse duration, will both decrease so an increasing strength-duration time constant learns us that the rheobase decreases slower than $I[0]$. So a higher ChR2(H134R) maximal conductance will have more impact on the pulse intensity necessary to generate an AP for small pulse duration than for long pulse durations. It is observed that the strength-duration curves of *oridist1* and *lm_thin1* intersect for pulse durations around 20 ms, for both small and large maximal conductances. This indicates that *lm_thin1* is more excitable for smaller pulse durations, *oridist1* for larger pulse durations. All the other strength-duration curves do not intersect, independent of \bar{G}_{ChR2} .

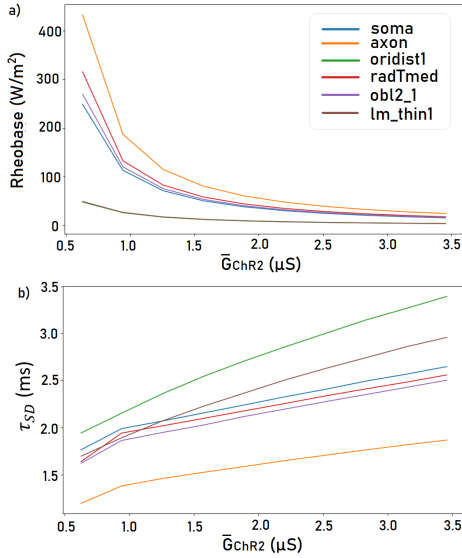


Figure 6: Plot (a) represents the rheobase calculated for the different opsin locations in function of the maximal conductance. The strength-duration time constant in function of the maximal conductance is visualised in the plot (b).

Gaussian distribution

The transition from a normal to a Gaussian ChR2(H134R) distribution for CP15TK21 resulted in a different behavior upon an axonal stimulation. Instead of a depolarization block, FR increases with an increasing optogenetic pulse intensity and maximal conductance. It reaches a mean firing rate of 38 Hz. The absence of the depolarization block can be explained by the lower maximal specific conductances. The stimulation is more distributed, resulting in a smaller injected current. All the other observations made in the case of a uniform distribution, can be copied. The same 2D colorplots were generated for the full-morphology model of Migliore et al. (2018) and shown in Figure 7. In general, M18 is a more excitable model, leading to higher firing rates for equal optogenetic stimulations. For higher pulse intensities and maximal conductances, stimulation of apical trunk

(radTmed) and oblique radial dendrites (*obl2*) leads to a FR of 42 Hz. There is no further increase. Most importantly, the complexity of the morphology did not influence the main observation: a higher firing rate is measured in the soma in case of apical dendritic tuft (*lm_thin1*) stimulation. This means that this result is independent of the complexity of the model and is likely to be observed in other models.

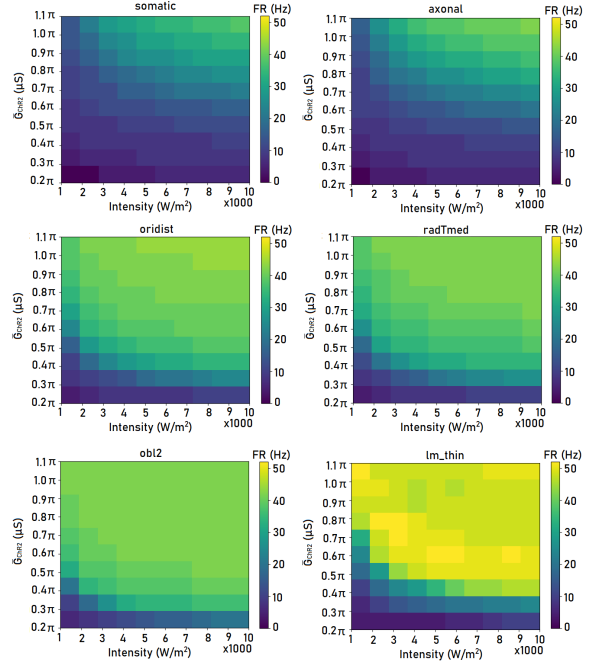


Figure 7: 2D colorplots of the mean firing rate in function of the optogenetic pulse intensity and maximal specific conductance of ChR2(H134R). A continuous pulse of 500 ms is used. The mean firing rates are recorded in the soma. The M18 model was used as neuronal model with a normally distributed maximal opsin conductance around the indicated location.

DISCUSSION

The mean firing rates showed how stimulation of distal dendritic tuft sections (*lm_thin*) leads to a higher mean firing rate compared to the other locations, almost independent of the optogenetic pulse intensity, maximal specific conductance of the opsin channel, and the complexity of the neuronal model. Positive AP delays showed that the spikes are initiated at the stimulation location, also called dendritic spikes. Jarsky et al. (2005) studied the dendritic spike propagation following a distal synaptic activation of hippocampal CA1 pyramidal neurons. They found that somatic APs could only be initiated when the input resulted in the generation of dendritic spikes. EPSPs are attenuated during their propagation to the soma and have a limited ability to trigger somatic APs. Their conclusions were confirmed by experimental results. Remarkably, Jarsky et al. (2005) also observed that in models with

strongly excitable dendrites, the apical dendritic tuft input (perforant-path input) is more efficacious than upper apical dendritic inputs (Schaffer-collateral input), in that a lower number of inputs are necessary to trigger a spike. Both CP15TK21 and M18 are assumed to be classified as strong dendritic excitable models because almost all measured dendritic spikes could propagate to the soma and trigger a somatic spike. Tomko et al. (2021) also describes how M18, of which the biophysics are adopted for CP15TK21, is a strongly-propagating model based on the weak attenuation of back-propagating action potentials. Similar observations are made in this study by the fact that a higher mean firing rate is measured in the soma when the opsin is located in the apical dendritic tuft region. According to Jarsky et al. (2005), this can be explained by the high input impedance of the small-diameter tuft branches. Measurements of the input impedances gave different results for CP15TK21 and M18. Using CP15TK21, the highest input impedances were measured in the soma and radTmed, which contradicts the assumption of Jarsky et al. (2005) because they have the largest diameters. However, using M18, the input impedances of the small diameter apical dendritic tuft en distal basal dendritic section were indeed elevated compared to the others. The input impedance is therefore expected to play a role in the efficacious stimulation of the small-diameter branches but combined with other factors.

FUTURE WORK

Only one type of optogenetic stimulus was used in this dissertation: a continuous optogenetic pulse of 500 ms. Multiple pulse intensities were used but the pulse duration was kept fixed for all tests. Important to note is that the observed location-dependent effects are likely to be a results of the characteristics of dendritic spikes. If the optogenetic pulse would only evoke sub-threshold EPSPs in the apical dendritic tuft region, they would be attenuated during their propagation to the soma and the efficacious apical tuft stimulation is no longer applicable. Therefore, the type, spatial extent, duration, and intensity of the optogenetic pulse necessary to generate dendritic spikes could be an interesting new field of study.

CONCLUSION

Optogenetic stimulation strategies, characterized by the opsin distribution, were searched that could improve the efficiency of optogenetic excitation of the CA1 pyramidal neuron. A comparison of six stimula-

tion locations led to the conclusion that the symmetrical apical dendritic tuft stimulation resulted in the most efficient excitation of the soma. Similar effects were observed with a morphological more complex model.

References

- Carnevale, N. T. and Hines, M. L. (2006). *The NEURON Book*. Cambridge University Press.
- Cutsuridis, V. and Poirazi, P. (2015). A computational study on how theta modulated inhibition can account for the long temporal windows in the entorhinal-hippocampal loop. *Neurobiology of Learning and Memory*, 120:69–83.
- Gasparini, S. (2004). On the Initiation and Propagation of Dendritic Spikes in CA1 Pyramidal Neurons. *Journal of Neuroscience*, 24(49):11046–11056.
- He, B., editor (2020). *Neural Engineering*. Springer International Publishing, Cham.
- Jarsky, T., Roxin, A., Kath, W. L., and Spruston, N. (2005). Conditional dendritic spike propagation following distal synaptic activation of hippocampal CA1 pyramidal neurons. *Nature Neuroscience*, 8(12):1667–1676.
- Migliore, R., Lupascu, C. A., Bologna, L. L., Romani, A., Courcol, J.-D., Antonel, S., Geit, W. A. H. V., Thomson, A. M., Mercer, A., Lange, S., Falck, J., Rössert, C. A., Shi, Y., Hagens, O., Pezzoli, M., Freund, T. F., Kali, S., Muller, E. B., Schürmann, F., Markram, H., and Migliore, M. (2018). The physiological variability of channel density in hippocampal CA1 pyramidal cells and interneurons explored using a unified data-driven modeling workflow. *PLoS Computational Biology*, 14(9):e1006423. Publisher: Public Library of Science.
- Schoeters, R., Tarnaud, T., Martens, L., Joseph, W., Raedt, R., and Tanghe, E. (2021). Double Two-State Opsin Model With Autonomous Parameter Inference. *Frontiers in Computational Neuroscience*, 15.
- Tomko, M., Benuskova, L., and Jedlicka, P. (2021). A new reduced-morphology model for CA1 pyramidal cells and its validation and comparison with other models using HippoUnit. *Scientific Reports*, 11(1):7615.
- Tønnesen, J. and Kokaia, M. (2017). Epilepsy and optogenetics: can seizures be controlled by light? *Clinical Science*, 131(14):1605–1616.
- White, M., Mackay, M., and Whittaker, R. G. (2020). Taking Optogenetics into the Human Brain: Opportunities and Challenges in Clinical Trial Design. *Open Access Journal of Clinical Trials*, Volume 12:33–41.

Contents

Acknowledgements	i
Permission for usage	ii
Abstract	iii
Extended abstract	ix
Contents	x
List of Figures	xii
List of Tables	xvi
List of Abbreviations	xvii
1 Introduction	1
2 Computational neurophysiology	3
2.1 Neurophysiology	3
2.1.1 Hippocampal CA1 neuron	5
2.2 Neuron models	8
2.2.1 Integrate-and-fire model	8
2.2.2 Hodgkin-Huxley model	10
2.3 Multi-compartment models	13
3 Optogenetics	16
3.1 Microbial opsins	16
3.1.1 Channelrhodopsin-2	18
3.1.2 Computational optogenetics	19
3.2 Subcellular optogenetics	20
3.3 Hurdles of optogenetics	22
4 Reduced-morphology neuron model	24
4.1 Cutsuridis and Poirazi model by Tomko: CP15TK21	24
4.2 ChR2(H134R) model: double two-state opsin model	27
4.3 Methodology	30
4.3.1 Stimulation strategies	31
4.3.2 Features	31
4.4 Results	34
4.5 Discussion	42

5 Morphologically simple versus complex neuronal model	45
5.1 Migliore 2018: M18	45
5.2 Methodology	46
5.2.1 Stimulation strategies	46
5.3 Results	49
5.4 Discussion	54
6 Conclusion	55
6.1 Future work	56
A Supplementary tables	58
B Ethics and scientific integrity	60
Bibliography	62

List of Figures

2.1	Single neuron in a drawing by Ramón y Cajal. The basic elements are shown: dendrite, soma, and axon (Gerstner et al., 2014).	3
2.2	Multiple phospholipids forming a cell membrane (Petersen, 2016).	4
2.3	A hippocampal CA1 neuron. Typically contains apical and basal dendrites and has a pyramidal shaped soma. (Georgiev, 2009)	6
2.4	Hippocampus with 3 main zones: dentate gyrus, cornu ammonis, and subiculum. Pyramidal cells are organized in zones CA1, CA2, CA3 and CA4. The cornu ammonis has five sublayers as explained in text (medical dictionary: https://medicine.en-academic.com/3923).	7
2.5	Left: Electrical equivalent of the neuron for a LIF model. $I(t)$ represents the input current, $V(t)$ the membrane potential. The cell membrane acts as a capacitor with capacity C . There is an Ohmic leakage current with resistance R which is in line with a battery of potential V_{rest} (Gerstner et al., 2014). Right: Membrane potential in function of time given by the leaky integrate-and-fire model (solid line) compared to a normal action potential (dashed line). After crossing the firing threshold θ at time t_i , a spike is generated and the membrane potential is reset to the potential V_r (Gerstner et al., 2014).	9
2.6	The equivalent circuit corresponding with the Hodgkin-Huxley model (Gerstner et al., 2014).	11
2.7	Left: the steady-state (in)activation functions x_∞ in function of the membrane voltage. Right: the time constants τ_x in function of the membrane voltage (Gerstner et al., 2014).	12
2.8	Different stages of an action potential in the Hodgkin-Huxley model (Izhikevich, 2006).	12
2.9	Simplification of a neuronal section with corresponding circuit diagram. R_L , and R_T are the longitudinal and transversal resistors, respectively. Capacitor C is the electrical capacity (Gerstner et al., 2014).	14
2.10	Replacement of a neuronal structure (a) by a multi-compartment model (b). (c) A 2-compartment model with membrane potential V_d and V_s in the dendrite and soma, respectively (Izhikevich, 2006).	15
3.1	Visualisation of excitatory Channelrhodopsin (ChR) and inhibitory Halorhodopsin (HR) (Fenno et al., 2011).	17
3.2	The opening-and-closing mechanism of the ChR2 protein. All- <i>trans</i> -retinal transforms after electron-photon interaction into the high-energy 13- <i>cis</i> -retinal. As a results the channel opens. The high-energy retinal returns to the all- <i>trans</i> state in the absence of light. The channel closes (He, 2020).	18

3.3	The time course of the ChR2 current as a response on light stimulation (blue line) obtained from experimental observations. Five parameters capture the amplitude and kinetics from the ChR2 current: the peak current I_p and the steady-state current I_{ss} . τ_{on} , τ_{off} , and τ_{inact} are the activation, deactivation, and inactivation time constants, respectively (Williams et al., 2013).	19
3.4	Three- (left) and four-(right) state models for the photocycle of ChR2. Different states are O(open), C(closed), D(desensitized). The four-state model consists of two open and two closed states. (Nikolic et al., 2009)	20
4.1	CA1 pyramidal neuron morphology of the CP15TK21 model with the corresponding section names (Cutsuridis and Poirazi, 2015; Tomko et al., 2021).	25
4.2	Double two-state opsin model (22OM) derived by Schoeters et al. (2021). The O-C state pair accounts for the open-closing mechanism. O and C respectively refer to open and close. Dark-light adaptation is captured by the mathematical R-S state pair. The light dependent rates are indicated by blue arrows. The ChR2 photocycle is visualised in the background.	28
4.3	The stimulation strategies used for the CP15TK21 model. Yellow sections indicate the consecutive locations of the ChR2(H134R) channel. The opsin is uniformly distributed along the section.	31
4.4	2D colorplots of the mean firing rate, calculated according to Eq. 4.30, in function of the optogenetic pulse intensity and maximal specific conductance of ChR2(H134R). A continuous pulse of 500 ms is used. The mean firing rates are recorded in the soma for each stimulation location of the diffuse neuronal stimulation strategy, indicated in the title of the surface plots.	34
4.5	The membrane potential (mV) in function of time (ms) for two different optogenetic stimuli. A continuous pulse with pulse duration 500 ms and intensity 5000 W/m^2 was used in a) and b) and is indicated as the blue area. The opsin is located in the section indicated in the legend with a maximal ChR2(H134R) conductance of $0.3\pi \mu\text{S}$. The membrane potential is measured at the center of this section. A similar optogenetic stimulus was used to obtain (c) and (d) but with a higher intensity (10000 W/m^2) and maximal opsin conductance ($0.5\pi \mu\text{S}$). The sections for which more than one AP was measured are plotted in (a) and (c), the others in (b) and (d).	35
4.6	Delay between an AP measured in the indicated section and in the soma. The opsin is located in the same section with a maximal conductance of $1.0\pi \mu\text{S}$, $0.3\pi \mu\text{S}$, and $1.0\pi \mu\text{S}$ for the grey, light green, and dark green bars, respectively. The respective optogenetic intensities are 5000 W/m^2 , 5000 W/m^2 , and 10000 W/m^2 . The optogenetic pulse is continuous with a pulse duration of 500 ms.	36
4.7	(a),(b) Strength-duration curve for different ChR2(H134R) locations and a maximal conductance of respectively $0.7\pi \mu\text{S} = 2.2 \mu\text{S}$ and $1.0 \mu\text{S}$, recorded in the soma. The optogenetic pulse duration (ms) of a continuous pulse is shown on the x-axis and the optical pulse intensity (W/m^2) on the y-axis. Plot (c) represents the rheobase (W/m^2) calculated for the different opsin locations in function of the maximal conductance (μS). The strength-duration time constant (ms) in function of the maximal conductance (μS) is visualised in the plot (d).	37
4.8	Input impedance measured at the indicated location in function of the frequency of the oscillatory current stimulus. It is measured 200 ms after the onset of the stimulus. The CP15TK21 neuron model was used.	38

4.9	2D colorplots of the mean firing rate, calculated according to Eq. 4.30, in function of the optogenetic pulse intensity and maximal specific conductance of ChR2(H134R). A continuous pulse of 500 ms is used. The mean firing rates are recorded in the soma for each stimulation location of the symmetric diffuse stimulation strategy, indicated in the title of the surface plots. Oridist refers to the two symmetrical sections: oridist1 and oridist2. Similarly, obl2 refers to obl2_1 and obl2_2 and lm_thin to lm_thin1 and lm_thin2.	39
4.10	The membrane potential (mV) in function of time (ms) with the opsin located in a single section (blue) and in the two corresponding symmetric sections (orange). In both cases, the membrane potential was measured in the section with suffix 1. A continuous optogenetic pulse of 500 ms and 5000 W/m^2 , and a maximal conductance of $0.3\pi \mu\text{S}$ was used in a), c), and e). For plot b), d), and f), an intensity of 10000 W/m^2 and a maximal conductance of $0.5\pi \mu\text{S}$ was used. The optogenetic pulse is indicated with the blue area.	40
4.11	2D colorplots of the mean firing rate, calculated according to Eq. 4.30, in function of the optogenetic pulse intensity and maximal specific conductance of ChR2(H134R). A continuous pulse of 500 ms is used. The mean firing rates are recorded in the soma. From left to right, the opsin is located in oridist1, oriprox1, and the soma.	40
4.12	The membrane potential (mV) in function of time (ms) with the opsin location indicated in the legend. The membrane potential is measured in the same section. A continuous optogenetic pulse of 500 ms and 5000 W/m^2 , and a maximal conductance of $0.3\pi \mu\text{S}$ was used in a). For plot b), an intensity of 10000 W/m^2 and a maximal conductance of $0.5\pi \mu\text{S}$ was used. The optogenetic pulse is indicated with the blue area.	41
4.13	Input impedance measured at a distal (oridist1) and proximal (oriprox1) basal dendritic section in function of the frequency of the oscillatory current stimulus. It is measured 200 ms after the onset of the stimulus. The CP15TK21 neuronal model is used.	41
5.1	CA1 pyramidal neuron morphology of the M18 model. The soma is the central yellow point, the axon is represented in green, the basal dendrites in blue, and the apical dendrites in red (Migliore et al., 2018).	45
5.2	Distribution of the maximal specific conductance for the different stimulation locations of M18 for a maximal conductance of $0.7\pi \mu\text{S}$. The names are derived from the corresponding stimulation locations of CP15TK21. Maximal specific conductance follows a normal distribution with parameters μ, σ , given in Table 5.1, and $\bar{g}_{\text{ChR2,max}}$ determined according to Eq. 5.3.	48
5.3	Distribution of the maximal specific conductance for the different stimulation locations of CP15TK21 for a maximal conductance of $0.7\pi \mu\text{S}$. Maximal specific conductance follows a normal distribution with parameters μ, σ , given in Table 5.1, and $\bar{g}_{\text{ChR2,max}}$ determined according to Eq. 5.3.	49
5.4	2D colorplots of the mean firing rate, calculated according to Eq. 4.30, in function of the optogenetic pulse intensity and maximal conductance of ChR2(H134R). A continuous pulse of 500 ms is used. The firing rates are recorded in the soma. The CP15TK21 model was used as neuronal model with a normally distributed maximal opsin conductance around the indicated location.	49
5.5	2D colorplots of the mean firing rate, calculated according to Eq. 4.30, in function of the optogenetic pulse intensity and maximal conductance of ChR2(H134R). A continuous pulse of 500 ms is used. The mean firing rates are recorded in the soma. The M18 model was used as neuronal model with a normally distributed maximal opsin conductance around the indicated locations.	50

5.6	The membrane potential (mV) in function of time (ms) with the opsin location indicated in the legend. The membrane potential is measured at the same section. A continuous optogenetic pulse of 500 ms and 5000 W/m^2 , and a normally distributed maximal conductance of $0.7\pi \mu\text{S}$ was used. The optogenetic pulse is indicated with the blue area. The soma and axon are separately plotted. The plot of the remaining sections (b) and (d) is magnified. Plot (a) and (b) are generated with the CP15TK21 model. Plot (c) and (d) with the M18 model. The opsin is normally distributed in both cases.	51
5.7	Delay between the first AP measured in the indicated section and in the soma. The opsin is located in the same section with a normally distributed maximal conductance of $1.0\pi \mu\text{S}$, $0.3\pi \mu\text{S}$, and $1.0\pi \mu\text{S}$ for the grey, light green, and dark green bars, respectively. The respective optogenetic intensities are 5000 W/m^2 , 5000 W/m^2 , and 10000 W/m^2 . The optogenetic pulse is continuous with a pulse duration of 500 ms.	52
5.8	Strength-duration curve for different ChR2(H134R) locations and a maximal conductance of $0.7\pi \mu\text{S}$, recorded in the soma. The optogenetic pulse duration (ms) of a continuous pulse is shown on the x-axis and the optical pulse intensity (W/m^2) on the y-axis. The neuronal models are respectively the M18 model and the CP15TK21 model for the left and right plot.	53
5.9	Input impedance measured at the indicated location in function of the frequency of the oscillatory current stimulus. It is measured 200 ms after the onset of the stimulus. The M18 neuron model was used.	53

List of Tables

2.1	The reversal potential E_{ion} for Na^+ , K^+ , Cl^- and Ca^{2+} given their biological intra- and extracellular concentrations (Petersen, 2016).	5
2.2	Designation ion channels depending on the values of m , the probability of an activation gate being in the open state, and h , the probability of an inactivation gate being in the open state (Gerstner et al., 2014).	10
4.1	The current types present in the M18 model and CP15TK21 model with their corresponding sections (Migliore et al., 2018). Rad, obl, ori, and lm are the respective abbreviations of stratum radiatum, oblique, stratum oriens, and stratum lacunosum-moleculare.	27
4.2	The final 22OM model parameters of the ChR2 mutant, ChR2(H134R), for the double reciprocal addition combination of time constant dependencies (Eq. 4.24) (Schoeters et al., 2021).	30
4.3	The rheobase intensity (I_{RH}) and strength-duration time constant (τ_{SD}) of the strength duration curve in Figure 4.7(a). A maximal conductance of $2.2 \mu\text{S}$ is used.	38
5.1	The mean (μ) and standard deviation (σ) used for the normal distribution of the maximal specific conductance of ChR2(H134R) in M18 and CP15TK21, corresponding with the stimulation locations, in function of the distance to the reference point.	46
5.2	The rheobase intensity (I_{RH}) and strength-duration time constant (τ_{SD}) of the strength duration curves in Figure 5.8. A maximal conductance of $0.7\pi \mu\text{S}$ is used.	52
A.1	The section names, lengths, diameters, surfaces, and number of segments of the reduced-morphology model (CP15TK21) corresponding with Figure 4.1 (Cut-suridis and Poirazi, 2015; Tomko et al., 2021).	58
A.2	The modelparameters of the M18 and CP15TK21 model: uniformly distributed passive parameters, active ionic conductances, and reversal potentials of channels for each section (Tomko et al., 2021; Migliore et al., 2018).	59
A.3	The stimulation and recording sites of CP15TK21 and their corresponding distances to the soma. The equivalent sections of M18 that have similar distances to the soma.	59

List of Abbreviations

AP	Action potential
AIS	Axonal initial segment
ATP	Adenosine triphosphate
bAP	Back-propagating action potential
C	Closed state
CA	Cornu Ammonis
Ca, Ca ²⁺	Calcium ion
ChRs	Channelrhodopsins
ChR2	Channelrhodopsins-2
Cl, Cl ⁻	Chloride ion
CP15	Neuron model of Cutsuridis and Poirazi (2015)
CP15TK21	Neuron model of Cutsuridis and Poirazi (2015) modified by Tomko et al. (2021)
D	Desensitized state
EPSP	Excitatory postsynaptic potential
FR	Mean firing rate
H ⁺	Proton
HH	Hodgkin-Huxley
HR	Halorhodopsins
IPSP	Inhibitory postsynaptic potential
K, K ⁺	Potassium ion
LIF	Leaky integrate-and-fire model
M18	Neuron model of Migliore et al. (2018)
Na, Na ²⁺	Sodium ion
O	Open state
PD	Pulse duration
To21	Neuron model of Tomko et al. (2021)
22OM	Double two-state opsin model of Schoeters et al. (2021)
4SB	Four-state Markov model of Williams et al. (2013)

Chapter 1

Introduction

Yearly, millions of people are affected by neurological diseases like epilepsy, schizophrenia, and Parkinson's disease. Some of them do not react to pharmacological treatment, others are not eligible for resection. Many patients suffer from side effects of their medication and this can decrease the quality of life (Tønnesen and Kokaia, 2017; White et al., 2020). Optogenetics is a promising brain stimulation technique in which molecules are genetically expressed in target cells with the aim of controlling their activity by exposing them to pulses of appropriate wavelengths (He, 2020). The main advantages over other neurological techniques are the cell-type specificity and a higher spatiotemporal resolution (Tønnesen and Kokaia, 2017). However, clinical trials for the use of optogenetics within the brain still face a lot of challenges (White et al., 2020).

In the past years, lots of research has been done to find computational models to simulate optogenetics. In silico predictions of the responses of both the optogenetic tool and the target cell can facilitate real experimentation and provide guidance for the development of in vivo tools (Williams et al., 2013). Furthermore, modeling the kinetics of different opsins can be a guide in the selection of the correct opsin (Schoeters et al., 2021). It has been shown that the kinetics of the spiking output and the efficacy of the stimulation are function of the spatial pattern of illumination (Grossman et al., 2013). In this dissertation, the location dependent effects of optogenetic activation in multi-compartment neuron models will be investigated. A variant of Channelrhodopsin-2 of the *Chlamydomonas reinhardtii* (Nagel et al., 2003) (ChR2(H134R)) is used as optogenetic tool. This opsin is expressed in hippocampal CA1 pyramidal neurons. ChR2(H134R) is modeled by the double two-state model of Schoeters et al. (2021). Two neuron models of different complexities are used to model the neuron: a modified version of the reduced-morphology model of Cutsuridis and Poirazi (2015) by Tomko et al. (2021) (CP15TK21 model) and the full-morphology model of Migliore et al. (2018) (M18 model). The models are implemented in the NEURON simulation platform (Carnevale and Hines, 2006). A comparative analysis of the location dependent effects is done in view of finding stimulation strategies that will improve the efficiency and selectivity of optogenetic protocols. Finally, the impact of using neuron models of different complexities on the results will be investigated.

In the second chapter, the transition is made from a real neuron to a computational model. The main properties of the neuron, necessary to translate the neuron's kinetics into a model, are enlightened. Extra attention is given to the hippocampal CA1 pyramidal neuron since this neuron is used in the modeling. Afterward, the leaky integrate-and-fire model together with the Hodgkin-Huxley model are explained to grasp the basics of neuron models. The neuron cannot be reduced to a point in order to investigate the location dependent effects on the neuron. For that reason, multi-compartment models are explained in the last section.

An introduction to optogenetics is given in Chapter 3. An optimal optogenetic tool can only be gained by selecting the correct opsin. An overview of the most known opsins is given in Section 3.1 with the focus on Channelrhodopsin-2. Next to the neuron model, an opsin model is necessary to conduct the study. A substantiation is given to the choice of working with the double two-state model of Schoeters et al. (2021). Section 3.2 focuses on the subcellular optogenetics. Here, the current state of art is discussed. The chapter is ended with the challenges which are still faced in the field of optogenetics.

The first two sections of Chapter 4 explain the models that are used in more detail: the neuronal model of Cutsuridis and Poirazi (2015) (CP15TK21) and the ChR2(H134R) model of Schoeters et al. (2021). An extensive comparison is made between different ChR2(H134R) locations on the optogenetic excitability in a CA1 pyramidal neuron modeled by the reduced-morphology model of Cutsuridis and Poirazi (2015). The small number of sections even allows to stimulate sections in a single dendrite in order to investigate the location dependent effects on the smallest scale. Six different stimulation locations are chosen diffuse across the neurons. They comprise the soma, the axon, a basal dendrite section, an apical trunk section, a radial oblique dendrite section, and an apical dendritic tuft section. Primarily, the generic response of the CA1 pyramidal neuron on different optogenetic stimulation strategies, is studied. Thereafter, the symmetric sections are included and finally two sections of the same basal dendrite are stimulated in order to study the influence of the geometry of the section and distance to the soma.

Many different models have been developed for the CA1 pyramidal neuron, from morphologically simple to very detailed models. In Chapter 5, a second neuronal model is used with the same biophysics as CP15TK21 but a more detailed morphology: the model of Migliore et al. (2018). A description is given in Section 5.1. An increased number of sections led to the necessity of working with a normally distributed opsin conductance instead of a uniform distribution. Similar stimulation locations are tested and the results are compared with the reduced-morphology model of Cutsuridis and Poirazi (2015).

Chapter 2

Computational neurophysiology

Understanding the function of the brain starts with focusing on the biology of the brain. When the physiology and the dynamics of the brain are known, they can be translated into a computational model. These computational models can predict the response of the cell which can be used to facilitate real experiments. In the following, the physiology of the neuron is discussed. This is then translated into a computational model. Many models have been created and two of them are discussed in Section 2.2: the leaky integrate-and-fire model and the Hodgkin-Huxley model. The following part is mainly based on two sources: (Gerstner et al., 2014) and (Petersen, 2016).

2.1 Neurophysiology

When studying the functioning of the brain, it is best to start with its smallest components: the neurons. These are the brain's most elementary processing units and are connected via synapses. Neurons are structured into networks that can contain more than 10^4 cell bodies. The basic elements of a neuron are the dendrites, the soma, and the axon. An example of a neuron is shown in Figure 2.1 (Gerstner et al., 2014).

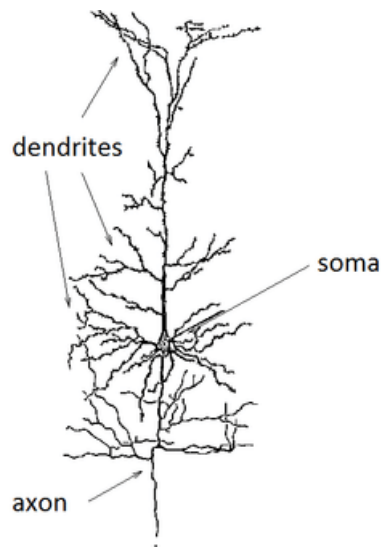


Figure 2.1: Single neuron in a drawing by Ramón y Cajal. The basic elements are shown: dendrite, soma, and axon (Gerstner et al., 2014).

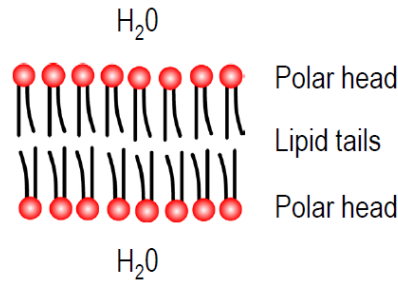


Figure 2.2: Multiple phospholipids forming a cell membrane (Petersen, 2016).

Communication between and within neurons takes place via chemical and electrical signals. The properties of the neuron's cell membrane are important in understanding the origin of these signals. The cell membrane of a neuron is a phospholipid bilayer. Phospholipids are made up of a lipophilic or hydrophobic tail and a hydrophilic phosphate head group. Figure 2.2 shows how several phospholipids can form a cell membrane.

The most relevant properties of the cell membrane are the electrical properties. Due to its anatomy, the cell membrane is only permeable to lipophilic structures like gases, lipids, and non-polar molecules. There is only a limited permeability to water and, most importantly, no permeability to ions and charged molecules. Therefore there is a possible concentration difference between both sides of the cell membrane. A concentration difference of charged ions then leads to an electrical potential across the membrane and this is called the membrane potential. Sodium (Na^+), potassium (K^+), and chloride (Cl^-) ions are those with the highest influence on this potential. A typical cell contains a higher concentration of potassium ions on the inside and a higher concentration of sodium and chloride ions on the outside (Petersen, 2016).

Electrical signal conduction would not be possible if the membrane potential was static. That is why the cell membrane comprises ion channels, i.e. transmembrane proteins that can mediate the flux of ions across the neuron's membrane. Next to ion channels, there are some other transporters who can control the movement of ions, but these are slower and involve more complex steps, e.g. the hydrolysis of ATP. Ion channels, on the other hand, are fast and can provide large electrical currents that have a direct effect on the membrane potential. For this reason, ion channels are the most interesting transporters to focus on when studying electrical brain signals. Neher and Sakmann (1976) developed the so-called patch-clamp recording technique which allowed them to determine the 2 major properties of ion channels. The first one is the unitary opening and closing of ion channels. The second one is the ion channels' selectivity towards certain ion types. Thus, ion channels have a conductance which is influenced by the probability that the ion channel is open, the electrical field across the membrane, and the concentration gradient (Petersen, 2016).

In brief, a neuron has a cell membrane which is impermeable to ions and charged molecules. A concentration difference of charged ions is built up across the cell membrane which results in an electrical potential, the membrane potential. So the two dominant, opposing forces are the concentration gradient and the electrical gradient. Despite the impermeability of the cell membrane, there can be an ion flux due to the ion channels. This flux is controlled by the two major forces and can be described as the electro-chemical diffusion.

An important property of a specific ion is its reversal potential. It is defined as the potential at which there is no net flux of ions given the extra- and intracellular ion concentration. In this case, the electrical and the concentration gradient cancel each other out. The reversal potential

is given by the Nernst equation:

$$E_x = \frac{RT}{zF} \ln \frac{[X]_o}{[X]_i} \quad (2.1)$$

Where X is a certain ion species, R is Avogadro's gas constant, T is the temperature in Kelvin, F is the Faraday constant and z is the charge of the ion. $[X]_o$ and $[X]_i$ are the ionic concentrations respectively on the outside and inside of the cell. To determine the reversal potential of ions, the biological concentrations are used (Petersen, 2016). As the values of the reversal potential of Na^+ , K^+ , Cl^- , and Ca^{2+} are important in what follows, they are listed below.

Table 2.1: The reversal potential E_{ion} for Na^+ , K^+ , Cl^- and Ca^{2+} given their biological intra- and extracellular concentrations (Petersen, 2016).

Ion	Intracellular $[X]_i$	Extracellular $[X]_o$	E_{ion}
K^+	150 mM	4 mM	-97 mV
Na^+	12 mM	145 mM	+67 mV
Cl^-	5 mM	120 mM	-85 mV
Ca^{2+}	100 mM	1 mM	+123 mV

If the neuron would only be permeable for one ion, the resting membrane potential would be equal to its reversal potential. Because this is not the case, the Goldman-Hodgkin-Katz equation can be used to calculate the equilibrium potential including multiple monovalent ions (Petersen, 2016). It is given by:

$$V_m = \frac{RT}{F} \ln \frac{P_{\text{K}^+} [\text{K}^+]_o + P_{\text{Na}^+} [\text{Na}^+]_o + P_{\text{Cl}^-} [\text{Cl}^-]_i}{P_{\text{K}^+} [\text{K}^+]_i + P_{\text{Na}^+} [\text{Na}^+]_i + P_{\text{Cl}^-} [\text{Cl}^-]_o} \quad (2.2)$$

In this equation, the parameters have the same meaning as in Eq. 2.1 and P_x is the permeability ratio for ion x. Typically, the measured resting membrane potential of a neuron is around -65 mV. Thus, the neuron, without any inputs, already has a strongly negative polarization. When a neuron receives an input from a presynaptic neuron, its membrane potential can increase or decrease, which is respectively referred to as excitatory (EPSP) or inhibitory (IPSP) post synaptic potential. Since the neuron receives inputs from multiple presynaptic neurons, the EPSP and IPSP sum together until the membrane potential exceeds the firing threshold. In this case, the membrane potential increases rapidly with an amplitude of around 100mV and a typical duration of 1-2 ms. This rapid change in membrane potential is called an action potential (AP), the elementary unit of signal transmission (Gerstner et al., 2014).

2.1.1 Hippocampal CA1 neuron

The brain can be seen as a structure organized in different (sub)regions. Every region is made of different layers and every layer contains neurons of various types (Gerstner et al., 2014). Cortical neurons can be classified based on intrinsic properties like their morphology, connectivity, or neurochemical profile. As stated before, according to their neurochemical profile neurons can be excitatory or inhibitory. Morphologically, neurons can be classified based on their shape, orientation, and projections. Well-known morphologies are the pyramidal, stellate, basket, and bipolar morphologies. The rest of this study will mainly focus on the pyramidal neuron, visualised below (Figure 2.3). The apical and basal dendritic trees are typical for this kind of neuron,

which derives its name from the pyramidal shape of the soma. These neurons are abundantly present in several regions of the brain (Spruston, 2008; Deleanu, 2021).

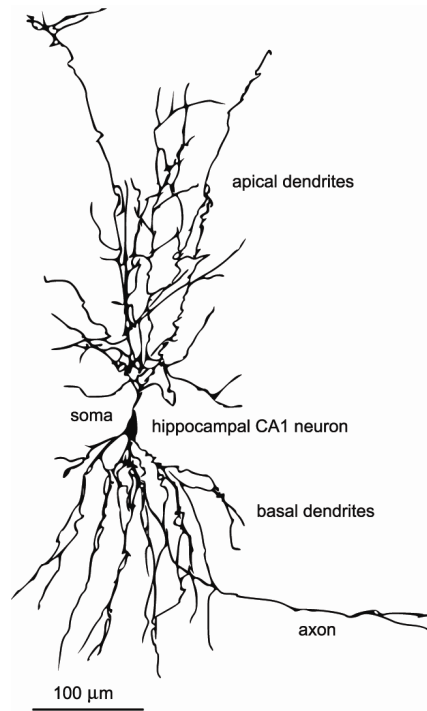


Figure 2.3: A hippocampal CA1 neuron. Typically contains apical and basal dendrites and has a pyramidal shaped soma. (Georgiev, 2009)

More specifically, the pyramidal neurons of the CA1 region of the hippocampus will be used throughout this study. This choice was made based on the extensive available knowledge. More than 130 model entries can be found on ModelDB, from simple to very detailed models (McDougal et al., 2017; Tomko et al., 2021). Section 4.1 and 5.1 will elaborate further on which models are most interesting for this research. To correctly situate the CA1 region, it is important to first have a look into the anatomy of the hippocampus. The hippocampus is involved in memory processing, learning, spatial navigation, and emotions. According to Fogwe et al. (2022), it can be described as a curved and recurved sheet of the cortex that folds into the temporal lobe’s medial surface. The main zones are the dentate gyrus, the cornu ammonis (CA), and the subiculum. The pyramidal cells of the cornu ammonis are organized into different zones: CA1, CA2, CA3, and CA4. In the CA1 region, 90% of the neurons are pyramidal neurons and the remaining ones are interneurons. The axons of the CA1 pyramidal cells are connected to the subiculum neurons (Fogwe et al., 2022; Chauhan et al., 2021; Hammond, 2015). Furthermore, the cornu ammonis has 5 sublayers:

1. Alveus
2. Stratum oriens: basal dendrites of pyramidal cells.
3. Stratum pyramidale: principle cell layer, contains 10-30 layers of pyramidal cells. Their somas are aligned here.
4. Stratum radiatum: apical dendrites of the pyramidal cells are extended here.
5. stratum lacunosum – moleculare: apical dendrites arborize here.

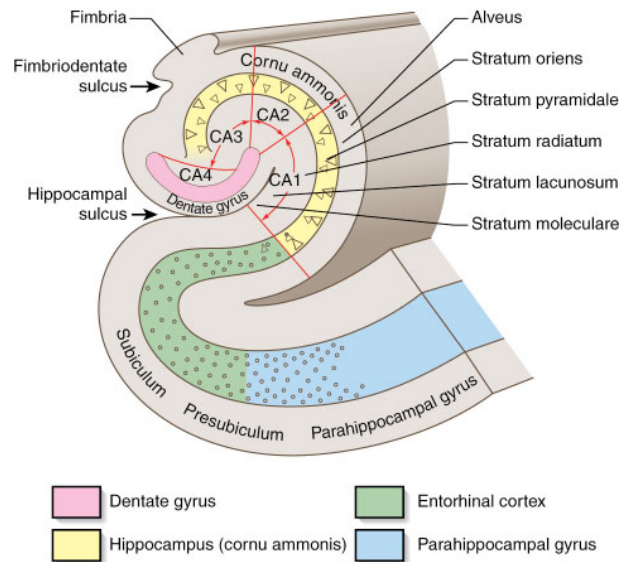


Figure 2.4: Hippocampus with 3 main zones: dentate gyrus, cornu ammonis, and subiculum. Pyramidal cells are organized in zones CA1, CA2, CA3 and CA4. The cornu ammonis has five sublayers as explained in text (medical dictionary: <https://medicine.en-academic.com/3923>).

In this dissertation, optogenetic stimuli are applied to various locations of the neuron with as result that signals will propagate along the neuron. The physiological features of a CA1 pyramidal cell are important in the clarification of the way in which signals propagate as we will observe in the results. In CA1 pyramidal cells the action potential is typically initiated in the axon hillock and propagated forward to the axon and backward to the dendritic tree as a back-propagating action potential (bAP) (Tomko et al., 2021). Tomko et al. (2021) and Sáray et al. (2021) describe some key physiological features. A first one concerns the somatic spiking properties. The neuron gets inputs from synapses located all over the neuron. These can have multiple spatiotemporal patterns which are transformed into one single spiking output (Migliore et al., 2018). Measurements are often performed at the soma, since this is the final integration site, together with the axon (Magee and Cook, 2000). Spike event features, spike shape features and voltage features can be studied (Tomko et al., 2021). Another physiological feature is the somatic depolarization block. When a current is injected into the soma with increasing intensity, the CA1 pyramidal cell will first respond with an increasing number of action potentials. If the current intensity exceeds a certain threshold, the cell stops firing after some action potentials, and the membrane potential reaches an equilibrium point (Bianchi et al., 2012). In the past, this phenomenon was considered unphysiological but Bianchi et al. (2012) showed that it can actually occur *in vivo* for a level of synaptic activity within the physiological range. Furthermore, depolarization block is said to be relevant in modulating the initiation and spread of focal epileptic seizures since it seems to be one of the mechanisms that protect this neuron from firing at high frequencies (Bianchi et al., 2012). Contrary to back-propagating APs, excitatory post synaptic potentials (EPSP) travel from apical dendrites toward the soma and axon. During this propagation, they are typically attenuated. The post synaptic potential attenuation is defined as the ratio between the peak amplitude of the somatic EPSP and the local dendritic EPSP (Tomko et al., 2021). Action potentials are normally initiated in the soma or axon because of their lowest voltage threshold for spike generation. However, sometimes local dendritic spikes are observed. They are characterized by a more depolarized voltage threshold than the soma (Gasparini, 2004). Gasparini (2004) found that highly synchronized inputs with moderate levels of spatial clustering are necessary for spike initiation at these locations. Losonczy and Magee (2006) have shown the same for radial oblique dendrites, namely, asynchronous input patterns are linearly summed and synchronous inputs supralinear, meaning that there is an initiation of a dendritic spike. Local

dendritic spikes can provide neurons with additional computational abilities. Not only EPSP, but also back-propagating action potentials are attenuated to some extent. The propagation of a bAP is a measure for the dendritic excitability (Sáray et al., 2021). Golding et al. (2001) describe how there is a dichotomy between strongly, weakly and intermediate backpropagating cells. Multiple factors have an impact on the degree to which backpropagating action potentials invade the dendritic arbor, including the dendritic morphology, shape of action potentials in the soma, and the distribution of sodium and potassium channels in the dendrites.

2.2 Neuron models

The neurophysiology that was discussed in Section 2.1 can now be translated into computational models. I will start by focusing on the integrate-and-fire model, as it is the simplest of the following models. The books of Izhikevich (2006) and Gerstner et al. (2014) are used to support the mathematical foundation of this model. Afterwards, I will focus on the Hodgkin-Huxley model, also brought forward by Izhikevich (2006) and Gerstner et al. (2014), as it is the most used model in the computational neuroscience.

2.2.1 Integrate-and-fire model

The name 'integrate-and-fire model' refers to the integration of all postsynaptic potentials. When the firing threshold is exceeded, the neuron will fire an action potential which defines the 'fire' term. The fact that APs are described as events rather than describing the spike generation mechanism is what simplifies this model. Gerstner et al. (2014) state that this is plausible in the assumption that the shape of an AP cannot be used to transmit information since it always has roughly the same form.

Figure 2.5 on the left by Gerstner et al. (2014) illustrates how the membrane can be represented by an electrical circuit. The cell membrane does not allow ions to move to the other side. Since the membrane is very thin, the charged ions can interact through electrostatic forces. Therefore, the membrane can be compared to a capacitor where the lipids act as a dielectric and the ions as the charges (Petersen, 2016). A neuron at rest has a resting potential V_{rest} which is represented by a voltage source V_{rest} . The input current $I(t)$ can be seen as an experimentally injected current or synaptic input from other neurons. Since the cell membrane is not a perfect insulator, there will be a leakage current (Gerstner et al., 2014). When this current is assumed to be Ohmic with finite leak resistance R , the model is named a leaky integrate-and-fire (LIF) model.

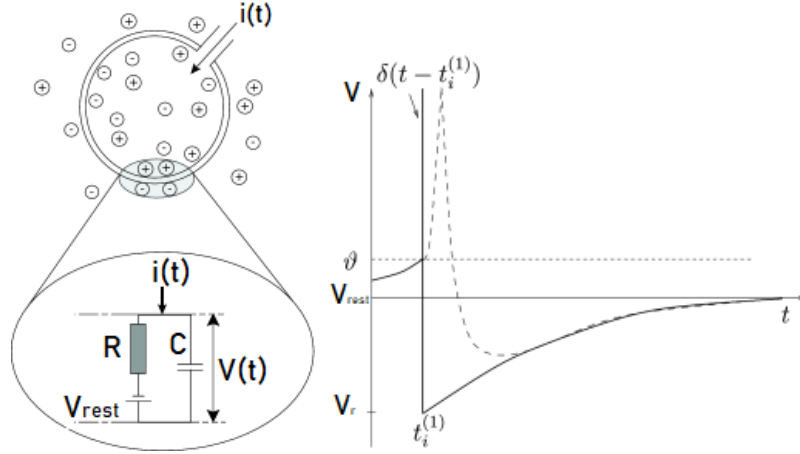


Figure 2.5: Left: Electrical equivalent of the neuron for a LIF model. $I(t)$ represents the input current, $V(t)$ the membrane potential. The cell membrane acts as a capacitor with capacity C . There is an Ohmic leakage current with resistance R which is in line with a battery of potential V_{rest} (Gerstner et al., 2014). Right: Membrane potential in function of time given by the leaky integrate-and-fire model (solid line) compared to a normal action potential (dashed line). After crossing the firing threshold θ at time t_i , a spike is generated and the membrane potential is reset to the potential V_r (Gerstner et al., 2014).

Two mechanisms are used to describe the neuronal dynamics. First, a linear differential equation describes the subthreshold behavior:

$$C \frac{dV(t)}{dt} = I(t) - \frac{V(t) - V_{rest}}{R} \quad (2.3)$$

which is obtained by the law of current conservation. This can be rewritten as:

$$\tau_m \frac{dV(t)}{dt} = -[V(t) - V_{rest}] + RI(t) \quad (2.4)$$

with $\tau_m = RC$ the membrane time constant. Eq.2.4 is also called the equation of a passive membrane (Gerstner et al., 2014). The solution to this equation is:

$$V(t) - V_{rest} = \Delta V \exp\left(-\frac{t - t_0}{\tau_m}\right) \text{ for } t > t_0 \quad (2.5)$$

if the initial conditions $V(t_0) = V_{rest} + \Delta V$ and $I(t) = 0$ for $t > t_0$ are satisfied. This equation shows that for this simple case, the membrane potential decays to its resting potential in the absence of an input (Gerstner et al., 2014).

The second mechanism is a spike generating mechanism. The neuron generates an AP at the moment the membrane voltage reaches the firing threshold θ . The representation of the spike is not defined but a vertical line or δ pulse is often used. Yet, the presence or absence of the spike is of greater importance than the morphology of the AP. After firing, the membrane potential is reset to V_r for which $V_r < \theta$ applies, and subsequently, these two mechanisms are repeated. To conclude this model, a graph of the membrane potential over time is shown in Figure 2.5 on the right to illustrate the LIF model (Gerstner et al., 2014).

2.2.2 Hodgkin-Huxley model

In 1952, Hodgkin and Huxley performed groundbreaking experiments on the squid giant axon. One of their most notable conclusions was that the following three major ion currents should be taken into account: the voltage-gated K^+ current and Na^+ current and an Ohmic leak current. The leak current comprises mainly the Cl^- current and other less important channel types. These experiments resulted in the famous Hodgkin-Huxley (HH) model which, according to Izhikevich (2006), is one of the most important models in computational neuroscience. In the following, a better framework for the ionic currents will be given in order to create an understanding of the Hodgkin-Huxley model. As stated before, ion channels allow ions to flow through the cell membrane. To understand how action potentials are built up, it is important to look at the driving force of an ion current. The bigger the difference between the membrane potential and the Nernst equilibrium potential E_k of an ion type k , the bigger the ionic current will be (Izhikevich, 2006):

$$I_k = g_k(V - E_k) \quad (2.6)$$

The difference $(V-E_k)$ is the driving force and g_k is the effective conductance in mS/cm^2 of ion type k . Important to mention is that this conductance is not constant but can depend on the membrane potential or intra- or extracellular agents. The ionic currents are therefore not Ohmic. The time-varying conductance allows this model to generate an AP compared to the LIF model where the AP mechanism is not modelled. According to Izhikevich (2006), the effective conductance g of a channel can also be written differently:

$$g = \bar{g}p \quad (2.7)$$

where \bar{g} is the maximal conductance of the channel and p is the probability that the channel is open. The HH model only considers the three major ion currents: I_K , I_{Na} and the leak current I_l . I_K , and I_{Na} are both voltage-gated currents while I_l is an Ohmic current meaning that the conductance g is constant. Voltage-gated currents' conductance depends, as the name implies, on the membrane voltage. The voltage-gated ion channels can consist of so-called gates. These gates can be activating or inactivating, meaning that they open or close the ion channel. The proportion of open channels p in a large population is thus (Izhikevich, 2006):

$$p = m^a h^b \quad (2.8)$$

where m denotes the probability of an activation gate being in the open state. The probability of an inactivation gate being in the open state is indicated by h . Parameters a and b respectively represent the number of activation and inactivation gates. Depending on the value of m and h , channels are called (partially) (in)active, deactive, or deinactive. A summary of the above is given in Table 2.2.

	0	0-1	1
m	Deactive	Partially active	Active
h	Inactive	Partially inactive	Deinactive

Table 2.2: Designation ion channels depending on the values of m , the probability of an activation gate being in the open state, and h , the probability of an inactivation gate being in the open state (Gerstner et al., 2014).

With all this information in the back of our minds, understanding the Hodgkin-Huxley model becomes significantly easier. Again, an equivalent circuit is made. Compared to the equivalent circuit in the LIF model, there are now three currents instead of one leak current, namely the three major currents discussed above. The capacitor represents the cell membrane. The ion channels are modelled in parallel with the capacitor and are represented as resistors. $I(t)$ is the injected current and V the membrane potential. Differences in ion concentrations result in a Nernst potential which is different for the different ion types. This is implemented in the circuit as the voltage sources E_l , E_{Na} , and E_K . As discussed above, the sodium and potassium currents are not Ohmic, meaning that the resistors are not fixed, which is indicated by the diagonal arrows. (Gerstner et al., 2014)

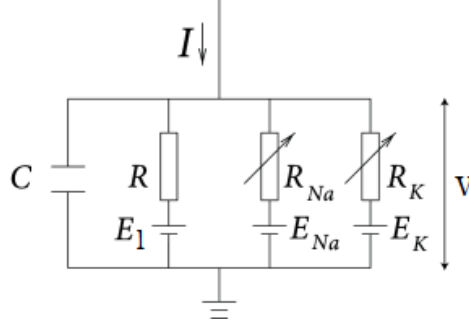


Figure 2.6: The equivalent circuit corresponding with the Hodgkin-Huxley model (Gerstner et al., 2014).

The following formulas are derived from the book of Gerstner et al. (2014). The injected current is the sum of the capacitive current and the three ion currents:

$$I = C \frac{dV}{dt} + \sum_k I_k \text{ with } k = Na, K, l \quad (2.9)$$

As in Eq. 2.6, every ion current can be written as $I_k = g_k(V - E_k)$. g_l is constant given that the leak current is Ohmic. Sodium channels have three activation gates and one inactivation gate. Using Eq. 2.7 and Eq. 2.8 gives $g_{Na} = g_{\bar{Na}} m^3 h$. Potassium has four activation gates and no inactivation gates which gives: $g_K = g_{\bar{K}} n^4$. This results in the final HH equation:

$$C \frac{dV}{dt} = I - g_{\bar{K}} n^4 (V - E_K) - g_{\bar{Na}} m^3 h (V - E_{Na}) - g_l (V - E_l) \quad (2.10)$$

The dynamics of the gating variables m , n and h are described by:

$$\tau_x(V) \dot{x} = -[x - x_\infty(V)] \text{ for } x = n, m, h \quad (2.11)$$

or

$$\dot{x} = \alpha_x(V)(1 - x) - \beta_x(V)x \text{ for } x = n, m, h \quad (2.12)$$

With τ_x the time constant of gating variable x and $x_\infty(V)$ the voltage-sensitive steady-state (in)activation function. Both variables can be measured experimentally (Izhikevich, 2006). For a constant potential V , gating variable x will approach x_∞ with a time constant τ_x . In Figure 2.7 on the left can be seen how the steady-state (in)activation functions evolve in function of the membrane potential. The voltage-dependent time constants are depicted on the right.

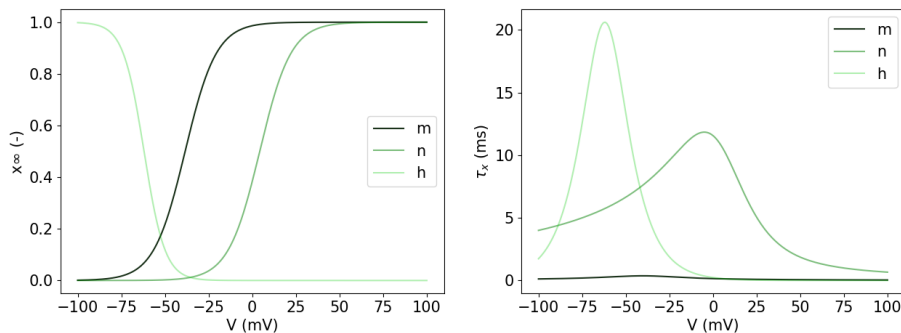


Figure 2.7: Left: the steady-state (in)activation functions x_∞ in function of the membrane voltage. Right: the time constants τ_x in function of the membrane voltage (Gerstner et al., 2014).

These two graphs are of great importance in understanding how the HH model can actually generate an AP. Depolarization occurs when the interior of a neuron becomes more positive and the membrane potential increases. This can be the result of an inward synaptic current. A large depolarization results in an increase of m_∞ and n_∞ and a decrease of h_∞ , which can be seen in Figure 2.7 on the left. The variable m approaches m_∞ fast because τ_m is small. This means that there is a large inward current of positive Na^+ ions, depolarizing the neuron even more. This is a positive feedback loop. On the other hand, depolarization results in an increase of n , resulting in an outward or repolarizing potassium current, which counteracts the depolarization. This is a negative feedback loop. At the same time, variable $h \rightarrow 0$, inactivating the Na^+ current. This is called the repolarization phase. So an AP is generated when the positive feedback loop transcends the negative feedback loop. The after-hyperpolarization can be explained by the slow dynamics of n , driving the potential toward E_K . The absolute refractory period occurs immediately after the repolarization. No AP can be generated due to the inactivated Na^+ current which is a result of the large time constant of h . The relative refractory period is the period in which the Na^+ current starts deinactivating and there is a possibility to generate an AP but only if the stimulus is higher than normal (Izhikevich, 2006).

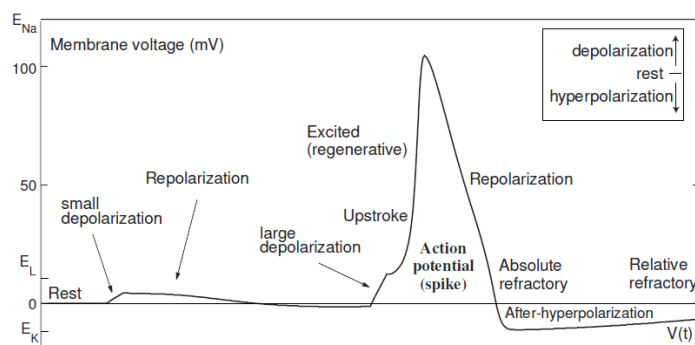


Figure 2.8: Different stages of an action potential in the Hodgkin-Huxley model (Izhikevich, 2006).

A good comparison between simple models like the leaky integrate-and-fire model and more advanced models like the conductance-based models (e.g. Hodgkin-Huxley model) is given in the book of Izhikevich (2006). Izhikevich (2006) states that in the latter, each variable and parameter is linked to a well-defined biophysical meaning which can be measured experimentally. Due to measurement errors, the results can deviate from those in experiments which is a drawback of conductance-based models. According to (Izhikevich, 2006) the simple models prove to be a better solution as they can reproduce the neurocomputational features more faithfully. These

simple models may be less biophysically detailed, but they prove themselves to be much more computationally efficient. Yet, the HH model is still used much more often because the simple models neglect a lot of important dynamics, such as adaptation, inhibitory rebound, conductance changes after a spike (Gerstner et al., 2014). Both the HH and the LIF models reduce the neuron to a point and ignore the spatial extent and variability of neurons. Using multi-compartment models, it is possible to expand the point-like neuron to a more realistic neuron for which spatial coordinates are included in the model. This is obviously of great importance in this dissertation. These multi-compartment models are treated in the next section.

2.3 Multi-compartment models

The neuron models treated above reduced the neuron to a point. The membrane potential and currents were only function of time and no spatial coordinate was used. In this case, the neuron was assumed to be isopotential. Figure 2.3 shows a potential neuron with an arbor-like structure with different branches. The size of the soma is around $10\mu\text{m}$ but the length of a neuron can go up to hundreds of microns (Petersen, 2016; Gerstner et al., 2014). Spatial aspects are of great importance in signal processing and the study of optogenetics. Obviously, to investigate the location dependent effects of optogenetics it is necessary to broaden the view and to include the spatial aspects of the neuron. For this purpose, the cable equations are derived based on the books of Gerstner et al. (2014) and Petersen (2016).

A piece of the neuron's dendrite can be seen as a leaky electrical cable. Gerstner et al. (2014) represents this piece as a cylindrical tube (Figure 2.9). Intracellular, there is an axial current, $i(x)$, that follows the spatiotemporal voltage gradients along the length of the neuron. Part of this current leaks out transversely through the ion channels. Another part of this current is used to charge the local membrane capacitor. The current difference is, therefore:

$$i(t, x + dx) - i(t, x) = -C \frac{\partial V(t, x)}{\partial t} - \sum_{ion} I_{ion}(t, x) + I_{ext}(t, x) \quad (2.13)$$

where the first term represents the change due to charging the local capacitor and the second term represents the loss of current through the ion channels. I_{ext} is the externally applied current. The drop in membrane potential $V(x)$ is the result of the longitudinal resistance R_L of the neurons arbor and depends on the geometry.

$$V(t, x + dx) - V(t, x) = -R_L i(t, x) \quad (2.14)$$

The capacitance C , ion currents I_{ion} , externally applied current I_{ext} , and longitudinal resistance R_L are rewritten in terms of their specific quantities per unit length:

$$C = c dx, I_{ion} = i_{ion} dx, I_{ext} = i_{ext} dx, R_L = r_L dx \quad (2.15)$$

Dividing Eq. 2.13 and Eq. 2.14 by dx and taking the limit of $dx \rightarrow 0$ gives:

$$\frac{\partial V(t, x)}{\partial x} = r_L i(t, x) \quad (2.16)$$

$$\frac{\partial i(t, x)}{\partial x} = c \frac{\partial V(t, x)}{\partial t} + \sum_{ion} i_{ion}(t, x) - i_{ext}(t, x) \quad (2.17)$$

And finally, the derivative of Eq. 2.16 is taken and substituted into Eq. 2.17 to get:

$$\frac{\partial^2 V(t, x)}{\partial x^2} = cr_L \frac{\partial V(t, x)}{\partial t} + r_L \sum_{ion} i_{ion}(t, x) - r_L i_{ext}(t, x) \quad (2.18)$$

This is called the general cable equation.

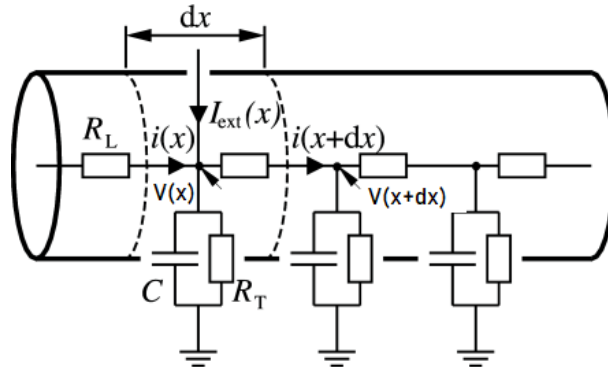


Figure 2.9: Simplification of a neuronal section with corresponding circuit diagram. R_L , and R_T are the longitudinal and transversal resistors, respectively. Capacitor C is the electrical capacity (Gerstner et al., 2014).

There could be an analytical solution only if the cable was passive and if the electrical and geometrical properties were uniform across the whole neuron. Since these conditions are not realistic for natural neuronal structures, numerical solutions should be found. Izhikevich (2006) explains how the continuous dendritic structure can be replaced with a network of discrete compartments. This is called a multi-compartment model and is illustrated in Figure 2.10 from (a) to (b). After this discretization, the ordinary time-dependent differential equations can be used at each of the chosen discretization points. Each compartment has its capacity and transversal conductivity. Finally, all compartments are coupled via their conductances. Figure 2.10 (c) depicts two compartments. If V_s and V_d are respectively the membrane potentials of the soma and the dendrite, they are coupled via:

$$C_s \dot{V}_s = -I_s(V_s, t) + g_s(V_d - V_s) \quad (2.19)$$

$$C_d \dot{V}_d = -I_d(V_d, t) + g_d(V_s - V_d) \quad (2.20)$$

Where $I_x(V, t)$ is the sum of all currents in compartment x and g_s and g_d are the coupling conductances. The relative size of the dendritic and somatic compartments can change these conductances (Izhikevich, 2006; Petersen, 2016). Such multi-compartment models will be used for the CA1 pyramidal neuron and are explained in more detail in Section 4.1 and 5.1.

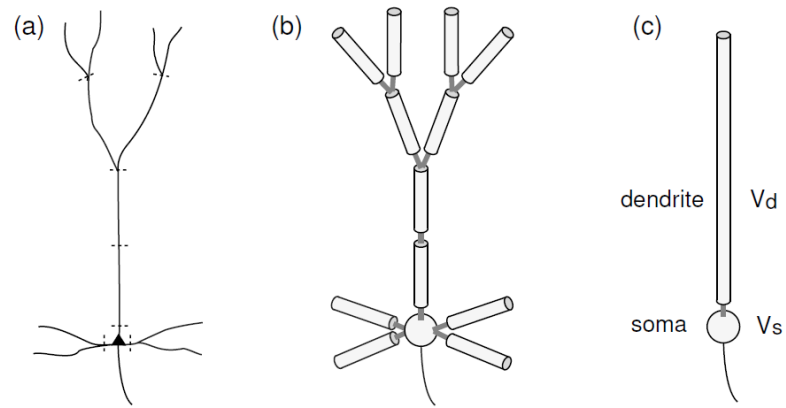


Figure 2.10: Replacement of a neuronal structure (a) by a multi-compartment model (b). (c) A 2-compartment model with membrane potential V_d and V_s in the dendrite and soma, respectively (Izhikevich, 2006).

Chapter 3

Optogenetics

Optogenetics is a fast-growing field in which molecules are genetically expressed in target cells with as result that the cell can either optically report on cellular physiology (sensors) or control cellular pathways actuated by light (actuators) (Yawo et al., 2021). The research of this dissertation specifically focuses on these actuators which can be light-activated ion channels or ion pumps expressed on the neuron. The modulated cell's cellular activity, e.g. the excitability, is controlled by exposing it to sequences of light pulses. Optogenetics allows studying the brain's mechanisms to get a better understanding of complex tasks such as perception or cognition (He, 2020). Besides its investigative function, it is also very promising as a therapeutic tool for neurological disorders. Compared to conventional stimulation or recording methods, optogenetics has some important advantages: cell-type specificity, higher spatiotemporal resolution, bidirectional control, and greater convenience (Tønnesen and Kokaia, 2017), (Yawo et al., 2021). Epilepsy is one of the most prevalent types of neurological diseases that yearly affects millions of people. Tønnesen and Kokaia (2017) clarify how optogenetics can be used to either shut down excitatory neurons or activate inhibitory neurons to control abnormal circuit activity. Other examples of fields of interest are Parkinson's disease, depression, schizophrenia and different types of addiction (Guillaumin et al., 2021; Fakhoury, 2021; McNally et al., 2021; Stamatakis and Stuber, 2012). Retinitis Pigmentosa, a neurodegenerative eye disease where loss of photoreceptors can lead to blindness, is one of the few diseases for which clinical trials are conducted (Sahel et al., 2021). Sahel et al. (2021) report one of the first results of this pioneering study. In these trials, a viral vector encoding a light-sensing channelrhodopsin protein was injected to target retinal cells. Engineered goggles were used to capture images and project them as light pulses onto the retina. This led to partial functional recovery of the vision (Sahel et al., 2021). However, clinical trials for the use of optogenetics within the brain still face a lot of challenges. The use of gene therapy techniques to introduce light-sensing proteins and the implantation of electronic devices to provide optical stimulation to this day still lead to a lot of unsolved puzzles (White et al., 2020).

3.1 Microbial opsins

Genetically expressed molecules are also referred to as optogenetic probes or tools (Tønnesen and Kokaia, 2017). In the past years, there has been an expansion of types and variants within this group. Rost et al. (2017) divide these tools into actuators and sensors. Actuators are expressed molecules with the aim of manipulating cellular activities like membrane potential, membrane composition, protein and organelle localization, and gene expression. Sensors, on the other hand, will visualize physiological events in the cell by means of optical signals. For this dissertation, the relevant molecules are the actuators who modulate the membrane potential.

Opsin genes are subdivided into microbial opsins (type I) and animal opsins (type II) (Fenno et al., 2011). Proteins of both types require retinal, which is a vitamin A-related organic cofactor that serves as an antenna for photons (Fenno et al., 2011). Proteins that are bound to retinal are called rhodopsins. According to Rost et al. (2017), microbial rhodopsins are the most commonly used optogenetic actuators. This is explained by the small size of their protein-encoding genes, the availability of all-trans retinal in mammalian neurons, and the millisecond timescale of their activation and deactivation (Rost et al., 2017). Thus, the further discussed opsins are microbial rhodopsins that modulate the membrane potential.

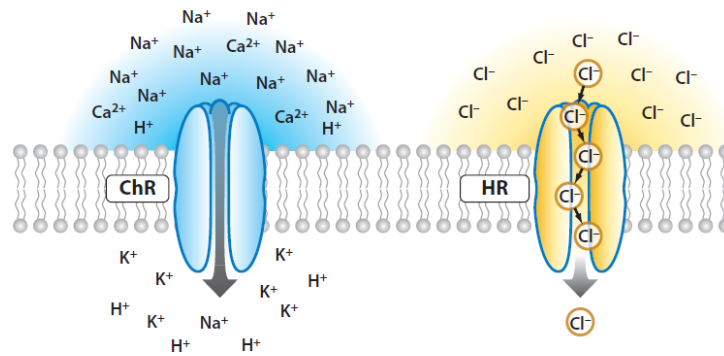


Figure 3.1: Visualisation of excitatory Channelrhodopsin (ChR) and inhibitory Halorhodopsin (HR) (Fenno et al., 2011).

An important distinction that can be made between opsins is their inhibitory or excitatory character. Inhibitory opsins will transport protons outward or chloride ions inward the cell via a pump. This results in a hyperpolarization in response to light stimulation and therefore an increased electrical threshold and a lower excitability of the neuron. According to Tønnesen and Kokaia (2017) the most used hyperpolarizing optogenetic probes in research are probes of the class of Halorhodopsins (HR). These are light-driven inward chloride pumps derived from the cell membrane of halobacterium (e.g. NpHR). Such a pump is visualised on the right of Figure 3.1. Examples of the outward proton pumps are Arch derived from *Halorubrum sodomense* and ArchT derived from *Halorubrum* strain TP009. Excitatory opsins will cause a depolarization of the neurons making them more excitable. Channelrhodopsins (ChRs) are light-gated cation-channels that passively conduct ions along electrochemical gradients. This can be seen in Figure 3.1 on the left. Modified versions of Channelrhodopsin-2 (ChR2), isolated from *Chlamydomonas reinhardtii*, are the most popular excitatory optogenetic probes among all. In general, ion channels have simpler molecular mechanisms and faster dynamics than pumps (Tønnesen and Kokaia, 2017; Rost et al., 2017). This fact and the available literature make ChR2 an ideal candidate to conduct this study with. Therefore, this study will now proceed to describe the structure and dynamics of ChR2 in more details.

3.1.1 Channelrhodopsin-2

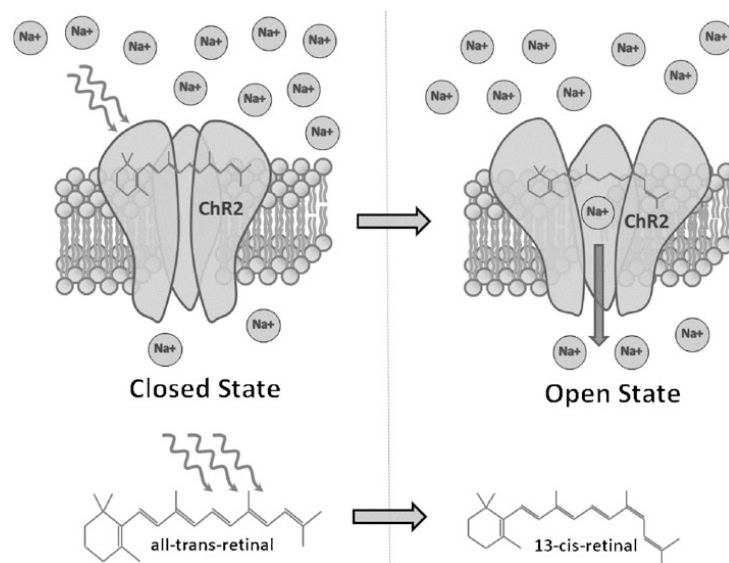


Figure 3.2: The opening-and-closing mechanism of the ChR2 protein. All-*trans*-retinal transforms after electron-photon interaction into the high-energy 13-*cis*-retinal. As a result the channel opens. The high-energy retinal returns to the all-*trans* state in the absence of light. The channel closes (He, 2020).

Channelrhodopsin-2 (ChR2) is a seven-transmembrane, light-responsive protein. ChR2 utilizes retinal in the all-*trans* configuration in order to function. Exposure to light results in the isomerization of the all-*trans* or low-energy configuration to the 13-*cis* or high-energy configuration. As a result of the force of this conformational change, the ChR2 protein structure changes and the open channel is formed. It is a nonspecific cation channel meaning that opening of the channel allows H^+ , Na^+ , K^+ , and Ca^+ ions to passively diffuse down their concentration gradients (Carter and Shieh, 2015). An illustration of this principle can be seen in Figure 3.2. In absence of light, the retinal molecule will thermally revert to the low-energy all-*trans* state and the channel closes. The process can restart upon exposure to light. The opening and closing of the channel can happen in less than 1ms, making it possible to control the activity of excitable cells (Fenno et al., 2011; He, 2020). ChR2 is called a single-component optogenetic tool because a single protein combines 2 tasks: light sensation and ion flux. The peak absorption is $\lambda = 470$ nm (blue light) (Tønnesen and Kokaia, 2017). Short wavelengths correspond to high energy waves and these are absorbed rapidly by tissue. In this case, it is difficult to reach deeper layers of the cortex. ChR2 is therefore not ideal for in vivo experiments. Other opsins with red-shifted spectrum sensitivity are discovered like *Volvox* Chr, which allows larger penetration depths (He, 2020). Next to this, other ChR variants with specialized properties were identified to broaden the range of optogenetic possibilities. One of them is ChR2(H134R). This opsin exhibits increased photocurrents due to an improved folding and retinal binding (Rost et al., 2017).

Every opsin has its typical photocycle which includes the different functional and conformational states through which the opsin goes after illumination (Fenno et al., 2011). Therefore, understanding this cycle is necessary to be able to model the opsin's dynamics. Via patch-clamp studies and UV-visible spectroscopic data, the activation response and photocycle of ChR2 became clearer. Figure 3.3 shows a typical time course of the ChR2 current upon stimulation. The stimulation length is depicted by the blue line. Three main features can be distinguished: an initial peak with a fast decay, a steady-state plateau, and postillumination, a fast decay to the baseline. Williams et al. (2013) use five empirical measures to describe this photocurrent kinetics:

the peak current I_p and the steady-state current I_{ss} . τ_{on} , τ_{off} , and τ_{inact} respectively represent the activation, deactivation, and inactivation time constants. Applying very short stimuli obstructs the possibility for all channels to be activated before the end of the stimuli. Some channels open after the stimulus has terminated and this results in a short rise of the current after the end of the stimulus. This can thus give another type of peak than shown in Figure 3.3. Another observation is the degraded transient response when subsequent stimuli differ less than 10s (Nikolic et al., 2009; Stehfest and Hegemann, 2010). Now that the dynamics of ChR2 are known, they can be translated into a computational model.

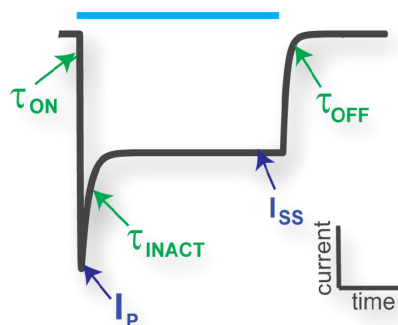


Figure 3.3: The time course of the ChR2 current as a response on light stimulation (blue line) obtained from experimental observations. Five parameters capture the amplitude and kinetics from the ChR2 current: the peak current I_p and the steady-state current I_{ss} . τ_{on} , τ_{off} , and τ_{inact} are the activation, deactivation, and inactivation time constants, respectively (Williams et al., 2013).

3.1.2 Computational optogenetics

Taking into consideration all the observations listed in Section 3.1.1 has led to the decision of working with three- or four-state Markov models (Figure 3.4) (Hegemann et al., 2005; Nikolic et al., 2006). Nagel et al. (2003) were the first to propose a three-state model. Three-state opsin models consist of an open (O), closed (C), and desensitized state (D). Desensitized means that the channel becomes less sensitive to light due to habituation. This state is necessary to account for the degraded transient response. The kinetics of the currents and relative amplitudes of the peak-plateau currents can be correctly predicted by this model (Nikolic et al., 2009). Experimental data shows a postillumination biexponential decay for wild type ChR2. This is one of the shortcomings of the three-state model and can only be modeled by a four-state opsin model. Another limitation is the need for light-dependent deactivation and recovery rates. Hegemann et al. (2005) proposed a four-state Markov model for ChR1. A few years later, Bamann et al. (2008) did a spectral analysis of ChR2 by stimulating it with short laser pulses (Nikolic et al., 2009). They could distinguish four different relaxation processes with independent time constants. For this reason, four-state models were preferred over three-state models. Figure 3.4 on the right is a four-state model that comprises two open states (O1 and O2) and two closed states (C1 and C2). Illumination will convert the channel from a closed to an open state. The transition rates between different states are e_{12} , e_{21} , G_{d1} , G_{d2} , and G_r . Williams et al. (2013) proposed a model that differentiates itself by including voltage dependence for the relevant kinetic parameters. Previous models primarily grasped light responsiveness which made the voltage dependence merely linear. Williams et al. (2013) developed the model for the ChR2(H134R) mutant. Mono-exponential processes were used to describe transitions. This is in contrast with the biexponential decay that was observed in the wild ChR2. This model was able to simulate the experimental results with high precision. However, it comprises four differential equations, resulting in high computational demand. Schoeters et al. (2021) suggested a double two-state opsin model primarily fitted to and tested on ChR2(H134R). Compared to the model

of Williams et al. (2013) it could represent the experimental data equally good. Changing to a double two-state model reduces the number of differential equations from four to two. This results in an increased computational speed and an easier fitting procedure. Lastly, this model can be expanded to other opsin types. Of course, every model has its disadvantages. The double two-state model responds instantaneous to light, overestimating the injected current at very short pulses. Furthermore, the pH and ion concentrations are not included. Eventually, the advantages of the double two-state model of Schoeters et al. (2021) together with the accurate representation of the experimental results led to the decision of working with this model. It is further elaborated in Section 4.2.

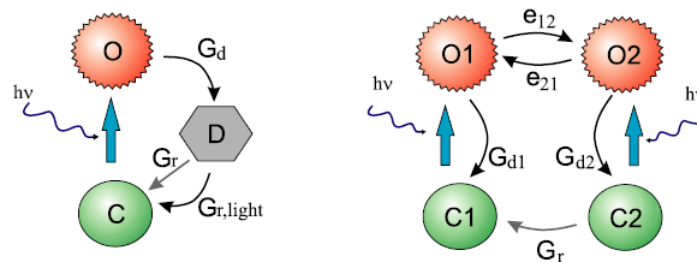


Figure 3.4: Three- (left) and four- (right) state models for the photocycle of ChR2. Different states are O(open), C(closed), D(desensitized). The four-state model consists of two open and two closed states. (Nikolic et al., 2009)

3.2 Subcellular optogenetics

One of the advantages of optogenetics was the cell-type specificity. Specific cell-types or neuronal populations can be targeted by using promoters or by spatially controlling the virus injection (Fenno et al., 2011). Even more, it is possible to target subcellular neuronal structures. Rost et al. (2017) have reviewed the most important subcellular targeting strategies. Based on this review, an overview will be given, followed by the usefulness of working subcellular. The section ends with the most relevant studies on computational subcellular optogenetics with the aim of situating this dissertation in existing literature.

There are two ways to obtain spatial selectivity when stimulating a neuron: genetically targeted expression and focusing the light beam (Nikolic et al., 2013). The genetically targeted expression can be obtained by modifying the opsin to restrict its expression to desired locations on the neuron. Rost et al. (2017) give some interesting examples for every compartment.

Axonal targeting can be obtained by fusing ChR2 to an artificial binding domain for myosin (ChR2-MVIBD-GFP). This is also called targeted axonal trafficking. Grubb and Burrone (2010) invented a way to target with an even greater spatial selectivity. They added the ankyrinG-binding loop of voltage-gated sodium channels (NavII-III) to the intracellular terminus of ChR2. This resulted in a localized ChR2 expression in the axonal initial segment (AIS). Even though the actual targeting succeeded, it was impossible to initiate APs most likely because of its sparse expression at the AIS together with the small single-channel conductance of ChR2.

Opposite, it is sometimes desired to exclude the axon from ChR2 expression. Lewis et al. (2009) obtained enrichment of the somatodendritic compartment by attachment of the myosin Va-binding domain (MBD) of melanophilin to ChR2. This successfully resulted in reduced spiking by axonal illumination and enhanced dendritic photocurrents. Postsynaptic densities could be targeted by the C-terminal addition of the short PDZ domain binding motif ETQV to ChR2 (Gradinaru et al., 2007; Rost et al., 2017).

More recently, Hamada et al. (2021) found a ChR2 modification that resulted in localization at the presynaptic axon terminals. ChR2 tagged by the metabotropic glutamate receptor 2

(mGluR2) C-terminal domain fused with a proteolytic motif (mGluR2-PA) could achieve this targeting without disturbing the normal transmission. In general, modifying ChR2 by the addition of trafficking motif tags to obtain spatial selectivity is only successful when the function of the optogenetic tool is not impaired.

The question now remains for what reason specific subcellular compartments are targeted. A uniform distribution of opsins in the neuron can result in excessive and unphysiological ion fluxes when a wide-field illumination is used. For example, ChR2 is permeable to calcium so a uniform distribution of ChR2 can lead to unrealistic calcium concentrations. Clustering the opsin can avoid this problem. There are also compartment-specific advantages. The AIS is the most excitable portion of the neuron due to the high voltage-gated sodium channels (Rost et al., 2017; Grubb and Burrone, 2010). Localization of the optogenetic tool where the AP initiates can therefore be interesting to manipulate the voltage. For some experiments, it is desired to avoid the axon and only excite the somatodendritic compartment. By doing this, activation of passing fibers can be avoided and enables exciting specific neuronal subpopulations with a higher precision (Rost et al., 2017). And lastly, presynaptic axon terminals can be chosen to enhance presynaptic activation and to study the functional effects of ChR2 (Hamada et al., 2021). Hamada et al. (2021) also state that lower levels of photostimulation were needed after targeting ChR2 to the axon terminals. Summarized, compartment-specific optogenetics allow to conduct experiments with higher precision and is furthermore used to study the functional and computational processes performed by the cell. Important to mention is the technique that is used to visualize the spatial distribution of ChR2 on the neuron. ChR2 is clustered with a fluorescent protein like YFP and GFP. This fluorophore-bound version of ChR2 can be envisioned by using a scanning confocal microscope (Grubb and Burrone, 2010).

The second way to stimulate the neuron at very localized points is by focusing the light beam. Micro-LED arrays can be used to stimulate multiple subcellular compartments (Nikolic et al., 2013). Grossman et al. (2010) invented this technique because of the lack of optical devices that could provide 2D stimulation with sufficient irradiance and high spatiotemporal control. This micro-LED array enables micrometer and millisecond resolution. It is even possible to illuminate with sophisticated patterns. Grossman et al. (2010) stated that this 2D stimulation opens the possibility to investigate basic computational functions of individual neurons, like spike-time-dependent plasticity or the backpropagation of action potentials (bAP). Spike-Timing-Dependent Plasticity (STDP) is the change in synaptic efficacy after multiple repetitions of forced spiking. This change is a function of the difference between the firing times of the pre- and postsynaptic neuron (Gerstner et al., 2014). Backpropagation of APs is the active conduction along the neuronal dendrites produced by the initiation of an axonal AP (Gasparini and Migliore, 2013). To stimulate only one subcellular compartment, e.g. soma, the laser coupled optical fibers can be used (Grossman et al., 2013).

Previously mentioned studies mainly conducted in vitro and in vivo experiments to investigate the response of cells to subcellular targeting. In this dissertation, the location-dependent effects of optogenetic stimulation are studied using multi-compartment models. Previously, Nikolic et al. (2013) and Grossman et al. (2013) conducted very similar computational studies.

Grossman et al. (2013) investigated via simulations how the spatial pattern of excitation affects the response of ChR2 expressing neurons. The simulations were done using NEURON. Four illumination strategies were used: focal somatic, apical dendritic, focal AIS, and whole cell illumination. The neuron model of Hay et al. (2011) was used to model a cortical layer V pyramidal neuron. Channelrhodopsin-2 was modeled with a new six-state model inspired by Nikolic et al. (2009). The illumination strategies consist of different illuminated areas. When a constant ChR2 density is assumed, different amounts of photo-current are injected, which makes it difficult to compare the results. This hurdle was avoided by tuning the ChR2 density (\bar{g}_{ChR2}) in such a way that they all give the same threshold irradiance for spiking. The ChR2

density for whole cell illumination (area=31.192 μm^2 , \bar{g}_{ChR2} =2.1 pS/ μm^2) is therefore much lower compared to that of the soma (area=1.131 μm^2 , \bar{g}_{ChR2} =35.0 pS/ μm^2). They found that the illumination strategy has an important effect on the kinetics of spiking output and the efficiency of stimulation:

1. *Whole cell illumination* synchronizes the depolarization of the dendritic tree and the soma. Observed spiking characteristics are an increased bursting rate and enhanced backpropagation of APs. This is the most efficient illumination given the low ChR2 density that is required for the same irradiance threshold. However, due to the larger area, the total number of channels is of similar magnitude as those of the other illumination strategies.
2. *Axonal stimulation*. No prolonged spiking was observed when illuminating only the axon. Interesting for this compartment is to analyze neurodegenerative processes like axon demyelination by adapting the membrane capacitance. They found that the threshold irradiance increases in proportion to the demyelination level of an axon.
3. Comparing the waveforms of *somatic illumination* and *apical dendritic illumination* showed that there is a stronger and more prolonged depolarization of the dendrites in the case of the apical dendrite illumination. For somatic illumination, a later AP can be observed due to backpropagation and there is a quick repolarization. For whole cell illumination, the effects are combined (last panel).
4. Grossman et al. (2013) also found that bAP had higher amplitudes and shorter latencies in the case of the whole-cell illumination. Modulation of the bAP is used to spatially modulate the direction and amplitude of spike time-dependent plasticity protocols. Co-excitation of the dendritic tree and the soma could enhance the conductivity of bAPs.

Nikolic et al. (2013) conducted a similar study. They used the same four different illumination types but next to channelrhodopsin-2 (ChR2), also halorhodopsin (NpHR) was used as an optogenetic tool. Therefore, both optical activation and silencing were possible. Nikolic et al. (2013) also worked with a layer V cortical pyramidal cell and modeled it using the same neuron model of Hay et al. (2011). ChR2 was described by a six-state model and NpHR by a three-state model. The NEURON simulation tool was used. Only the effects of activating NpHR and co-activating NpHR and ChR2 are studied here since Grossman et al. (2013) examined ChR2 on its own. NpHR turned out to hyperpolarize the best in the case of whole cell illumination. Apical dendritic illumination showed some hyperpolarization but was insufficient to prevent the membrane voltage from reaching the threshold. Illumination at the soma or axon did not result in a significant hyperpolarization of the membrane potential. Activation of both opsins resulted in different scenarios depending on the relative locations of each illumination. There was a slight balance towards depolarization. By using the two opsins, two opposing effects can be combined (excitation and inhibition). This enables controlling the cell's firing at millisecond precision.

3.3 Hurdles of optogenetics

Optogenetics almost exist for twenty years. It has brought major advances in the field of neuroscience and is widely used to study signal processing in the brain. Yet, clinical trial design still faces a lot of challenges. For this reason, only clinical trials for Retinitis Pigmentosa have been conducted up until now. A first hurdle is the invasiveness. For both the introduction of the viral vector and the implantation of a medical device that can deliver sufficient light, a neurosurgical procedure is necessary (White et al., 2020). Retinitis Pigmentosa is treated in the eye, where ambient light serves as stimulation tool. In this way, both the difficult access to the brain to inject the vector and the implantation of an optical device can be avoided (White et al., 2020). Secondly, the brain tissue is directly exposed to light. Prolonged stimulation can lead

to the production of heat. Stujenske et al. (2015) found that stimulation with high-intensity light can result in an elevation of the local firing rate, even without any expression of opsins. They described a realistic model to simulate light and heat propagation during optogenetic experiments. A third difficulty is the generalization from a mouse brain to the human brain. The volume of a human brain is a 1000-fold bigger (Tønnesen and Kokaia, 2017). All experiments done on rodents that provide proof of principle for optogenetics are therefore difficult to extend to humans. Light in the visible range is quickly absorbed in brain tissue so the use of optical fibers is necessary to target deeper structures. These optical fibers need to be designed in order to minimize brain damage and immune responses. A possible solution to the quick absorption is the use of red-shifted opsins. Red light has a longer wavelength and will penetrate deeper into the brain tissue (Tønnesen and Kokaia, 2017; Tung et al., 2016).

This dissertation aims at contributing to the conquest of these hurdles. A better understanding of the neuronal responses after subcellular targeting can result in a more efficient stimulation of the neuron. Hamada et al. (2021) already showed that lower levels of photostimulation were possible due to the neuronal targeting with high spatial selectivity. Despite all these challenges, White et al. (2020) expects the first human trials to occur within the next decade due to the hard work of several groups.

Chapter 4

Reduced-morphology neuron model

This chapter comprises the investigation of the location-dependent effects on the smallest scale. With the reduced-morphology model of Cutsuridis and Poirazi (2015), modified by Tomko et al. (2021), it is possible to focus on individual sections. The aim is to find stimulation strategies that can improve the efficiency of optogenetic excitation. Primarily, the generic response of the CA1 pyramidal neuron on different optogenetic stimulation strategies, is studied. The stimulation strategies are characterized by the location on which ChR2(H134R) is expressed. Thereafter, the focus will shift to a single basal dendrite. Additionally, the impact of the symmetry on the results is studied. Simulations are done with the NEURON simulation platform, further elaborated in Section 4.3. The double two-state opsin model of Schoeters et al. (2021) is used to model ChR2(H134R). This opsin channel is inserted into the neuron model: the modified version of the Cutsuridis and Poirazi (2015) model by Tomko et al. (2021) (CP15TK21). The results are represented in Section 4.4 and are discussed in Section 4.5.

4.1 Cutsuridis and Poirazi model by Tomko: CP15TK21

To study the location dependent effects of the optogenetic expression, we need a neuron model in which the opsin channel can be implemented. Many different models have been developed for the CA1 pyramidal neuron, from morphological simple to very detailed models. Next to the morphology, also the composition of ion channels and biophysical properties can be adapted. To study the impact of the complexity of the neuron model on the results, a comparison is made between the results obtained by a reduced-morphology model (Chapter 4) and a full-morphology model (Chapter 5). This section elaborates on the neuron's morphology, the ion channel composition, and the model's ability to reproduce the key characteristic properties of the CA1 pyramidal neuron, which is studied by Tomko et al. (2021).

Primarily, the model of Cutsuridis and Poirazi (2015) (CP15) was chosen as reduced-morphology model. This model was used in a computational study on how theta modulated inhibition can account for the long temporal windows in entorhinal-hippocampal loop (Cutsuridis and Poirazi, 2015). A representation of the morphology is shown in Figure 4.1, together with the 19 different section names. These are inspired by the corresponding sublayer of the cornu ammonis (see Section 2.1.1) in which they are located. The morphology is symmetric and the right and left side are respectively indicated by suffix one and two. Summarized, there are four basal dendrites (3-6) and three apical dendritic trunk sections (7-9). Four oblique, apical dendrites are connected to the apical trunk (10-13) and six sections (14-19) form the dendritic tuft. Some sections consist of multiple segments. The lengths, diameters, total surfaces, and number of segments can be found in Table A.1 in Appendix A.

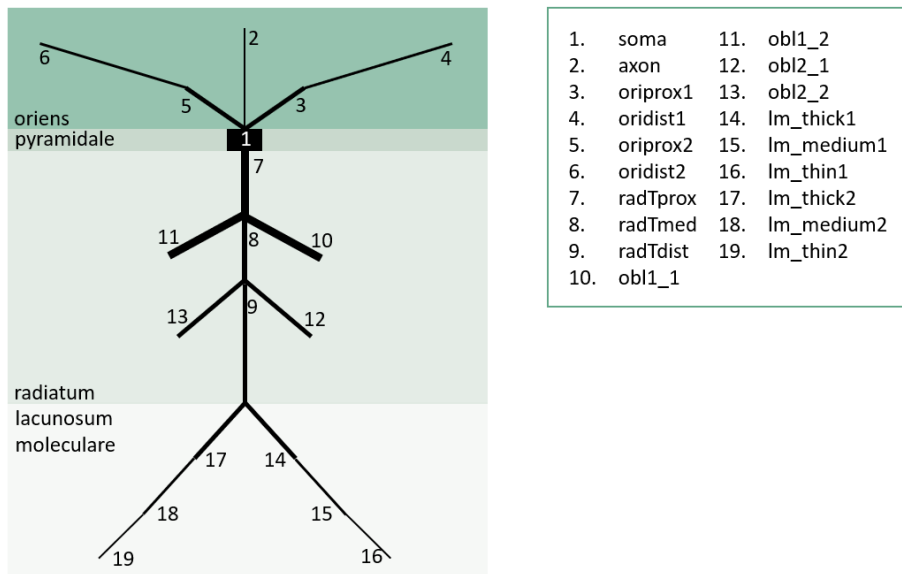


Figure 4.1: CA1 pyramidal neuron morphology of the CP15TK21 model with the corresponding section names (Cutsuridis and Poirazi, 2015; Tomko et al., 2021).

The biophysical properties of the original version of the CP15 model were adapted from the Poirazi model (Poirazi et al., 2003a,b; Cutsuridis and Poirazi, 2015). However, it quickly became clear that the excitability of this model was not sufficient. Recently, Tomko et al. (2021) proposed a new reduced-morphology model (To21) in which they changed the content of the ion channels of a reduced-morphology model based on those of the full-morphology model of Migliore et al. (2018) (M18). This new model had improved physiological properties and was able to capture key physiological features of CA1 pyramidal neurons with a shorter computational time. Based on these conclusions, the same was done for CP15 which eventually led to the modified version of the Cutsuridis and Poirazi (2015) model by Tomko et al. (2021): CP15TK21. It can be found on modelDB¹. Most importantly, this model has a higher excitability, making it easier to perform the computational study with. Summarized, the morphological properties of CP15 are preserved but the ion channel composition is replaced with those from M18. Therefore, the biophysical properties explained below apply for both the reduced-morphology model (CP15TK21) and the full-morphology model (M18), elaborated in Chapter 5. In total, there are twelve different ion currents and a calcium accumulation mechanism. The Hodgkin-Huxley model, as described in Section 2.2.2, is used to describe the currents:

$$i_L = g_L(V - E_L) \quad (4.1)$$

$$i_{Na} = g_{Na}m^3h(V - E_{Na}) \quad (4.2)$$

$$i_{Kdr} = g_{Kdr}n(V - E_K) \quad (4.3)$$

$$i_{Kad} = g_{Kad}nl(V - E_K) \quad (4.4)$$

$$(4.5)$$

¹<https://github.com/tomko-neuron/HippoUnit>

$$i_{Kap} = g_{Kap}nl(V - E_K) \quad (4.6)$$

$$i_{Kmb} = g_{Kmb}m(V - E_K) \quad (4.7)$$

$$i_{Hd} = g_{Hd}l(V - E_H) \quad (4.8)$$

$$i_{Kca} = g_{Kca}m^3(V - E_K) \quad (4.9)$$

$$i_{Kcagk} = g_{Kcagk}o(V - E_K) \quad (4.10)$$

$$i_{Cal} = g_{Cal}m^2(V - E_{Ca}) \quad (4.11)$$

$$i_{Can} = g_{Can}m^2h(V - E_{Ca}) \quad (4.12)$$

$$i_{Cat} = g_{Cat}m^2h(V - E_{Ca}) \quad (4.13)$$

With $g_L, g_{Na}, g_{Kdr}, g_{Kad}, g_{Kap}, g_{Kmb}, g_{Hd}, g_{Kca}, g_{Kcagk}, g_{Cal}, g_{Can}, g_{Cat}$ the maximal conductances and $E_L, E_{Na}, E_K, E_H, E_{Ca}$ the equilibrium potentials. The definition of the currents together with the sections in which they are present, are summarized in Table 4.1. The rate functions of the gating variables can be found on modelDB². The activation and inactivation gating variables change according to Eq. 2.11. The conductance is mainly uniformly distributed except for the peak conductance of $i_{Ka(d/p)}$ and i_{Hd} , and the equilibrium potential of the passive current E_L . These are calculated for each section based on its distance from the soma and described by a linear function. The parameters were fitted during the M18 optimization process (Migliore et al., 2018; Tomko et al., 2021). The uniformly distributed parameters can be found in Table A.2 in Appendix A. The membrane potential is described according to Eq. 2.10:

$$C_m \frac{dV}{dt} = -i_{Na} - i_{Kdr} - i_{Kad} - i_{Kap} - i_{Kmb} - i_{Hd} - i_{Kca} - i_{Kcagk} - i_{Cal} - i_{Can} - i_{Cat} - i_L \quad (4.14)$$

All sections containing calcium channels include a simple calcium accumulation mechanism, with a single exponential decay of 100 ms (Migliore et al., 2018). The calcium dynamics are described by:

$$\frac{d[Ca]_i}{dt} = -0.52 \cdot i_{[Ca]} + \frac{[Ca^{2+}]_0 - [Ca^{2+}]_i}{\tau_{Ca}} \quad (4.15)$$

With $i_{[Ca]}$ the sum of all calcium currents, τ_{Ca} the calcium decay time constant and $[Ca^{2+}]_0$ the intracellular calcium concentration at rest. The values of τ_{Ca} and $[Ca^{2+}]_0$ can be found in Table A.2 in Appendix A. E_{Ca} is not specified because it depends on the local calcium concentration.

²<https://github.com/tomko-neuron/HippoUnit>

Current	Definition	Sections
i_L	Leak current	Soma, rad, lm, ori, axon
i_{Hd}	H current	Soma, rad, obl, lm, ori
i_{Na}	Na ⁺ current for axon	Soma, rad, lm, ori, axon
i_{Kap}	Proximal A-type K ⁺ current	Soma, axon
i_{Kad}	Distal A-type K ⁺ current	Rad, obl, lm, ori
i_{Kdr}	Delayed rectifier K ⁺ current	Soma, rad, lm, ori, axon
i_{Kmb}	M-type K ⁺ current	Soma, axon
i_{Kca}	Ca ²⁺ -activated sAHP K ⁺ current	Soma, rad, obl, lm, ori
i_{Kcagk}	Ca ²⁺ -activated K ⁺ current	Soma, rad, obl, lm, ori
i_{Cal}	HVA L-type Ca ²⁺ current	Soma, rad, obl, lm, ori
i_{Can}	HVA N-type Ca ²⁺ current	Soma, rad, obl, lm, ori
i_{Cat}	LVA T-type Ca ²⁺ current	Soma, rad, obl, lm, ori
cai	Calcium accumulation	Soma, rad, obl, lm, ori

Table 4.1: The current types present in the M18 model and CP15TK21 model with their corresponding sections (Migliore et al., 2018). Rad, obl, ori, and lm are the respective abbreviations of stratum radiatum, oblique, stratum oriens, and stratum lacunosum-moleculare.

4.2 ChR2(H134R) model: double two-state opsin model

The consideration elaborated in Section 3.1.2 finally led to the decision of working with the double two-state opsin model (22OM) of Schoeters et al. (2021). Schoeters et al. (2021) made an extensive comparison of their model with the accurate four-state Markov model (4SB), derived by Williams et al. (2013). They showed that the double two-state model is able to represent experimental data with high accuracy. The performances were overall comparable to those of the 4SB model and sometimes slightly better. The 22OM model consists of two differential equations less than the 4SB model, resulting in an increased computational speed. In my research, it is, obviously, preferred to have faster simulations. However, in the case of very short light pulses ($PD < \tau_{on}$), the 22OM model might overestimate the injected current since it has an instantaneous response to light.

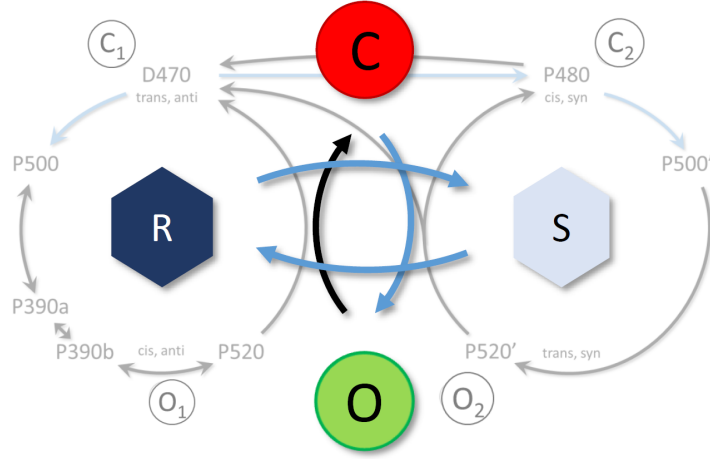


Figure 4.2: Double two-state opsin model (22OM) derived by Schoeters et al. (2021). The O-C state pair accounts for the open-closing mechanism. O and C respectively refer to open and close. Dark-light adaptation is captured by the mathematical R-S state pair. The light dependent rates are indicated by blue arrows. The ChR2 photocycle is visualised in the background.

The double two-state model is represented in Figure 4.2 on top of the ChR2 photocycle. There are two independent two-state pairs: O-C and R-S. After a long time of darkness, the channel is closed (C) and dark adapted. Upon stimulation, the opsin goes through different functional and conformational changes and ends up in its open (O) state. As discussed in Section 3.1.1, there is a degraded transient response when subsequent stimuli differ less than 10s. Molecules can adapt to both light and darkness. Light-adapted molecules have a lower conductance than dark adapted ones. When the photostimulation is stopped, the molecules need a recovery period to return to their dark adapted states, which is of the order of seconds (Nikolic et al., 2009). In this model, the change in conductance due to light-dark adaptation is captured by the mathematical model states R and S. Their relationship with the physical dark adapted and light adapted states is given by:

$$R = \frac{g_{ChR2} \cdot DA + g_{LA} \cdot LA}{g_{ChR2}} \quad (4.16)$$

$$S = 1 - R \quad (4.17)$$

The parameter g_{LA} is the conductance of a light adapted channel. LA and DA are the probabilities of the opsin molecules to be in a light or dark adapted state, respectively. So, in a fully dark adapted state, $R=1$ and $S=0$. After the transition to a fully light adapted state, $R = g_{LA}/g_{ChR2}$, and $S = 1 - g_{LA}/g_{ChR2}$. An expression for the ChR2 photocurrent is obtained via the same reasoning as for the Hodgkin-Huxley ionic currents (Eq. 2.6).

$$i_{ChR2} = g_{ChR2}G(V)(O \cdot R)(V - E_{ChR2}) \quad (4.18)$$

The difference $(V - E_{ChR2})$, with E_{ChR2} the equilibrium potential, is the driving force and g_{ChR2} is maximal specific conductance of a fully dark adapted channel. Williams et al. (2013) describe the importance of a rectification function $G(V)$ to include the strong inward current-voltage rectification at voltages above 0 mV. The photocurrent is maximal in the open, dark-adapted state ($O=1$ and $R=1$). The derivatives of the states are defined as:

$$\frac{dO}{dt} = \frac{O_\infty(I, V) - O(t)}{\tau_O(I, V)} \quad (4.19)$$

$$\frac{dR}{dt} = \frac{R_\infty(I, V) - R(t)}{\tau_R(I, V)} \quad (4.20)$$

With O the fraction of molecules in the open state, for which O_∞ and τ_O are the corresponding equilibrium and time constants, respectively. Similarly, R_∞ and τ_R are the corresponding equilibrium and time constants of state R . Schoeters et al. (2021) primarily fitted the model to the data reported by Williams et al. (2013) on the ChR2(H134R) opsin. The fitting procedure was accelerated by the use of an analytical solution to the above set of differential equations. The closed form analytical expression is only valid under voltage clamp conditions and a rectangular optical pulse stimulation with constant light intensity. The experimental data should meet these conditions in order to use the analytical solution. The intensity and voltage dependence of the time-constants τ_O and τ_R are fit separately. Sigmoidal functions on the log scale and logistic regression are respectively used for the intensity and voltage dependence. Finally, the dependencies are combined by a reciprocal addition since this gave better results than a multiplication. Eq. 4.21-4.24 give the relationships for the time constants, with $p_i, i = 1 \rightarrow 6$ the unknown parameters. In the next step, the equilibrium constants, O_∞ and R_∞ , and the parameters of the rectification function $G(V)$ are fit. O_∞ and R_∞ are only dependent on the intensity because the main voltage dependence is covered by $G(V)$. These last relationships are given in Eq. 4.25-4.27.

$$\tau_O(I) = \frac{p_3}{1 + \exp(p_1/p_2) \cdot I^{1/(p_2 \cdot \ln(10))}} \quad (4.21)$$

$$\tau_R(I) = p_1 \left(1 - \frac{p_2}{1 + \exp(p_3/p_4) \cdot I^{-1/(p_4 \cdot \ln(10))}} - \frac{1 - p_2}{1 + \exp(p_5/p_6) \cdot I^{-1/(p_6 \cdot \ln(10))}} \right) \quad (4.22)$$

$$\tau_X(V) = \frac{p_1}{1 + \exp(-(V - p_2)/p_3)}, \quad X = O, R \quad (4.23)$$

$$\tau_X(I, V) = [(\tau_X(I))^{-1} + (\tau_X(V))^{-1}]^{-1}, \quad X = O, R \quad (4.24)$$

$$O_\infty(I) = \frac{1}{1 + \exp(p_1/p_2) \cdot I^{-1/(p_2 \cdot \ln(10))}} \quad (4.25)$$

$$R_\infty(I) = 1 - \frac{p_3}{1 + \exp(p_1/p_2) \cdot I^{-1/(p_2 \cdot \ln(10))}} \quad (4.26)$$

$$G(V) = \frac{p_1 \cdot (1 - p_2 \exp(-(V - E_{ChR2})/p_3))}{V - E_{ChR2}} \quad (4.27)$$

Parameters $p_i, i = 1 \rightarrow 6$ are calculated by minimization of the cost function followed by a global optimization. Further details of the cost function and fitting procedure can be found in the original paper of Schoeters et al. (2021). The final parameters are given in Table 4.2. E_{ChR2} and g_{ChR2} are set to zero and one, respectively.

Intensity dependence of time constant of state O			Voltage dependence of time constant of state O			Intensity dependence of time constant of state R					
$\tau_o(I)$			$\tau_o(V)$			$\tau_R(I)$					
p_1	p_2	p_3	p_1	p_2	p_3	p_1	p_2	p_3	p_4	p_5	p_6
1.81	1.17	0.021	23.14	-0.39	13.19	10	0.56	-1.58	0.87	1.96	0.11
Voltage dependence of time constant of state R			Equilibrium of state O		Equilibrium of state R			Rectification function G(V)			
$\tau_R(V)$			$O_\infty(I)$		$R_\infty(I)$			G(V)			
p_1	p_2	p_3	p_1	p_2	p_1	p_2	p_3	p_1	p_2	p_3	
99.74	-38.69	12.02	3.38	0.62	1.96	0.12	0.77	10.77	1.25	44.52	

Table 4.2: The final 22OM model parameters of the ChR2 mutant, ChR2(H134R), for the double reciprocal addition combination of time constant dependencies (Eq. 4.24) (Schoeters et al., 2021).

Throughout this study, the time constants and time are expressed in ms, the membrane potential in mV and the intensity in W/m^2 . The maximal conductance of a dark adapted channel is redefined since $G(V)$ has a factor p_1 :

$$\bar{g}_{ChR2} = p_1 \cdot g_{ChR2} = 10.77 \cdot g_{ChR2} \quad (4.28)$$

The maximal specific conductance \bar{g}_{ChR2} is expressed in mS/cm^2 . For convenience, ChR2(H134R) is abbreviated as ChR2 in all parameter designations.

4.3 Methodology

The simulations were done via the NEURON simulation platform (Carnevale and Hines, 2006). It is a powerful simulation tool created by Hines (1993). The biologically realistic models of the CA1 pyramidal neuron and the opsin ChR2(H134R), defined in the previous two sections, are implemented in the NEURON 8.0.0 environment in Python 3.7.11. Biological models like these are characterized by nonlinearities and spatiotemporal complexities with no analytical solution. NEURON allows to handle the neuron's complex membrane currents and inhomogeneous membrane properties. Like those explained in Table 4.1 and the ChR2(H134R) channel, membrane channels are described in NMODL, a high-level language invented by Moore and Hines (1996) (Hines and Carnevale, 1997). These mechanisms are subsequently translated to C, compiled, and linked to the rest of NEURON. When all mechanisms and parameters are defined, the neuron's response to a stimulus can be simulated. The aim is to find the longitudinal spread of voltage and current along the neuron. In Section 2.3 was declared how the cable equations form the connection between voltages and currents across different compartments of the multi-compartment neuron model. In natural neuronal structures, no analytical solutions can be found for these differential equations. Therefore, a numerical approach should be used, which is in this case the Backward Euler method (Hines and Carnevale, 1997). A constant time step of 0.025 ms is used. As initial conditions, the ChR2(H134R) channel is assumed to be in a closed, dark adapted state ($R=1$, $O=0$). The initial membrane voltage is set to -70 mV and the default temperature of 6.3°C is used. The spiking activity of a neuron and the morphology of a spike can be quantified by features. In the following, the stimulation strategies are specified, continued by the features that are used to make a comparison.

4.3.1 Stimulation strategies

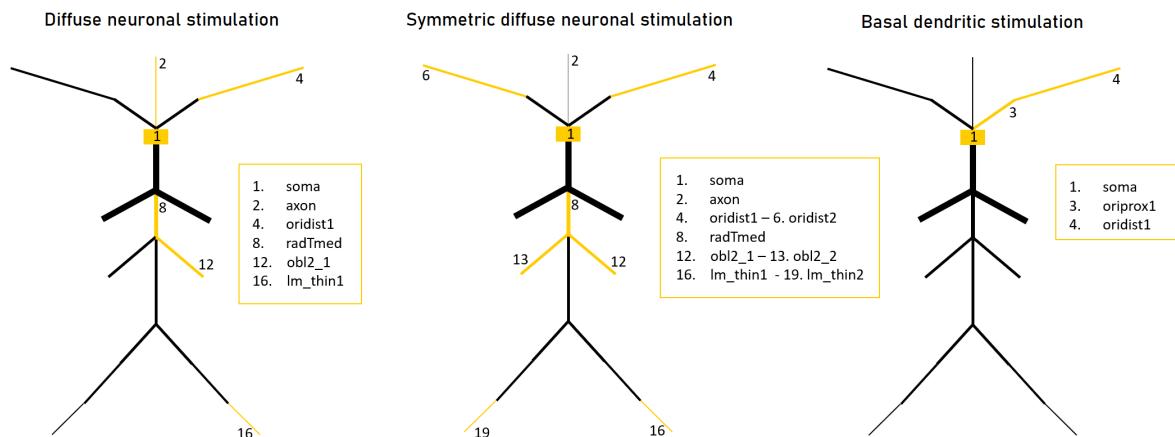


Figure 4.3: The stimulation strategies used for the CP15TK21 model. Yellow sections indicate the consecutive locations of the ChR2(H134R) channel. The opsin is uniformly distributed along the section.

In total, three different stimulation strategies are used (Figure 4.3). The yellow sections in which the ChR2(H134R) channels are consecutively inserted, are listed in the yellow box. For the first strategy, only one section per simulation is targeted. The sections are chosen diffusively across the neuron with the aim of studying the generic response of the neuron on different stimulation locations. The chosen sections are: the soma, the axon, a basal dendrite (oridist1), an apical trunk dendrite (radTmed), a radial oblique dendrite (obl2_1), and an apical tuft dendrite (lm_thin1). In Section 3.2, different possible methods were given to limit the opsin expression to certain neuronal structures. This can be obtained by genetically modifying the opsin to restrict its expression to desired locations on the neuron. However, in reality there are multiple dendrites belonging to one neuronal structure (e.g. apical dendritic tuft). In the second strategy, the symmetrical equivalent sections are therefore added. In the third, second last, and last simulation, the opsin is simultaneously inserted in two sections. This is also done to find the interaction of the symmetrical sections and the integration of the currents. The last strategy is the most specific, in which only one basal dendrite and the soma are targeted. Similar behavior is expected since the biophysics of two sections belonging to the same dendrite are almost equal. Only their dimension and the distance to the soma differ. The opsin is uniformly distributed along the targeted sections for all strategies.

4.3.2 Features

The different locations targeted in each strategy are analyzed by comparing different features. The first and most obvious feature is the mean firing rate (FR). Moor and Geit (2015) described the mean frequency of the firing rate as the number of peaks measured during the stimulation time, divided by the time to the last spike:

$$FR = \frac{\#peaks}{t_{last\ spike} - t_{start\ stimulus}} \quad (4.29)$$

This definition is however not ideal in case of initial bursting. Cortical neurons often show a distinct transient and steady-state response (Gerstner et al., 2014). For small light intensities (I) and values of the maximal specific ChR2(H134R) conductance (\bar{g}_{ChR2}), only the transient

response is observed. In case of initial bursting, a high number of peaks is divided by a small time period, resulting in a high mean firing rate. For higher intensities and maximal conductances, a regular steady-state spiking behavior results in a lower mean firing rate. It is, however, expected that the mean firing rate increases with an increasing light intensity and maximal conductance. Therefore, the firing rate is defined as the number of peaks measured during the stimulation time, divided by the stimulation duration, also called the pulse duration (PD):

$$FR = \frac{\#peaks}{PD} \quad (4.30)$$

This definition of the mean firing rate clarifies the dependency on light intensity and maximal ChR2(H134R) conductance. Contrary, it is not possible anymore to observe initial bursting behavior for small values of I and \bar{g}_{ChR2} . Important to note is that the mean firing rate is put to zero in case of a single AP. Throughout this dissertation, the mean firing rate is defined by Eq. 4.30, denoted as FR, and expressed in Hz, unless other specified. For each stimulation location in a strategy, the FR measured in the soma is calculated for a set of light intensities [1000, 2000, 3000, 4000, . . . , 10000] W/m² and maximal specific conductance [200, 300, 400, . . . , 1100] mS/cm². The maximal specific conductance is expressed per cm² surface area of the neuron. As can be seen in Table A.1 in Appendix A, each section has a different surface area so insertion of ChR2(H134R) in a section with a different surface area will result in a different maximal conductance. The amount of injected photocurrent depends on the maximal conductance. To compare different stimulation strategies, it is important to have an equal injected photocurrent and thus an equal maximal conductance. In order to solve this problem, the maximal specific conductance of a section is scaled so that the maximal conductance equals that of the soma. From now on, the maximal conductance is denoted as \bar{G}_{ChR2} and expressed in μ S.

$$\bar{G}_{ChR2_soma} = \bar{G}_{ChR2_section} \quad (4.31)$$

$$\bar{g}_{ChR2_soma} \cdot A_{soma} = \bar{g}_{ChR2_section} \cdot A_{section} \quad (4.32)$$

$$\bar{g}_{ChR2_section} = \bar{g}_{ChR2_soma} \frac{A_{soma}}{A_{section}} \quad (4.33)$$

With A_{soma} and $A_{section}$ the surface area of respectively the soma and the section for which the maximal specific conductance is scaled. The set of maximal specific conductances listed above applies for the soma and are adjusted for all sections that have a different surface area according to Eq. 4.33.

Another way to compare different locations is by comparing their strength-duration curves. Strength-duration curves plot the minimal amplitude of the stimulus, here the optogenetic pulse intensity, that is necessary to evoke a spike in function of the stimulus duration (Rattay et al., 2012; Ranck, 1975). This curve is fully described by two constants: rheobase (I_{RH}) and chronaxie (Stern et al., 2015). The rheobase is defined as the minimum intensity needed for excitation in case of infinite long pulse duration. The chronaxie is the pulse duration corresponding with an intensity of twice the rheobase. The cell's time constant is normally related to the chronaxie but this correlation fades when working with spatially extended neuron models like CP15TK21 (Stern et al., 2015). The strength-duration time constant (τ_{SD}) is more fundamental than chronaxie and only two measurements are required to calculate it (Mogyoros et al., 1996). It is defined as a measure of the rate at which the optogenetic pulse intensity increases as the duration of the stimulus is reduced to zero (Kiernan and Lin, 2012). An expression for the

strength-duration time constant is obtained via Weiss' empirical law (Weiss, 1990):

$$I \cdot PD = I_{RH}(PD + \tau_{SD}) \quad (4.34)$$

With I the optogenetic pulse intensity, I_{RH} the rheobase intensity, PD the pulse duration, and τ_{SD} the strength-duration time constant. τ_{SD} is then approximated by the limit as the pulse duration approaches zero:

$$\tau_{SD} = \frac{I[0] \cdot PD[0]}{I_{RH}} \quad (4.35)$$

With $PD[0]$ the shortest pulse duration, $I[0]$ the corresponding intensity, and I_{RH} the rheobase. So only a measurement of the intensity necessary to excite the neuron for very large and very short pulse duration is needed to compute the strength-duration time constant. The strength-duration curve is calculated for a logarithmic set of durations, i.e. 15 points between 0.1 and 100 ms. For every pulse duration, a binary search was done to find the corresponding optogenetic pulse intensity. The lower and upper boundaries were respectively 0 W/m² and 1e05 W/m² and were increased or decreased by a factor of two until an AP was measured. Accuracy of three decimal places was obtained in a final step. The bisection method was used with as condition that the upper and lower boundaries differ maximum $1e-7 + 1e-3 \cdot \text{upper boundary}$. The final optogenetic pulse intensity corresponding to the given pulse duration is the average of the upper and lower boundaries. Finally, the rheobase is found as the smallest optogenetic pulse intensity. The strength-duration time constant is approximated by formula 4.35 with $PD[0]$ equal to 0.1 ms and $I[0]$ the corresponding determined intensity. If different stimulation locations are compared, the membrane potential is always recorded at the soma, unless other specified. The applied maximal specific conductance is multiplied by the area of the section and expressed in μS because all stimulation locations have the same maximal conductance (μS) but not the same maximal specific conductance (mS/cm^2). The dependency of the rheobase and strength-duration time constant on \bar{g}_{ChR2} is plotted for the same set of maximal specific conductances applied to the soma [200, 300, 400, ..., 1100] mS/cm^2 . These values are for the same reason converted to the maximal conductance:

$$\bar{g}_{ChR2_soma} \cdot A_{soma} = \bar{G}_{ChR2} \quad (4.36)$$

$$[200, 300, \dots, 1100] \frac{\text{mS}}{\text{cm}^2} \cdot 100\pi \cdot 10^{-8} \text{cm}^2 = [0.2\pi, 0.3\pi, \dots, 1.1\pi] \mu\text{S} \quad (4.37)$$

With A_{soma} the surface area of the soma, which is equal to $100\pi \mu\text{m}^2$. The set of maximal conductances \bar{G}_{ChR2_soma} applies for all locations.

Another feature is the delay of the first action potential. Action potentials that are initiated outside of the soma need some time to propagate to the soma. In the study of location dependent effects, it is interesting to know what the delay is for an AP starting at the different stimulation locations. A positive delay corresponds with an AP that arrives at a later time in the soma. On the other hand, a negative delay can also reveal that the action potential was actually initiated in the soma. So, the delay of an action potential is the difference in time measured between the soma and the section where the action potential was initiated.

The impedance of a neuron is influenced by both the morphology of the neuron and the presence of voltage-gated conductances in the cell membrane (Káli and Zemankovics, 2012). The

input impedance describes the local change in membrane potential at the site of the input current (Dewell and Gabbiani, 2018). The dendrites of the neuron have different geometries and voltage-gated conductances, resulting in different input impedances depending on the location on the neuron. Therefore, the input impedance is determined for the different stimulation locations. The class 'Impedance' of NEURON was used. An oscillatory current stimulus of different frequencies is injected. A logarithmic set of 20 frequencies is used between 0.1 Hz and 100 Hz. Higher frequencies were not used because the number of segments per sections is not optimized for those frequencies. The input impedance is calculated 200 ms after the onset of the stimulus, after the transient response, and is defined as the absolute amplitude of $v(x)/i(x)$, with x the measuring location.

4.4 Results

Diffuse neuronal stimulation

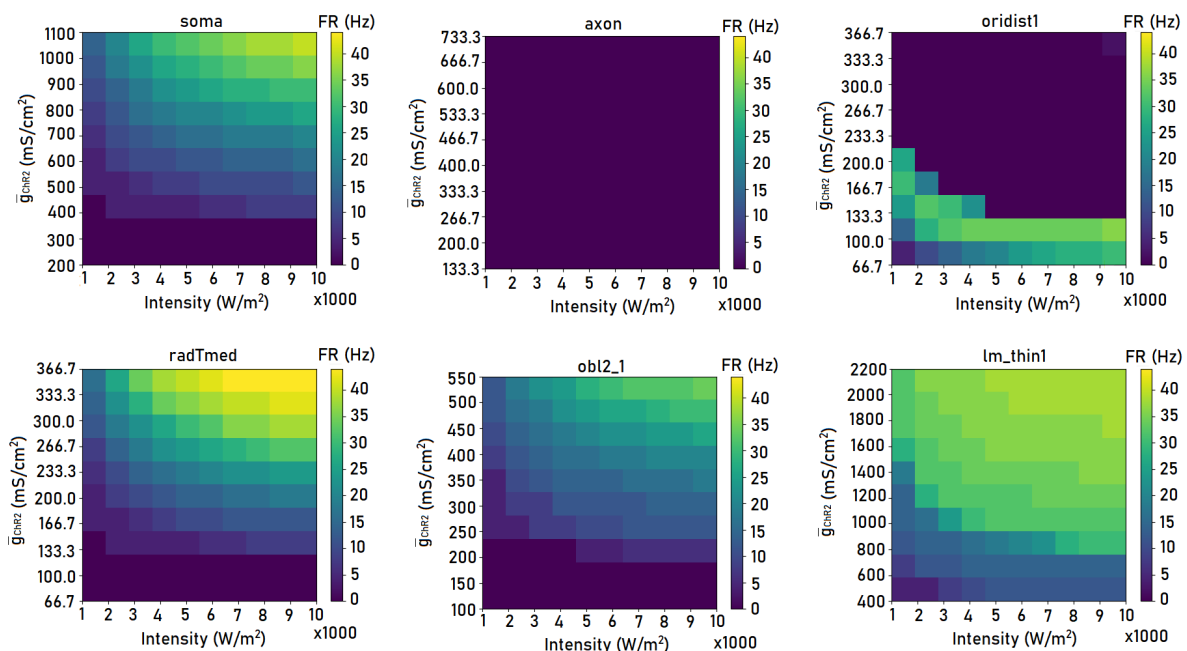


Figure 4.4: 2D colorplots of the mean firing rate, calculated according to Eq. 4.30, in function of the optogenetic pulse intensity and maximal specific conductance of Chr2(H134R). A continuous pulse of 500 ms is used. The mean firing rates are recorded in the soma for each stimulation location of the diffuse neuronal stimulation strategy, indicated in the title of the surface plots.

The opsin is consecutively inserted in the soma, axon, oridist1, radTmed, obl2_1, and lm_thin1. It is uniformly distributed along the section. The mean firing rate is calculated according to Eq. 4.30 for a set of optogenetic pulse intensities and maximal specific conductances of the Chr2(H134R) channel with a pulse duration of 500 ms. The results are visualized in 2D colorplots in Figure 4.4. Intensities are varied on the x-axis and maximal specific conductance on the y-axis. Each section has different values on the y-axis because of the surface area scaling factor (Eq. 4.33), explained in Section 4.3. The total maximal conductance is thereby equal for all plots: $[0.2\pi, 0.3\pi, \dots, 1.1\pi] \mu\text{S}$. The mean firing rate varies between 0 and 44 Hz. For all locations, except of the axon and oridist1, the mean firing rate increases for increasing values of the intensity and the maximal specific conductance. Placement of the opsin in the axon gives zero mean firing rates for all intensities and maximal conductances. Mean firing rates of around

30 Hz are measured in the soma when the opsin is placed in oridist1 for low values of \bar{g}_{ChR2} (below 133.3 mS/cm^2). Higher values result in a FR of zero. The highest FR is measured if the opsin is located at radTmed, which is a central apical trunk dendrite. The distance to the soma of the apical section radTmed, obl2_1, and lm_thin1, are respectively $188.33 \mu\text{m}$, $288.33 \mu\text{m}$, and $633.78 \mu\text{m}$. A remarkably higher mean firing rate is observed for lm_thin1 compared to obl2_1.

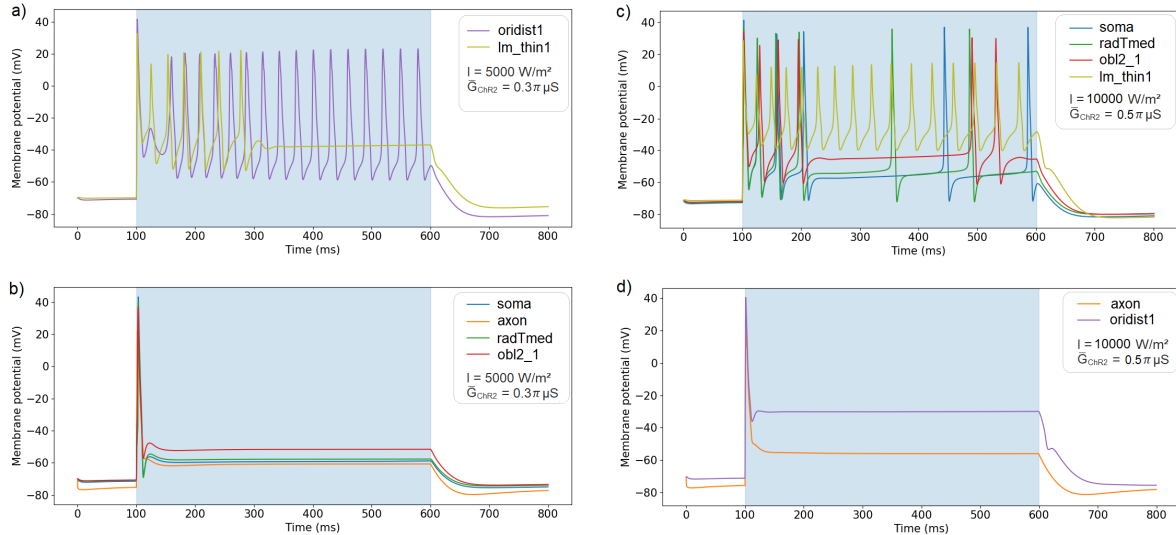


Figure 4.5: The membrane potential (mV) in function of time (ms) for two different optogenetic stimuli. A continuous pulse with pulse duration 500 ms and intensity 5000 W/m^2 was used in a) and b) and is indicated as the blue area. The opsin is located in the section indicated in the legend with a maximal ChR2(H134R) conductance of $0.3\pi \mu\text{S}$. The membrane potential is measured at the center of this section. A similar optogenetic stimulus was used to obtain (c) and (d) but with a higher intensity (10000 W/m^2) and maximal opsin conductance ($0.5\pi \mu\text{S}$). The sections for which more than one AP was measured are plotted in (a) and (c), the others in (b) and (d).

The mean firing rate reveals only a part of the membrane potential trace. Firing patterns observed in neuronal responses often show a distinct transient and steady-state part (Gerstner et al., 2014). Two combinations of optogenetic pulse intensity and maximal conductance were selected to observe the firing pattern for different stimulation locations. The membrane potential is recorded in the same section as where the opsin is located. This was done because the membrane potential influences the functioning of the opsin channel. The optogenetic pulse is continuous with a duration of 500 ms. Figure 4.5 (a) and (b) show the membrane potential traces for $I = 5000 \text{ W/m}^2$ and $\bar{G}_{\text{ChR2}} = 0.3\pi \mu\text{S}$. The blue area covers the time for which the optogenetic stimulation was present. In the soma, axon, radTmed, and obl2_1, only one AP is measured (Figure 4.5(b)). Their membrane potentials are elevated during the remaining time of the optogenetic stimulus. A slightly higher plateau value is measured in obl2_1. Removing the stimulus results in a hyperpolarization, i.e. the membrane potential declines further than the resting membrane potential. A higher activity was measured in the other two sections, oridist1 and lm.thin1 (Figure 4.5(a)). The first AP measured in both sections is higher in amplitude. A tonic firing was observed in oridist1, covering the whole optogenetic stimulus time, followed by a hyperpolarization upon removal of the stimulus. Placement of the opsin in lm.thin1 results in a shorter spike train. Thereafter, it reaches a plateau value of -37 mV , again followed by hyperpolarization upon removal of the stimulus. Figure 4.5 (c) and (d) show the membrane potential traces for a higher intensity and maximal conductance: $I = 10000 \text{ W/m}^2$, $\bar{G}_{\text{ChR2}} = 0.5\pi \mu\text{S}$. The upper plot consists of the sections in which more than one AP was measured. When the opsin is localized in the soma, an initial burst can be observed. After about

200 ms of silence, the neurons starts to fire again with a lower firing rate. Further increasing the maximal conductance results in a shorter period of silence and a higher firing rate for both the initial burst and the tonic steady-state firing. The same behavior is observed when the opsin is located in the apical trunk dendrite (radTmed) and radial oblique dendrite (obl2_1). However, a different firing pattern is observed in the farthest dendrite of the dendritic tuft (lm_thin1). The firing rate is higher compared to the other sections and there is no initial burst but only regular spaced spikes. Remarkable is the difference equilibrium potentials. Lm_thin1 is the most depolarized, followed by obl2_1, radTmed, and the soma. The membrane potentials of the other two sections are shown in Figure 4.5 (d). The tonic firing that was measured in oridist1 for a lower optogenetic pulse intensity and maximal conductance has now changed to only one action potential. During the stimulus time, the membrane potential in oridist1 is depolarized (-30 mV). And lastly, axonal stimulation results again in one AP followed by a depolarized membrane potential. A slightly higher depolarization is observed compared to the first stimulus, i.e. -56 mV versus -61 mV.

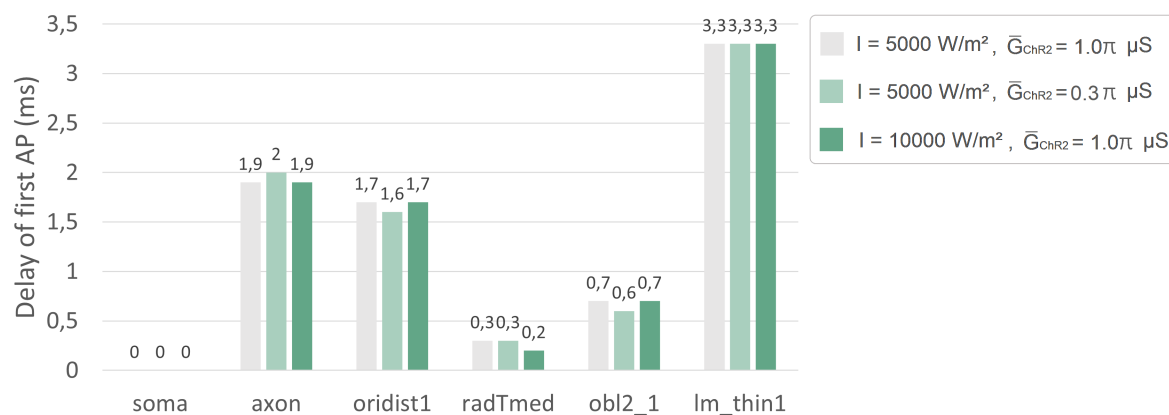


Figure 4.6: Delay between an AP measured in the indicated section and in the soma. The opsin is located in the same section with a maximal conductance of $1.0\pi \mu\text{S}$, $0.3\pi \mu\text{S}$, and $1.0\pi \mu\text{S}$ for the grey, light green, and dark green bars, respectively. The respective optogenetic intensities are 5000 W/m^2 , 5000 W/m^2 , and 10000 W/m^2 . The optogenetic pulse is continuous with a pulse duration of 500 ms.

Normally, EPSP from different synapse inputs are integrated at the soma and can result in an action potential. It is also possible that the action potential was actually initiated in the dendrite, which is called a dendritic action potential. In order to investigate the AP initiation, recordings of the membrane potential at the soma and stimulation location are simultaneously made. The time of the first AP in the soma and stimulation location are compared and the delay is calculated. Figure 4.6 shows the result for all stimulation locations of the diffuse neuronal stimulation. The delay is calculated for the first action potential because for some stimulation locations, only one AP was measured in total. Optogenetic pulse intensities of 5000 W/m^2 and 10000 W/m^2 were used, combined with a maximal conductance of $0.3\pi \mu\text{S}$ and $1.0\pi \mu\text{S}$, leading to three cases. The pulse intensity and maximal conductance have limited impact on the delay. The delays measured between the soma and itself are obviously zero. All delays are positive, leading to the conclusion that the action potential is initiated at the stimulation location. Arrangement of the sections from low to high delays gives: radTmed, obl2_1, oridist1, axon, and lm_thin1. The observations are expandable to almost all observed action potentials. The spiking pattern measured at the soma resembles the spiking pattern measured at the stimulation location, with a slight delay due to the propagation of the action potential. If the simulation location is distinct from the soma and axon, we can say that the

measured spikes are dendritic spikes.

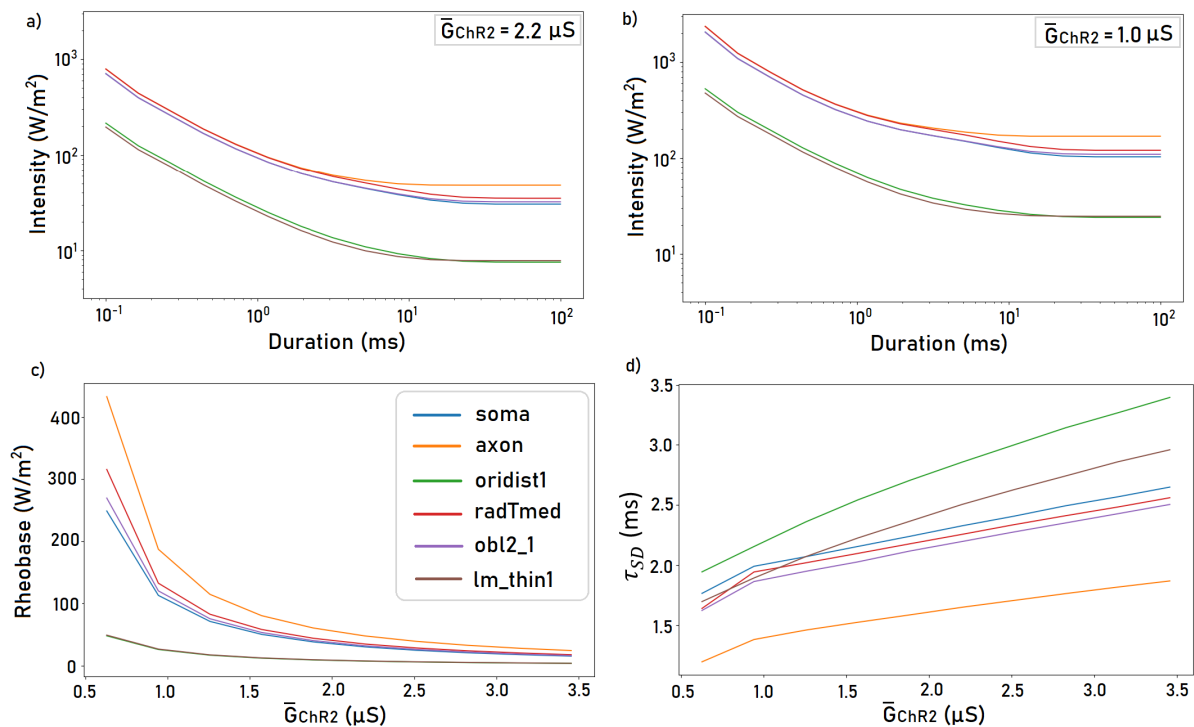


Figure 4.7: (a),(b) Strength-duration curve for different ChR2(H134R) locations and a maximal conductance of respectively $0.7\pi \mu\text{S} = 2.2 \mu\text{S}$ and $1.0 \mu\text{S}$, recorded in the soma. The optogenetic pulse duration (ms) of a continuous pulse is shown on the x-axis and the optical pulse intensity (W/m^2) on the y-axis. Plot (c) represents the rheobase (W/m^2) calculated for the different opsin locations in function of the maximal conductance (μS). The strength-duration time constant (ms) in function of the maximal conductance (μS) is visualised in the plot (d).

Figure 4.7 shows the results for the strength-duration plots and its relevant parameters. The strength-duration curve is plotted in (a) and (b) for two values of maximal ChR2(H134R) conductance, i.e. $2.2 \mu\text{S}$ and $1.0 \mu\text{S}$, respectively. The recordings were done in the soma for all stimulation locations. For both maximal conductances, similar relative differences are observed between the different stimulation locations. Due to the lower maximal conductance used in plot b), a higher intensity is needed for all pulse durations to generate an action potential. This results in an upward shift of all curves compared to plot a). The strength-duration curves of oridist1 and lm_thin1 are shifted downward compared to the other curves. Both their rheobase and strength-duration time constants are comparable. Their curves intersect for a pulse duration of 19.54 ms in plot a) and 20.67 ms in plot b). Lm_thin1 is more excitable for smaller pulse durations, oridist1 for larger pulse durations. The other four sections have comparable strength-duration time constants but their rheobase differ. The highest rheobase and lowest strength-duration time constant is observed when the opsin is located in the axon. The rheobase of the soma, obl2.1, and radTmed are almost equal, with a slightly higher value for the latter. The rheobase and strength-duration time constants for $\bar{G}_{\text{ChR2}} = 2.2 \mu\text{S}$ can be found in Table 4.3. The strength-duration curves are calculated for only two values of maximal conductances. To see the influence of \bar{G}_{ChR2} on the strength-duration curves, the rheobase (c) and strength-duration time constant (d) are plotted for a set of maximal conductance, i.e. $[0.2\pi, 0.3\pi, \dots, 1.1\pi] \mu\text{S}$. An increasing maximal conductance results in a decreasing rheobase and an increasing strength-duration time constant for all locations. The difference in rheobase is the most pronounced for small values of \bar{G}_{ChR2} . Lm.thin1 and oridist1 have an equal rheobase for all values of \bar{G}_{ChR2} .

However, τ_{SD} is higher when the opsin is located in oridist1. The axon distinguishes oneself from the other locations with a higher rheobase and smaller strength-duration time constant over the whole line. Placement of the opsin in the soma, radTmed, and obl2_1 gives very similar values for both parameters. The strength-duration time constant curves intersect for small maximal conductances (plot d)). The order of strength-duration time constant magnitude of the different locations is changed for $\bar{G}_{ChR2} = 1.0 \mu S$ and $\bar{G}_{ChR2} = 2.2 \mu S$, however oridist1 and lm_thin1 remain the only two locations for which the curves intersect.

CP15TK21		
Section	I_{RH} (W/m ²)	τ_{SD} (ms)
soma	30.47	2.327
axon	48.06	1.650
oridist1	7.555	2.856
radTmed	35.06	2.256
obl2_1	32.19	2.197
lm_thin1	7.836	2.504

Table 4.3: The rheobase intensity (I_{RH}) and strength-duration time constant (τ_{SD}) of the strength duration curve in Figure 4.7(a). A maximal conductance of $2.2 \mu S$ is used.

The measured input impedances are shown in Figure 4.8. The highest input impedance is measured in the soma, for all frequencies. It has a mean of $158.1 M\Omega$. Lowest input impedances are measured in the axon and obl2_1. They intersect at a frequency of $3.37 Hz$ for an input impedance of $44.33 M\Omega$. Obl2_1 has the highest input impedance of the two for low frequencies. The mean input impedances of the other three sections, i.e. lm_thin1, oridist1, and radTmed, are respectively $55.75 M\Omega$, $78.25 M\Omega$, and $117.4 M\Omega$.

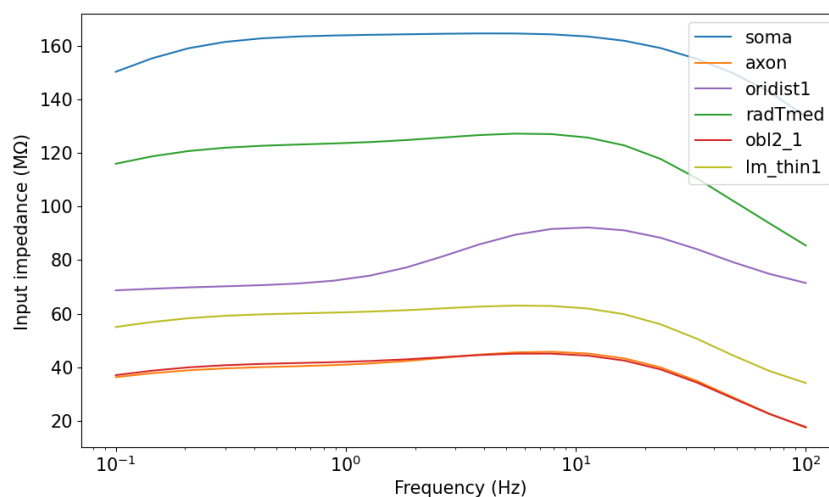


Figure 4.8: Input impedance measured at the indicated location in function of the frequency of the oscillatory current stimulus. It is measured 200 ms after the onset of the stimulus. The CP15TK21 neuron model was used.

Symmetric diffuse neuronal stimulation

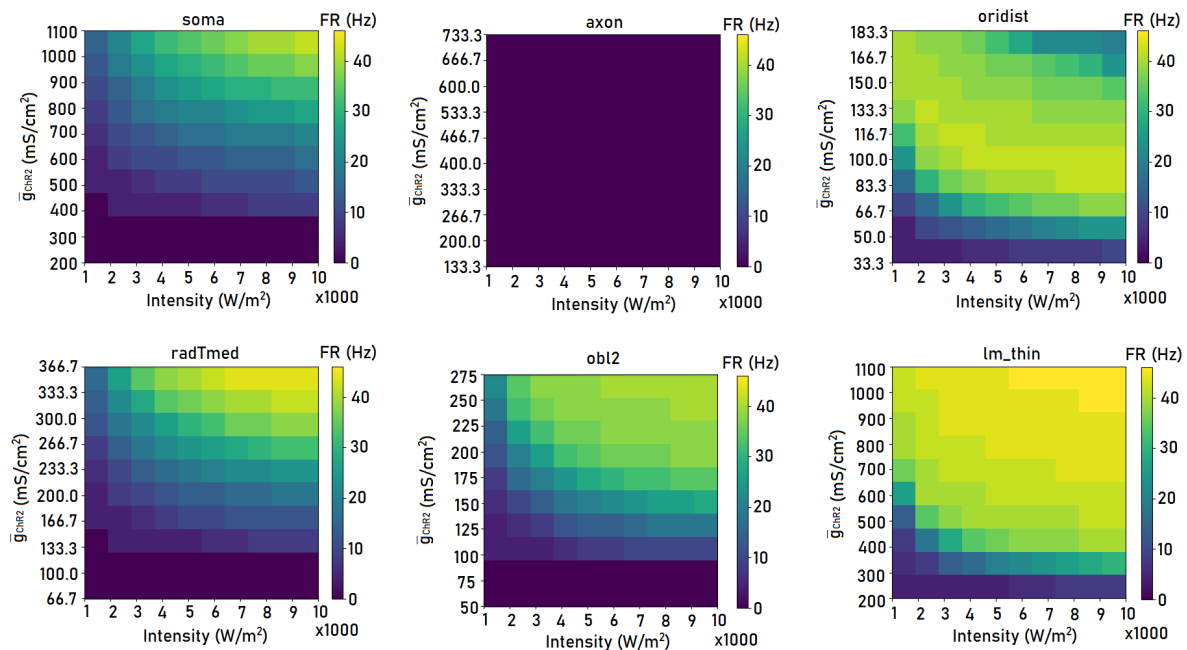


Figure 4.9: 2D colorplots of the mean firing rate, calculated according to Eq. 4.30, in function of the optogenetic pulse intensity and maximal specific conductance of ChR2(H134R). A continuous pulse of 500 ms is used. The mean firing rates are recorded in the soma for each stimulation location of the symmetric diffuse stimulation strategy, indicated in the title of the surface plots. Oridist refers to the two symmetrical sections: oridist1 and oridist2. Similarly, obl2 refers to obl2_1 and obl2_2 and lm_thin to lm_thin1 and lm_thin2.

Compared to the diffuse neuronal stimulation strategy, the opsin is now placed in both symmetrical sections. For example, oridist1 and oridist2 are both targeted instead of only oridist1. The surface area of two sections is obviously larger so the maximal specific conductance is decreased to maintain an equal maximal conductance. The opsin is still uniformly distributed along the targeted sections and the pulse duration is 500ms. In Figure 4.9, the plots for the soma, axon, and radTmed remain unchanged but these plots are added for comparison. When the opsin is placed in both oridist1 and oridist2 (indicated with 'oridist'), the mean firing rate does not become zero anymore for a higher maximal conductance. Primarily, FR increases for increasing intensity and maximal conductance. However, for large values (right upper corner), there is a decrease in FR. Figure 4.10 (a) and (b) illustrate the difference between the single case and symmetric case. For lower values of I and \bar{G}_{ChR2} , continuous firing is observed with a high rate when the opsin is only located in oridist1. Targeting both sections results in an initial burst, followed by tonic firing with a lower firing rate as the single case. As was seen in the previous part, the firing rate becomes zero for a higher intensity and maximal conductance. This is not observed when both sections are targeted. Contrary, the firing rate increases and the spikes are regularly spaced. The three lower plots of Figure 4.9 show the activity in the soma when the opsin is placed in apical dendrites. Again, an overall higher FR is observed for lm_thin as for obl2, which is remarkable because of the longer distance from the soma. Placing the opsin in obl2_1 and obl2_2 (indicated with 'obl2') clearly increases the mean firing rate in the soma, compared to the single case (Figure 4.4). The firing rate in obl2_1 itself is also increased, as expected. This can be seen in Figure 4.10 (d). The period of silence observed in the single case is not present anymore when both sections are targeted. The same is observed for lm_thin1 and lm_thin2 (indicated with 'lm_thin'). The mean firing rate at the soma even surpasses the FR measured with

radTmed as opsin location. This indicates an interaction between both symmetrical sections.

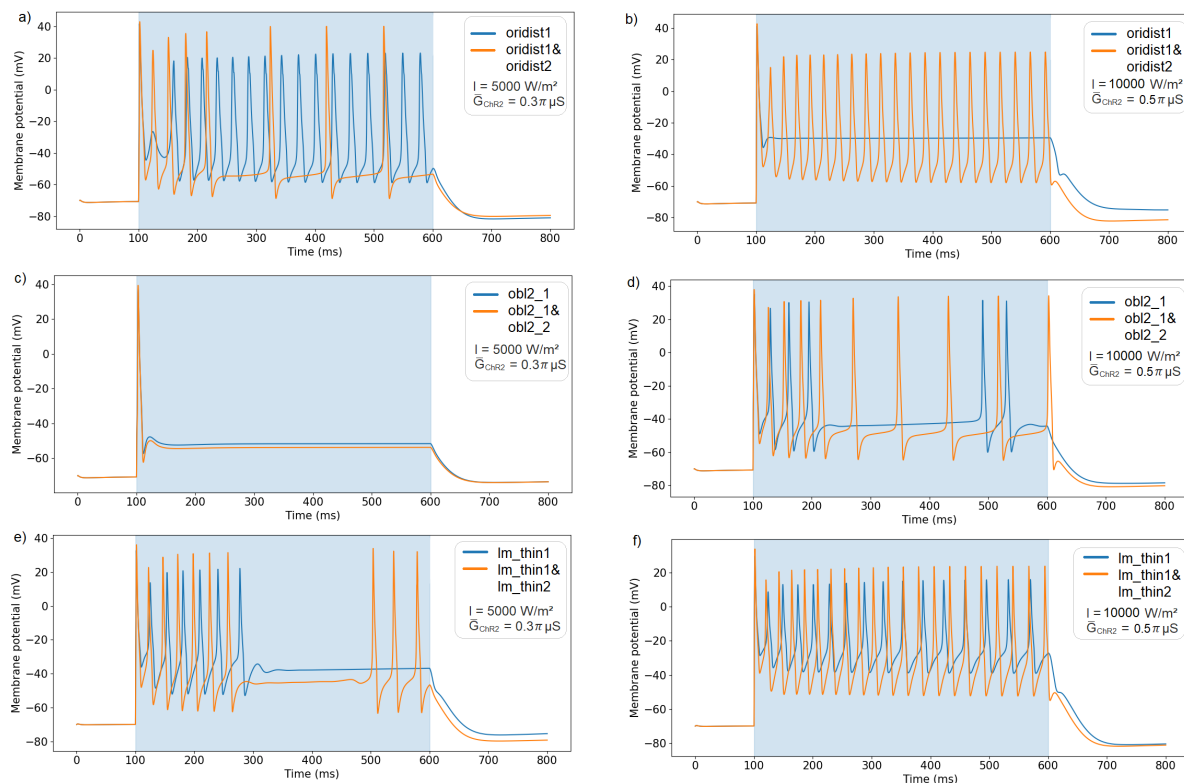


Figure 4.10: The membrane potential (mV) in function of time (ms) with the opsin located in a single section (blue) and in the two corresponding symmetric sections (orange). In both cases, the membrane potential was measured in the section with suffix 1. A continuous optogenetic pulse of 500 ms and 5000 W/m^2 , and a maximal conductance of $0.3\pi \mu\text{S}$ was used in a), c), and e). For plot b), d), and f), an intensity of 10000 W/m^2 and a maximal conductance of $0.5\pi \mu\text{S}$ was used. The optogenetic pulse is indicated with the blue area.

Basal dendritic stimulation

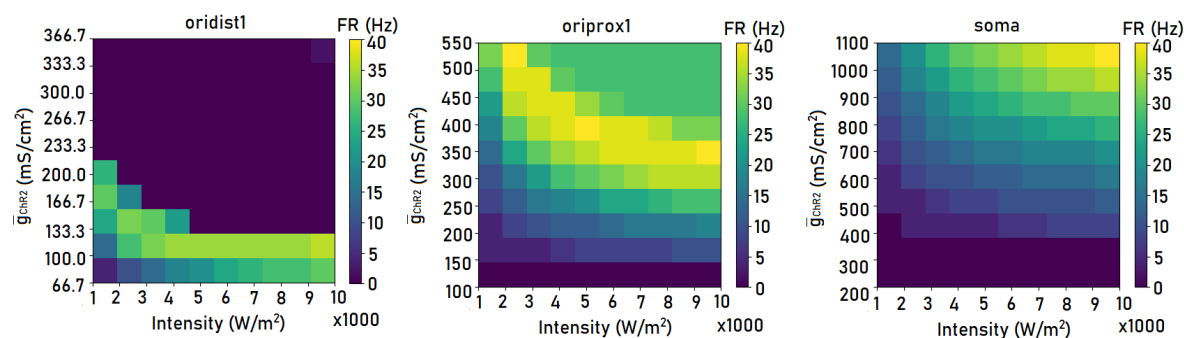


Figure 4.11: 2D colorplots of the mean firing rate, calculated according to Eq. 4.30, in function of the optogenetic pulse intensity and maximal specific conductance of ChR2(H134R). A continuous pulse of 500 ms is used. The mean firing rates are recorded in the soma. From left to right, the opsin is located in oridist1, oriprox1, and the soma.

The last strategy consecutively targets different parts of the same basal dendrite. Oridist1 represents the distal part, with a distance of $205 \mu\text{m}$ between its center and the soma. Oriprox1, the proximal part, is connected to the soma with a distance of $55 \mu\text{m}$ between the soma and its

center. Oridist1 has a total surface area of $300\pi \mu\text{m}^2$ and oriprox1 of $200\pi \mu\text{m}^2$. The maximal specific conductance is again scaled, which can be seen on the y-axis of the plots in Figure 4.11. The soma has a surface area of $100\pi \mu\text{m}^2$ so the maximal specific conductance is respectively divided by three and two for oridist1 and oriprox1. It was expected that an optogenetic stimulus of the same intensity would elicit a comparable response in the soma for the opsin located in the distal and proximal part of the same dendrite. Figure 4.11 and 4.12 show that this is not the case. Placement of the opsin in oridist1 gives higher mean firing rates for small values of \bar{g}_{ChR2} . Only three spikes are measured in oriprox1 for the same stimulus and maximal conductance when the opsin is located in oriprox1 (Figure 4.12 (a)) and only one for the soma. Increasing values of the intensity and maximal conductance results in a mean firing rate of zero for oridist1, as was already seen in the previous parts. In oriprox1, the mean firing rate increases whereafter it reaches a constant value of 28 Hz.

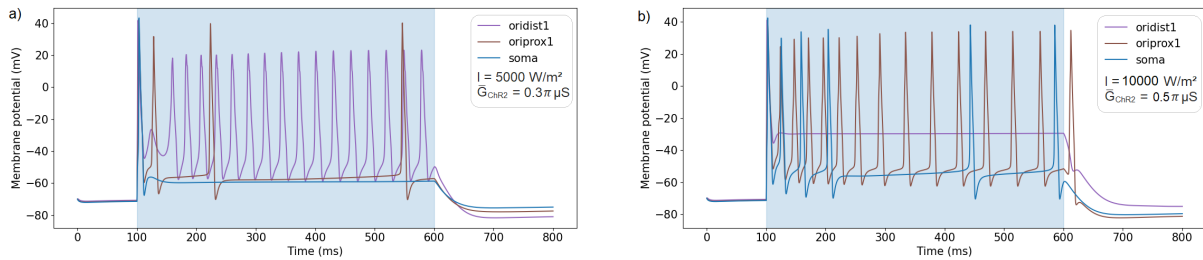


Figure 4.12: The membrane potential (mV) in function of time (ms) with the opsin location indicated in the legend. The membrane potential is measured in the same section. A continuous optogenetic pulse of 500 ms and 5000 W/m^2 , and a maximal conductance of $0.3\pi \mu\text{S}$ was used in a). For plot b), an intensity of 10000 W/m^2 and a maximal conductance of $0.5\pi \mu\text{S}$ was used. The optogenetic pulse is indicated with the blue area.

The input impedances are also measured for the distal and proximal basal dendritic section (Figure 4.13). It can be seen that the input impedance of oridist1 is higher than that of oriprox1 for all frequencies. The mean input impedances of oridist1 and oriprox1 are respectively $117.4 \text{ M}\Omega$ and $52.00 \text{ M}\Omega$. In both cases, an increasing frequency results in a slight increase of the input impedance until 5.5 Hz, followed by a decreasing in input impedance.

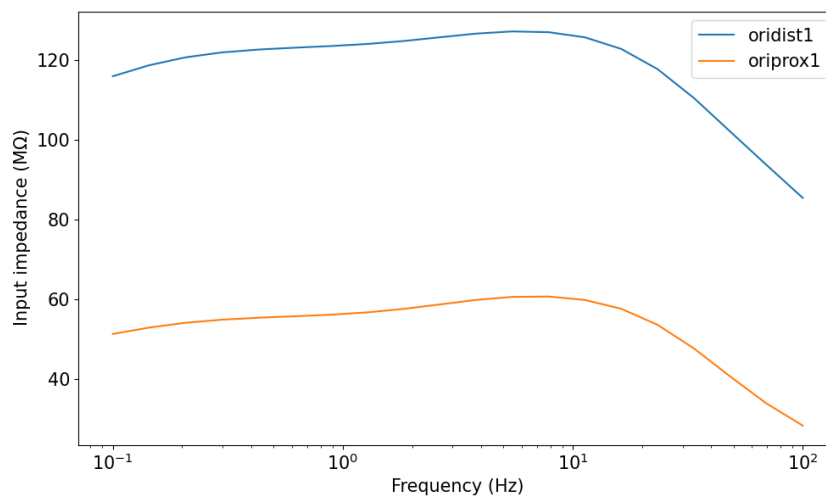


Figure 4.13: Input impedance measured at a distal (oridist1) and proximal (oriprox1) basal dendritic section in function of the frequency of the oscillatory current stimulus. It is measured 200 ms after the onset of the stimulus. The CP15TK21 neuronal model is used.

4.5 Discussion

The response of the neuron on optogenetic stimuli with different opsin locations has been characterized by different features. The mean firing rate has learned us how stimulation of a distal dendritic tuft section (`lm_thin1`) leads to a higher mean firing rate compared to the other locations, almost independent of the optogenetic pulse intensity and maximal specific conductance of the opsin channel. A possible explanation could be that the surface of this section is smaller and thereby the maximal specific conductance is higher, leading to a more spatially clustered stimulation. However, simultaneously targeting two dendritic tuft sections (`lm_thin1` and `lm_thin2`) led to a total surface area equal to that of the soma. In this case, an equal maximal specific ChR2(H134R) conductance was used and yet, higher firing rates are observed. To gain insight in this distinct behavior, it is important to repeat that the spikes are generated at the stimulation location, a dendritic tuft dendrite in this case. Normally, multiple EPSP travel towards the soma and if the integration is high enough, an action potential is initiated at the soma. In case of a dendritic spike, the action potential is already initiated at the dendrite and propagates along the neuron towards the soma. Jarsky et al. (2005) studied the dendritic spike propagation following a distal synaptic activation of hippocampal CA1 pyramidal neurons. Some of the findings in this study are possibly an explanation to the observations made in this dissertation. They mainly focused on the following two excitatory synaptic inputs: the perforant-path input, which is an input to the apical dendritic tuft, and the Schaffer collaterals, an input to basal and apical dendrites. The study was performed by a combination of a computational and experimental approach. As neuronal model they used a strong and weak dendritic excitability model. Computational simulation led to three main conclusions:

1. Apical dendritic tuft inputs, have a limited ability to trigger somatic action potentials in CA1 neurons. The reason is that EPSP are attenuated during their propagation to the soma.
2. If apical dendritic tuft inputs result in dendritic spikes, it is possible to trigger somatic action potentials. This means that the initiation of local dendritic spikes can circumvent the problem of attenuation along the long distances between the soma and the apical dendritic tuft. Applied to this dissertation, optogenetic stimulation of the apical dendritic tuft is expected to have little to no influence on the somatic spiking behavior if no dendritic spikes were initiated.
3. An additional apical dendritic input (closer to the soma than the apical dendritic tuft) can facilitate the propagation of the dendritic spike that was initiated in the apical dendritic tuft.

These three conclusion were confirmed by experimental results. Remarkably, Jarsky et al. (2005) observed that in models with strongly excitable dendrites, the apical dendritic tuft input (perforant-path input) is more efficacious than upper apical dendritic inputs (Schaffer-collateral input), in that a lower number of inputs are necessary to trigger a spike. This is also observed in our results by the fact that a higher mean firing rate is measured in the soma when the opsin is located in the apical dendritic tuft (`lm_thin1`). If the opsin is located elsewhere, a lower mean firing rate is measured even though an equal optogenetic stimulus was used. According to Jarsky et al. (2005), this can be explained by the high input impedance of the small-diameter tuft branches. For a high input impedance, an injected current will result in a high change in potential. The input impedances were therefore determined for the different stimulation locations (Figure 4.8). Contradictory, the soma has the highest input impedance, followed by `radTmed`, which has the highest diameter of the used sections. So, no correlation is seen between the input impedance and the diameter of the sections. Therefore, other factors will play a role in the elevated activity for apical tuft dendritic stimulation. Next, Jarsky et al. (2005) experimen-

tally observed that the action potential threshold in the soma was lower when somatic spikes were triggered by dendritic spikes initiated in the apical tuft compared to the action potential threshold when somatic spikes were directly evoked by a current injection in the soma. This would explain why even optogenetic stimulation of the soma results in a lower firing rate in the soma itself than optogenetic stimulation of the dendritic tuft section. In order to link the findings of Jarsky et al. (2005) to our results, three major differences are discussed. First, the biophysics of the models used by Jarsky et al. (2005) are less complex than those of CP15TK21. However, they tested the robustness of the predictions by repeating their tests with a more complex model and found that the observations remained unchanged even though longer dendrites and more voltage-dependent currents were included in the model. Another major difference is their type of input, which is synaptic instead of an optogenetic stimulus. The mechanism by which a dendritic spike is initiated is therefore different but it is expected that the propagation of the dendritic spike and the impact on the somatic spiking pattern are equal. And lastly, the observations of Jarsky et al. (2005) that resemble ours, are mainly seen for strong dendritic excitability models. In weak excitable models there is an unreliable propagation meaning that not all dendritic spikes will reach the soma (Jarsky et al., 2005). Our model is assumed to be classified as a strong dendritic excitability model because almost all measured dendritic spikes could propagate to the soma and trigger a somatic spike. Tomko et al. (2021) also describes how M18, of which the biophysics are adopted for CP15TK21, is a strongly-propagating model based on the weak attenuation of back-propagating action potentials. According to Sáray et al. (2021), the attenuation of bAPs is a measure for dendritic excitability so this affirms our assumption. For these reasons, it is assumed that the location dependent propagation characteristics of the dendritic spikes observed in both our studies can be related.

Next to the increased firing rates observed for apical dendritic tuft stimulation, also other observations were made. Normally, increasing the stimulation intensities or maximal opsin conductances lead to higher firing rates. When the opsin is located in the axon or the distal basal dendrite (*oridist1*), the firing rate becomes zero, while the membrane potential is at a constant depolarized level (see Figures 4.4 and 4.5). This phenomenon is described as a depolarization block. According to Tomko et al. (2021), a large amount of (optogenetic) current injection will partially block the deinactivation of the sodium channel. The depolarization block is then observed if delayed the rectifier potassium current does not activate enough to repolarize the neuron.

Targeting of the soma, the apical trunk dendrite (*radTmed*) and the radial oblique dendrite (*obl2_1*) results in an equal spiking pattern (see Figure 4.5 (b) and (c)). The optogenetic pulse is characterized by an initial peak current. This is reflected in the initial burst seen in the spiking pattern for the different sections. Thereafter, the neuron adjusts until a steady-state is reached. If the steady-state optogenetic current is sufficient, a continuous firing is observed. The higher the pulse intensity and conductance of the opsin channel, the more current injection and the shorter the period of silence in between the initial burst and the steady-state continuous firing. The firing rate increases. Figure 4.5 (c) illustrates one of the characteristics of dendritic spikes: a more depolarized action potential voltage threshold compared to the soma (Gasparini, 2004).

Strength-duration curves reveal information about the excitability of a stimulation location. Optogenetic stimulation of a distal basal dendrite (*oridist1*) or apical dendritic tuft dendrite (*lm_thin1*) result in rheobases that are on average 79% lower than those obtained for an optogenetic stimulation of the other sections. These two sections are therefore more excitable and will trigger a somatic AP already for lower pulse intensities. A possible explanation is again the high input impedances because of the small-diameters of both branches. *Lm_thin1* and *oridist1* have respective diameters of 1 μm and 1.5 μm , which are for this model the smallest of all sections. *Lm_thin1* is slightly more excitable for pulse durations smaller than 20 ms. For all sections applies that a higher maximal conductance decreases the rheobase because a

higher maximal conductance means that for the same optogenetic pulse intensity, more current is injected into the section. An AP will thus be evoked for lower optogenetic intensities. The increasing strength-duration time constant is slightly more complex to understand. In Eq. 4.35 $PD[0]$, the shortest pulse duration, remains unchanged. I_{RH} and $I[0]$, the intensity corresponding with the smallest pulse duration, will both decrease so an increasing strength-duration time constant learns us that the rheobase decreases slower than $I[0]$. So a higher ChR2(H134R) maximal conductance will have more impact on the pulse intensity necessary to generate an AP for small pulse duration than for long pulse durations. This applies again to all sections.

In order to get closer to the realistic situation in which the opsin is not only expressed on one dendrite, but rather on all 'equivalent' dendrites, the symmetrical section were added. The depolarization block that was observed when a single basal dendrite (oridist1) was targeted has changed to a continuous firing in the case of two basal dendritic sections (oridist1 and oridist2). In all cases, the maximal conductance was kept constant, meaning that the larger area of two sections led to a smaller maximal specific conductance. In other words, the optogenetic input is more spatially spread. Therefore the depolarization block did not occur in the symmetric case. The fact that a depolarization block is faster observed in this section indicates a higher excitability. For all cases, the simultaneous stimulation of two symmetric sections leads to dendritic spikes in both sections that strengthen each other, leading to a higher amplitude and firing rate.

The effects of the thin branches in the apical tuft leading to more dendritic spikes and therefore to a more efficacious optogenetic stimulation also seem to take place in the basal dendrites. First, the distal part of a basal dendrite was stimulated. This section has a smaller diameter but a higher surface area than the proximal part so the maximal specific conductance that was used was lower than that in the proximal basal dendrite. Yet, higher firing rates are observed, eventually even leading to a depolarization block. Again, the observed spikes are dendritic spikes, initiated at the stimulation location. Figure 4.13 illustrated that the distal section has a higher input impedance for all frequencies between 0.1 and 100 Hz. This is different from the results measured for the stimulation locations of the diffuse neuronal stimulation strategy (Figure 4.8), explained in Section 4.3.1, where the sections where stimulation led to the highest firing rates, measured in the soma, were not necessarily the sections with the highest input impedance. However, this increased input impedance will play a role in the increased higher mean firing rates measured upon stimulation of the distal basal dendrite.

Chapter 5

Morphologically simple versus complex neuronal model

The results obtained by in silico modeling should always be treated with caution. Neuron and opsin models are made as realistic as possible. Yet, they are made for a specific study or tuned ad hoc for a limited set of experiments. In the choice and interpretation of the neuron model, it is important to emphasize that there is more than one possible realistic solution (Tomko et al., 2021). For that reason, a more complex, full-morphology model is adopted. The morphology is different from CP15TK21 but the biophysics remain. More details can be found in Section 5.1. The opsin model and main methodology of Chapter 4 are preserved. Localized targeting of the opsin on specific locations becomes more difficult in an extended model. Section 5.2.1 elaborates on the stimulation strategies. The results are compared and discussed in Section 5.3 and 5.4.

5.1 Migliore 2018: M18

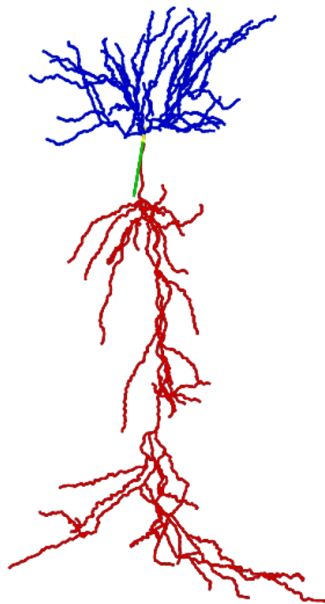


Figure 5.1: CA1 pyramidal neuron morphology of the M18 model. The soma is the central yellow point, the axon is represented in green, the basal dendrites in blue, and the apical dendrites in red (Migliore et al., 2018).

A second, more complex model was used to study the effects of the complexity of the neuron model on the results: the model of Migliore et al. (2018) (M18). This model can be found on modelDB under accession number 244688. Instead of 19 sections, this model has 165 sections. It was the result of a study that analyzed the peak specific conductance of ion channels in individual CA1 neurons (Migliore et al., 2018). Morphologically, this model is much more accurate than the reduced-morphology model. However, the computational time increases with complexity. The biophysics of M18 and CP15TK21 are similar and are explained in Section 4.1.

The question now arises if it is necessary to model the neuron with such high complexity. Tomko et al. (2021) used HippoUnit to evaluate the capabilities of a model. It is a toolbox used to compare simulation results from one neuronal model to another, specially made for CA1 pyramidal neurons. The CP15TK21 model (named as CP15 vTo21 in the paper of Tomko et al. (2021)) showed lower final error scores on almost all HippoUnit tests than the M18 model, meaning that it is actually better in reproducing the characteristic properties of a CA1 pyramidal neuron (Tomko et al., 2021). Therefore, the full-morphology model of Migliore et al. (2018) should be treated as a distinct model instead of a more accurate model.

5.2 Methodology

The model of Migliore et al. (2018) is implemented in the NEURON simulation platform. The same versions are used as for CP15TK21 (NEURON 8.0.0 and Python 3.7.11). The double two-state opsin model of Schoeters et al. (2021) is again used to model ChR2(H134R) and inserted into M18. The models are solved by the default Backward Euler method with a maximum time step of 0.025 ms. Similar initial conditions are used: an initial closed, dark adapted state ($R=1$, $O=0$) of ChR2(H134R), an initial membrane voltage of -70 mV, and a temperature of 6.3 °C. The main goal of changing the CA1 pyramidal neuron model is to study the impact of the complexity of the model on the results concerning the location-dependent excitation of optogenetic stimulation. For this model, it is not useful to look at separate sections as was done for the CP15TK21 model since there are 165 sections. Instead of a uniform distribution along a section, the opsin is normally distributed around a central location. These locations are chosen such that they resemble those used in the CP15TK21 stimulation strategies. Features used for the evaluation of these stimulation locations are similar to those used in Chapter 4. Definitions and explanations of the features can be found in Section 4.3.

5.2.1 Stimulation strategies

Section	Reference point	M18		CP15TK21		
		μ (μm)	σ (μm)	Reference Point(s)	μ (μm)	σ (μm)
soma	soma	0	25	soma	0	25
axon	axon	0	75	axon	0	125
oridist	soma	285.00	75	oridist	0	100
radTmed	soma	188.33	25	radTmed	0	50
obl2	soma	288.33	25	obl2	0	75
lm_thin	soma	630.00	25	lm_thin	0	100

Table 5.1: The mean (μ) and standard deviation (σ) used for the normal distribution of the maximal specific conductance of ChR2(H134R) in M18 and CP15TK21, corresponding with the stimulation locations, in function of the distance to the reference point.

In order to compare location dependent effects on two different neuronal models, a methodology was found for the insertion of the opsin. The aim is to stimulate similar locations on different neuronal models. M18 consists of 165 sections, so uniformly targeting a specific section, like in the stimulation strategies in Chapter 4, was not optional. Instead, the opsin channel is inserted in every segment of the neuron. The presence of the opsin can be controlled by adapting the maximal specific conductance. A conductance of zero is similar to not inserting the opsin. The higher the conductance, the more current that is injected for the same illumination intensity. The maximal specific conductance can therefore be treated as the density of ChR2(H134R). The maximal specific conductance follows a normal distribution in function of the distance to a reference point. The general form of a Gaussian probability density function is given by:

$$\bar{g}_{ChR2}(x) = \bar{g}_{ChR2,max} \cdot e^{-\frac{1}{2}\left(\frac{x-\mu}{\sigma}\right)^2} \quad (5.1)$$

with x the path distance between the segment for which \bar{g}_{ChR2} is determined and the reference point, not the distance between the vectors. For reasons elaborated on later, the soma is the reference point for all stimulation location except of the axon. There are two parameters: the mean (μ) and the standard deviation (σ). The mean of the distribution is the distance to the reference point where $\bar{g}_{ChR2}(\mu) = \bar{g}_{ChR2,max}$. To target similar locations as in CP15TK21, the distances to the soma of the stimulation locations of CP15TK21 are determined and used as mean values for the corresponding stimulation locations of M18 (except of the axon). The most outer part of a section is used to calculate the distance. They can be found in Table 5.1. In the preceding analysis, an equal maximal conductance was maintained for all locations. The maximal conductance was determined by multiplying the maximal specific conductance by the surface area of the targeted section. The fact that it is not uniformly distributed anymore, makes it more complex to compute the total maximal conductance. If $\bar{g}_{ChR2,max} = 1$, then the maximal conductance is equal to:

$$\bar{G}_{ChR2} = \sum_{sec} \sum_{seg} e^{-\frac{1}{2}\left(\frac{x-\mu}{\sigma}\right)^2} \cdot \frac{A_{sec}}{n_{seg}} \quad (5.2)$$

Where the sum is evaluated for all segments of the 165 sections and x is the distance between the segment and the reference point. A_{sec} is the surface area of the section and n_{seg} the number of segments in that section. To obtain a desired maximal conductance ($\bar{G}_{ChR2,desired}$), $\bar{g}_{ChR2,max}$ has to be equal to:

$$\bar{g}_{ChR2,max} = \frac{\bar{G}_{ChR2,desired}}{\sum_{sec} \sum_{seg} e^{-\frac{1}{2}\left(\frac{x-\mu}{\sigma}\right)^2} \cdot \frac{A_{sec}}{n_{seg}}} \quad (5.3)$$

The axon is a special case, because it is one specific part of the neuron. Applying the same methodology as for the other sections results in a high \bar{g}_{ChR2} in all basal and apical sections at the same distance from the soma as the axon, which is not desired. To solve this, the axon itself is used as reference point and μ is set to zero. So, x is now the distance between the segment in question and the axon. The standard deviation is a measure for the spread of \bar{g}_{ChR2} . Small values of σ result in high maximal specific conductance for all segments on a distance μ from the reference point and a fast decay for an increasing distance. Table 5.1 lists the chosen standard deviation for every stimulation location. The axon and oridist have larger standard deviations. The reason is that there are less sections at a distance μ from the reference point for these two cases. Because of the requirement of equal maximal conductance, $\bar{g}_{ChR2,max}$ will reach up to very high values. In order to have values in the same order of magnitude, a higher

standard deviation was chosen. Figure 5.2 shows the maximal specific conductance distribution for every stimulation location for $\bar{G}_{\text{ChR2,desired}} = 0.7\pi \mu\text{S}$. With the chosen standard deviations, \bar{g}_{ChR2} ranges between 0 and ± 200 . In the following, the same names as used for the stimulation locations of CP15TK21 will be designated to the corresponding stimulation locations of M18, as was also done in Figure 5.2.

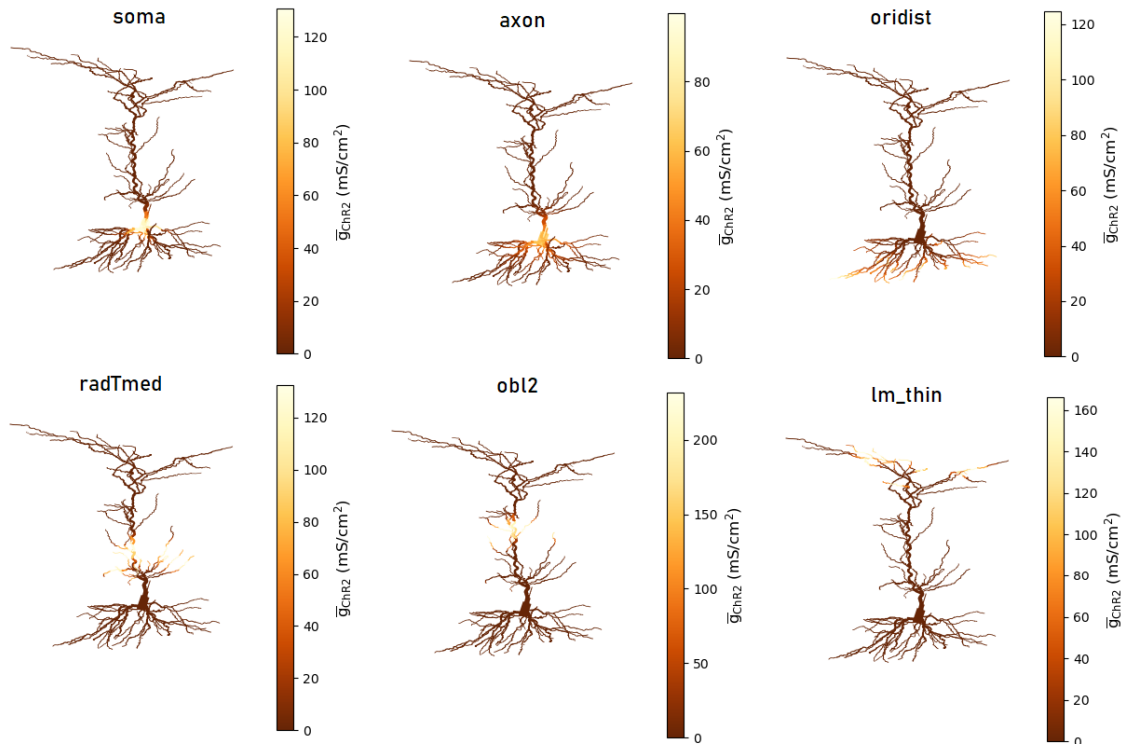


Figure 5.2: Distribution of the maximal specific conductance for the different stimulation locations of M18 for a maximal conductance of $0.7\pi \mu\text{S}$. The names are derived from the corresponding stimulation locations of CP15TK21. Maximal specific conductance follows a normal distribution with parameters μ, σ , given in Table 5.1, and $\bar{g}_{\text{ChR2,max}}$ determined according to Eq. 5.3.

Important to note is the fact that both the apical and basal dendrites at a distance μ get high \bar{g}_{ChR2} values. Therefore, a maximal specific conductance value is only assigned to the basal dendrites in case of 'oridist' and to the apical dendrites in case of 'radTmed', 'obl2', and 'lm_thin'. The sum over the section (sec) in Eq. 5.3 and 5.2 is limited to the same sections. In some cases, the membrane potential is measured at the stimulation location instead of the soma because the injected optogenetic current is voltage dependent. For that reason, it is educational to know the membrane voltage at the location of the opsin. However, the opsin is now inserted in multiple sections. Sections with similar distances to the soma as the sections of CP15TK21 were found to perform the recordings. They are summarized in Table A.3 in Appendix A.

The transition to a normally distributed maximal specific conductance is also made for CP15TK21 in order to have a distribution that resembles the one of M18 to make the comparison. The number of segments are increased by a factor three for every section to have a higher spatial resolution. The same methodology as was used for the axon, is now used for all stimulation locations, i.e. the section itself as reference point and a mean of zero. The independent variable of the distribution, x , is the distance between the section itself and the segment for which the maximal specific conductance is determined. The standard deviations are again adapted for every case in order to have similar \bar{g}_{ChR2} ranges. The values can be found in Table 5.1.

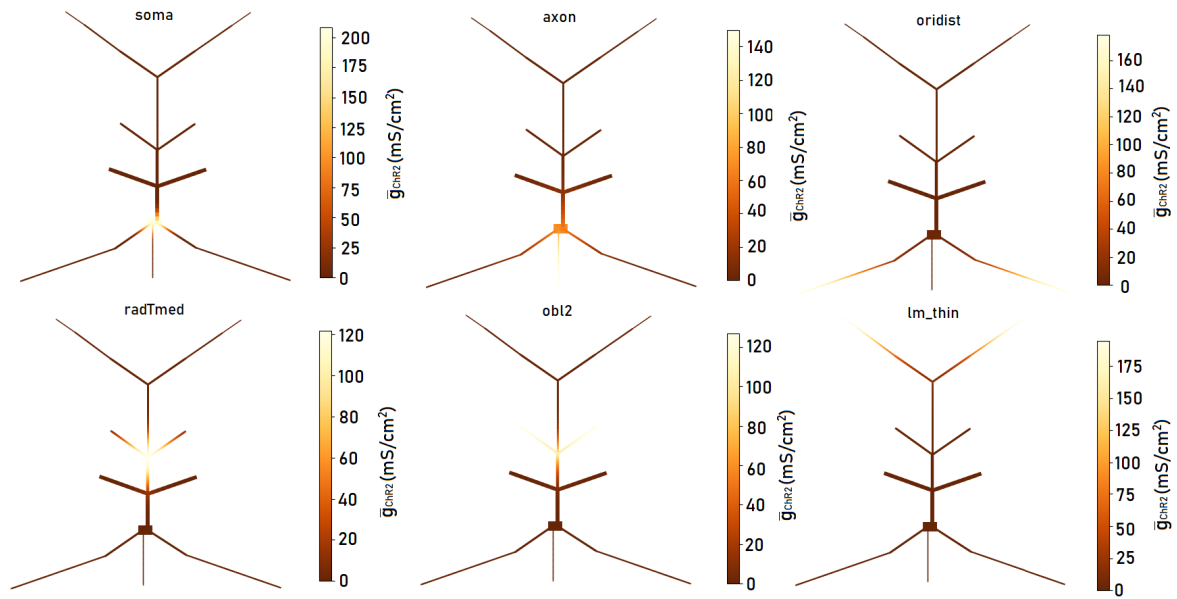


Figure 5.3: Distribution of the maximal specific conductance for the different stimulation locations of CP15TK21 for a maximal conductance of $0.7\pi \mu\text{S}$. Maximal specific conductance follows a normal distribution with parameters μ, σ , given in Table 5.1, and $\bar{g}_{\text{ChR2,max}}$ determined according to Eq. 5.3.

5.3 Results

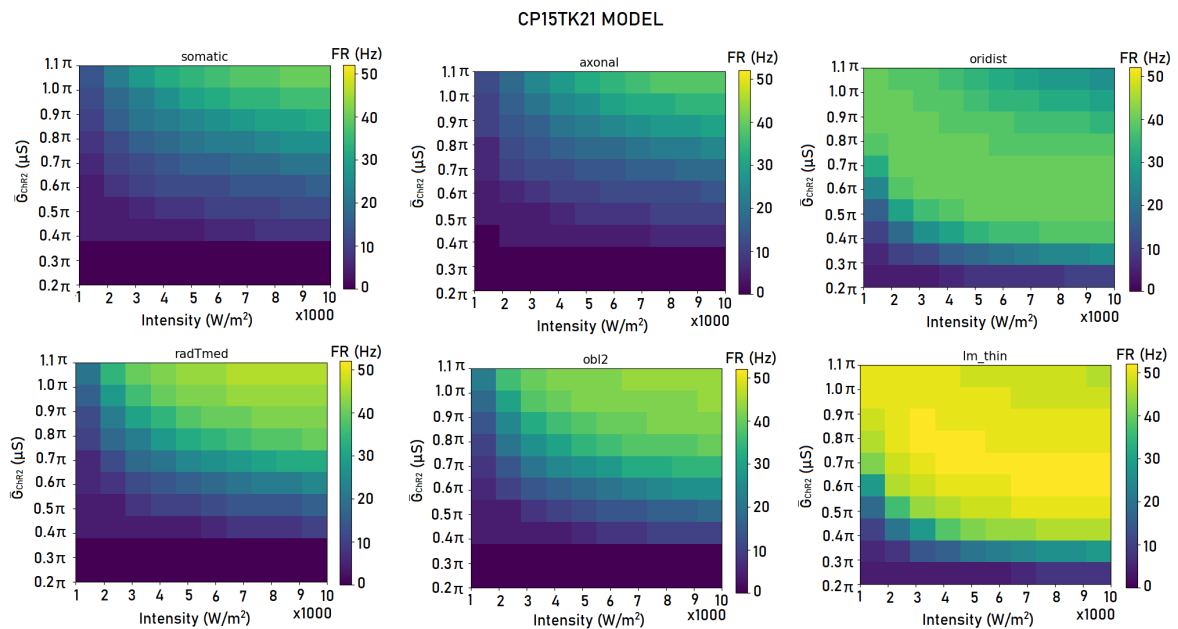


Figure 5.4: 2D colorplots of the mean firing rate, calculated according to Eq. 4.30, in function of the optogenetic pulse intensity and maximal conductance of ChR2(H134R). A continuous pulse of 500 ms is used. The firing rates are recorded in the soma. The CP15TK21 model was used as neuronal model with a normally distributed maximal opsin conductance around the indicated location.

Figure 5.4 is comparable to Figure 4.9 but the maximal specific conductance is now normally distributed instead of uniformly. The y-axis is transformed according to Eq. 4.37. A different results is seen for the axonal stimulation. The FR is not equal to zero anymore but increases with an increasing optogenetic pulse intensity and maximal conductance. It reaches a mean firing rate of 38 Hz. All the other observations made in Section 4.4 for the symmetric diffuse neuronal stimulation, can be copied.

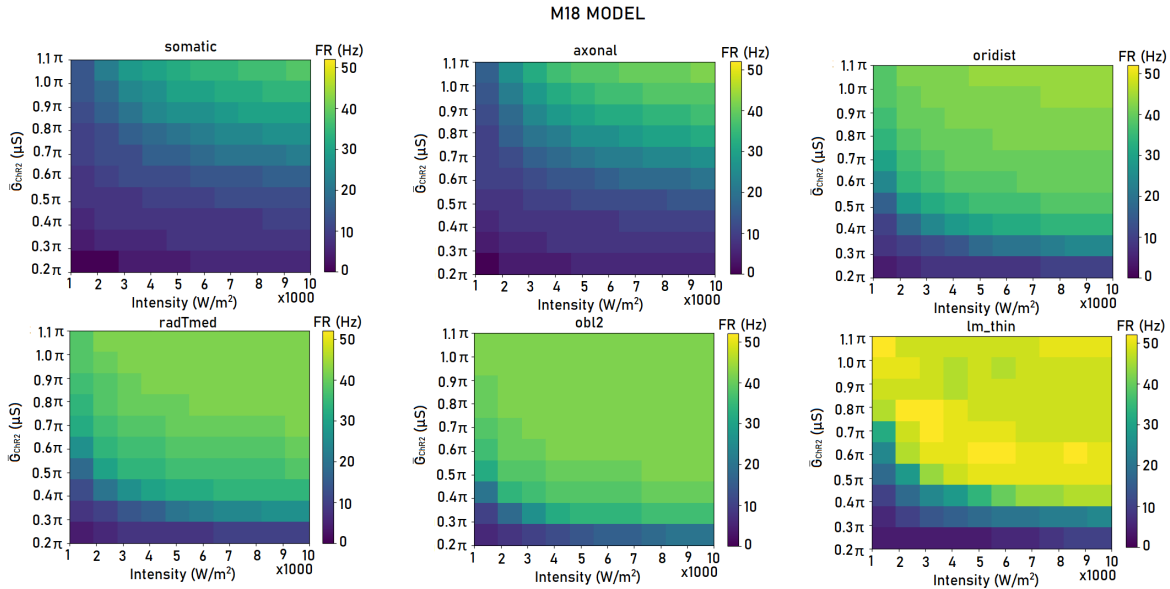


Figure 5.5: 2D colorplots of the mean firing rate, calculated according to Eq. 4.30, in function of the optogenetic pulse intensity and maximal conductance of Chr2(H134R). A continuous pulse of 500 ms is used. The mean firing rates are recorded in the soma. The M18 model was used as neuronal model with a normally distributed maximal opsin conductance around the indicated locations.

The same 2D colorplots were generated for the full-morphology model of Migliore et al. (2018). The overall FR is slightly higher than for CP15TK21. Somatic and axonal stimulation results in very similar mean firing rates. For CP15TK21, stimulation of basal dendrites (oridist) led to a decrease of mean firing rate for higher values of the intensity and maximal conductance. This is not the case for M18, where FR continues to increase. For higher pulse intensities and maximal conductance, stimulation of apical trunk (radTmed) and oblique apical dendrites (obl2) leads to a FR of 42 Hz. There is no further increase. And lastly, the increased FR observed for lm_thin stimulation, is again seen for the M18 model. Compared to the other stimulation locations, the excitability of the neuron is the highest if the opsin is located in the farthest apical dendrite. In general, the mean firing rates are higher when simulations are done with the M18 model but the relative differences between the stimulation locations are preserved.

Membrane potential traces are plotted in Figure 5.6 for a continuous pulse of 5000 W/m^2 and a normally distributed maximal conductance of $0.7\pi \mu\text{S}$. This corresponds to a central point in the 2D colorplots above. Results are obtained for both models and are split over two plots to have a clearer picture of the different spike trains. The voltage traces measured in the soma and axon are shown in (a) and (c) for CP15TK21 and M18, respectively. The firing pattern consists of an initial burst followed by a tonic steady-state firing. The only observed difference between both is the increased firing rate in case of M18. If the opsin is located in one of the four other sections, more activity is measured. The firing patterns are continuous with a slightly higher firing rate in the transient part. The plots are magnified to be able to distinguish the different action potentials. For CP15TK21, the AP amplitude and morphology measured with obl2 and

radTmed as opsin location, are comparable and higher compared to oridist and lm_thin. For M18, the size and morphology of the APs corresponding to obl2 are closer to those of oridist and lm_thin. So, not only the mean firing rates of both models are comparable but also the firing patterns.

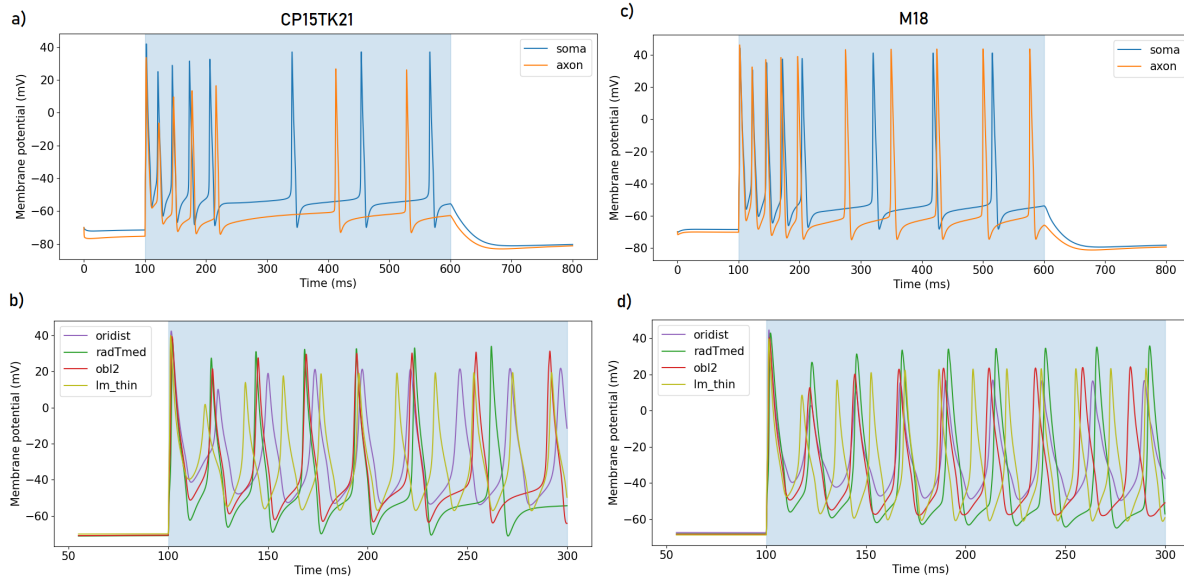


Figure 5.6: The membrane potential (mV) in function of time (ms) with the opsin location indicated in the legend. The membrane potential is measured at the same section. A continuous optogenetic pulse of 500 ms and 5000 W/m^2 , and a normally distributed maximal conductance of $0.7\pi \mu\text{S}$ was used. The optogenetic pulse is indicated with the blue area. The soma and axon are separately plotted. The plot of the remaining sections (b) and (d) is magnified. Plot (a) and (b) are generated with the CP15TK21 model. Plot (c) and (d) with the M18 model. The opsin is normally distributed in both cases.

It was already observed for CP15TK21 that there are differences in propagation time for an AP propagating between a section and the soma. The same was tested for the full-morphology model, which consists of many more sections and branches. Figure 5.7 shows the delay between the first AP measured in the indicated section and in the soma for both models. Three different combinations of stimulation intensity and maximal conductance were tested. In general, the propagation time for an AP traveling from sections at comparable distance from the soma, is higher in the full-morphology model. However, the relative differences between the sections are comparable. The farthest section is the dendritic tuft section (lm_thin) for which the highest delays are measured for both models. The delay is on average 5.2 and 3.9 times higher than the one initiated in the other sections for CP15TK21 and M18, respectively. The ratio of the delay for obl2 and oridist is higher for M18 compared to CP15TK21. Modifying the stimulus intensities and maximal conductance results in slightly higher variations of delays in the M18 model.

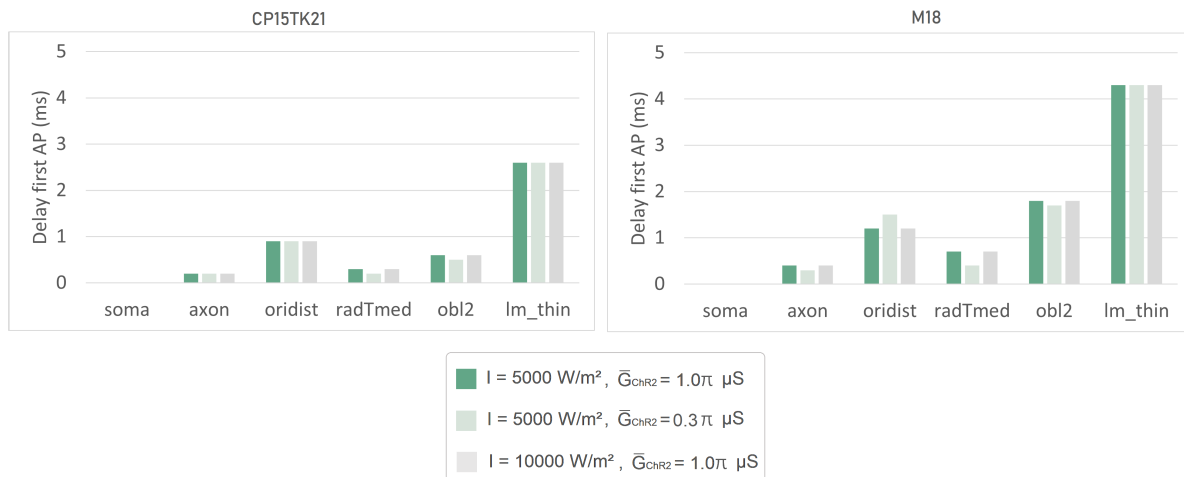


Figure 5.7: Delay between the first AP measured in the indicated section and in the soma. The opsin is located in the same section with a normally distributed maximal conductance of $1.0\pi \mu\text{S}$, $0.3\pi \mu\text{S}$, and $1.0\pi \mu\text{S}$ for the grey, light green, and dark green bars, respectively. The respective optogenetic intensities are 5000 W/m^2 , 5000 W/m^2 , and 10000 W/m^2 . The optogenetic pulse is continuous with a pulse duration of 500 ms.

The strength-duration curves are plotted in Figure 5.8 for both models. A maximal conductance of $0.7\pi \mu\text{S}$ is used. The rheobase intensity and strength-duration time constants are listed in Table 5.2. The rheobase intensities for oridist and lm_thin are again lower compared to the other stimulation locations for CP15TK21. The same was observed in Figure 4.7 for the uniform distribution. However, the difference in rheobase intensities of both sections is higher. The other four sections have again similar values for both parameters. In general, the strength-duration curves of M18 have lower rheobase intensities and higher strength-duration time constants than CP15TK21. Despite the differences of both parameters, there are no pulse durations for which the corresponding intensity is equal for both models. Only the strength-duration curves of the apical dendritic tuft stimulation (lm_thin) are almost identical. For M18, the rheobase for lm_thin stimulation is the highest compared to the other sections. Its value is similar to the rheobase value using the CP15TK21 model but all the other strength-duration curves are shifted downward. In both cases, the same photocurrent was injected but less optogenetic pulse intensity was needed to elicit a spike using M18. This indicates a higher excitability when the CA1 pyramidal neuron is modeled by the M18 model.

Section	M18		CP15TK21	
	I_{RH} (W/m^2)	τ_{SD} (ms)	I_{RH} (W/m^2)	τ_{SD} (ms)
soma	10.02	3.839	30.09	2.323
axon	9.922	3.855	32.19	2.259
oridist	7.023	3.880	13.30	2.643
radTmed	7.883	3.558	36.31	2.206
obl2	8.109	2.950	35.19	2.197
lm_thin	17.78	2.084	17.97	2.067

Table 5.2: The rheobase intensity (I_{RH}) and strength-duration time constant (τ_{SD}) of the strength duration curves in Figure 5.8. A maximal conductance of $0.7\pi \mu\text{S}$ is used.

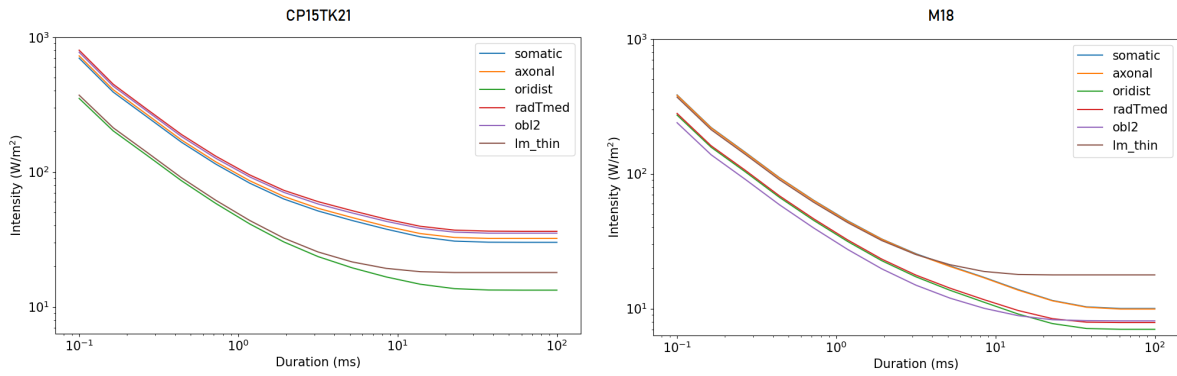


Figure 5.8: Strength-duration curve for different ChR2(H134R) locations and a maximal conductance of $0.7\pi \mu S$, recorded in the soma. The optogenetic pulse duration (ms) of a continuous pulse is shown on the x-axis and the optical pulse intensity (W/m^2) on the y-axis. The neuronal models are respectively the M18 model and the CP15TK21 model for the left and right plot.

The measured input impedances for M18 are shown in Figure 5.9. Input impedances measured in lm_thin and oridist are clearly elevated compared to those measured in the other sections, with mean values of respectively 383.5 Hz and 400.6 HZ. They intersect at a frequency of 34.7 Hz for an input impedance of 384.1 M Ω . Oridist has the highest input impedance for smaller frequencies. The axon, obl2, radTmed, and soma have mean input impedances of respectively 93.84 M Ω , 85.53 M Ω , 56.32 M Ω , and 33.16 M Ω .

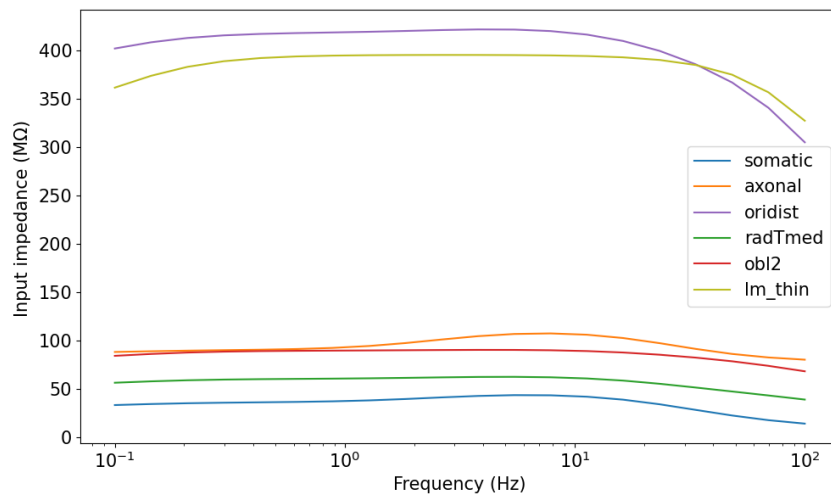


Figure 5.9: Input impedance measured at the indicated location in function of the frequency of the oscillatory current stimulus. It is measured 200 ms after the onset of the stimulus. The M18 neuron model was used.

5.4 Discussion

The transition from a uniform maximal ChR2(H134R) distribution to a normal distribution in CP15TK21 led to a different response on the axonal stimulation. The absence of the depolarization block can be explained by the lower maximal specific conductances. A standard deviation of 125 μm was used so 99% of the available opsin is located within 375 μm from the distal part of the axon. The axon's length is only 150 μm so some of the surrounding sections also get stimulated with small ChR2(H134) conductances. The stimulation is more distributed and the injected current does not lead to a depolarization block anymore. More importantly, the results of this new CP15TK21 model are compared to the full-morphology neuronal model: M18. This model has the same biophysics as CP15TK21 but a lot more dendritic branches. The complexity of the morphology did not influence the main observation: a higher firing rate is measured in the soma in case of apical dendritic tuft (*lm_thin1*) stimulation. This means that this result is independent of the complexity of the model and is likely to be observed in other models. Jarsky et al. (2005) also made this observation in a biophysically simpler and more complex model which leads to the assumption that this result will also be seen in biophysically deviating models. However, the neuron should be modeled as a strong dendritic excitable model. In general, M18 is a more excitable model, leading to higher firing rates for equal optogenetic stimulations. The input impedances were also measured in the concerning sections of M18. The apical dendritic tuft input impedance and distal basal dendritic input impedance were clearly higher compared to the other locations. This affirms the suspicion of Jarsky et al. (2005) that the stimulation of small-diameter branches is efficacious due to the high input impedances. It is remarkable how the input impedances of M18 and CP15TK21 are divergent, yet the same observations are made concerning the efficacious apical dendritic tuft stimulation. This indicates that the effects are not only a result of the increased input impedance, but also of other factors. The delay of the first AP increased on average 89% compared to CP15TK21. However, the sections used to calculate the delay for M18 had slightly deviating distances from the soma than the equivalent sections of CP15TK21 (Table A.3 in Appendix A). The axon of M18 is 52.79 % shorter than the axon of CP15TK21. Nonetheless, the delay measured for M18 was 83.33 % higher than for the longer axon of CP15TK21. The recording sites of M18 corresponding with *obl2* and *lm_thin* of CP15TK21 were respectively only 2.879 % and 5.048 % further away from the soma, yet delays were respectively 211.8 % and 65.38 % higher. This indicates that the difference in distance to the soma is not the cause of the difference in delay. Instead, the complexity of M18, i.e. the higher number of branches and sections, is likely to be the reason for these higher delays. The rheobase intensities obtained by M18 are on average 63.3% smaller than those obtained by CP15TK21. This indicates again that M18 is a more excitable model. Despite the highest mean firing rates, the apical dendritic tuft stimulation results in the highest rheobase intensity of all sections for M18. However, the strength-duration curve of *lm_thin* for $\bar{G}_{\text{ChR2}} = 0.7\pi \mu\text{S}$ is almost identical to the one obtained with CP15TK21. For the other locations, compared to CP15TK21, the strength-duration curves of M18 are shifted downward and there are no intersections meaning that for these locations, M18 is a more excitable model for all pulse durations in case of $\bar{G}_{\text{ChR2}} = 0.7\pi \mu\text{S}$.

Chapter 6

Conclusion

The hippocampus is involved in many cognitive functions such as spatial learning and memory. It also plays an important role in many neurological pathologies. The cornu ammonis 1 (CA1) zone is the main output area of the hippocampus since it sends axonal outputs to over 50 areas in the brain (Takata et al., 2015). Excitation or inhibition of this region can affect many other cortical brain regions which can be used in the treatment of pathologies like temporal lobe epilepsy, or in the study of brain connectivity (Huynh et al., 2020; Takata et al., 2015). Despite its powerful characteristics like cell-type specificity and a high spatiotemporal resolution, optogenetic stimulation of the human brain still faces a lot of challenges. This dissertation aimed at finding optogenetic stimulation strategies that can improve the efficiency of optogenetic excitation of the CA1 pyramidal neuron. The well-known Channelrhodopsin-2 variant ChR2(H134R) was inserted in different locations of the neuron, leading to a spatially localized stimulation of the CA1 pyramidal neuron. The opsin was modeled by the double two-state opsin model of Schoeters et al. (2021) because of its high precision simulations and computational speed. This model was already fitted to and tested on ChR2(H134R).

The model of Cutsuridis and Poirazi (2015), modified by Tomko et al. (2021) (CP15TK21), is primarily used to model the CA1 pyramidal neuron. This model has a simplified morphology but the biophysics are adopted from the full-morphology model of Migliore et al. (2018). Different locations of the neuron were stimulated with a continuous optogenetic pulse of 500 ms for different pulse intensities. The stimulation locations consisted of the soma, the axon, a basal dendrite, an apical trunk dendrite, a radial oblique dendrite, and an apical tuft dendrite. Simultaneous recordings of the membrane potential at the stimulation location and the soma showed that the observed action potentials were initiated at the stimulation locations and could be defined as dendritic spikes. They propagate to the soma and generate somatic spikes. In reality, optogenetic stimulation of subcellular structures of the neuron is possible by genetically modifying the opsin to restrict its expression to desired locations on the neuron. The symmetrical equivalent sections of CP15TK21 have identical morphological and biophysical properties so, in reality, the opsin would be expressed on both sections. For a similar pulse intensity, stimulation of two symmetrical sections compared to one section resulted in higher firing rates and action potentials with increased amplitudes. A comparison of all six stimulation locations led to the conclusion that the symmetrical apical dendritic tuft stimulation resulted in the most efficient excitation of the soma. The highest somatic mean firing rate and lowest rheobase were measured. This section has the smallest diameter of all stimulation locations that were tested. It is located the farthest from the soma, making the results rather unexpected. However, Jarsky et al. (2005) made similar observations when comparing the propagation of dendritic spikes that are initiated in the apical tuft dendrite and upper apical dendrite due to synaptic input. For models with strongly excitable dendrites, apical dendritic tuft input was more efficacious than

upper apical dendritic input. This is comparable to our result, namely, stimulation of the apical dendritic tuft dendrite also resulted in higher mean firing rates compared to apical dendritic trunk stimulation or radial oblique dendritic stimulation. According to Jarsky et al. (2005), this can be a consequence of the high input impedance of the small-diameter tuft branches. However, measurements of the input impedance led to a contradictory result: the soma has the highest input impedance, followed by radTmed, which has the highest diameter of the used sections. So, no correlation is seen between the input impedance and the diameter of the sections. Therefore, other factors will play a role in the elevated activity for apical tuft dendritic stimulation. The computational observations of Jarsky et al. (2005) were also validated by experimental tests. This phenomena is thus also observed *in vitro*.

Next to the model of Cutsuridis and Poirazi (2015), the morphologically more complex model of Migliore et al. (2018) (M18) was used and the tests were repeated. An increased number of sections led to the necessity of working with a normally distributed opsin conductance instead of a uniform distribution. Again, stimulation of the apical dendritic tuft section resulted in the highest mean firing rates measured in the soma. For this model, the apical dendritic tuft input impedance and distal basal dendritic input impedance were clearly higher compared to the other locations. This affirms the suspicion of Jarsky et al. (2005) that the stimulation of small-diameter branches is efficacious due to the high input impedances. However, the results of CP15TK21 showed that the efficacious apical dendritic tuft stimulation is not necessarily a result of higher input impedance so other factors will also play a role. With this more complex model, the rheobase obtained by stimulation of the apical dendritic tuft was the highest instead of the lowest of all sections. In general, the M18 model was more excitable but the results were similar to those obtained by the reduced-morphology model.

It can be beneficial to stimulate small-diameter branches of the neuron with an optogenetic stimulus that is sufficient to initiate dendritic spikes at the stimulation location. Even at higher distances, the initiation of dendritic spikes in small-diameter branches of the neuron results in somatic spike trains with high firing rates. A possible hurdle that can be overcome by these findings is the attenuation of light by brain tissue. If this stimulation strategy is indeed more efficient, less light intensity is needed to obtain a similar spiking output of the CA1 pyramidal neuron.

6.1 Future work

Only one type of optogenetic stimulus was used in this dissertation: a continuous optogenetic pulse of 500 ms. Multiple pulse intensities were used but the pulse duration was kept fixed for all tests. Important to note is that the observations that are made are likely to be a result of the characteristics of dendritic spikes. Therefore it would be interesting to investigate which type, spatial extent, duration, and intensity of optogenetic pulse lead to the generation of dendritic spikes. Gasparini (2006) found that synaptic input has to be synchronous and loosely spatially clustered in order to initiate action potentials in the dendrites. However, Losonczy and Magee (2006) describes how the synchronous and spatially clustered input requirement for dendritic spikes can be circumvented by broad-plateau like events. They can produce both dendritic and somatic spikes. Channelrhodopsin-2 current input can be seen as a broad-plateau like event, especially for longer duration as was used in this dissertation. It is thus possible that the characteristic shape of ChR2 current is beneficial for the initiation of dendritic spikes. Optogenetic stimulation of apical tuft dendrites, or probably more general small diameter branches, seems to be more efficacious and leads to higher firing rates measured in the soma. Next to different types of optogenetic stimuli, different types of neurons can be examined. Population based modeling in which the right variability of neuron types are used, would be even more interesting than focusing on one neuron (Tomko et al., 2021). Another possible extension is the opsin type.

Opsins with different kinetics can have different location-dependent effects on optogenetic stimuli. Lastly, next to the opsin distribution, the illumination can be distributed too. Combining these effects could possibly lead to an even more precise neuronal targeting.

Appendix A

Supplementary tables

Section	Length (μm)	Diameter (μm)	Surface (μm^2)	Number of segments
soma	10	10	100π	1
axon	150	1	150π	5
oriprox1	100	2	200π	3
oridist1	200	1.5	300π	5
oriprox2	100	2	200π	3
oridist2	200	1.5	300π	5
radTprox	100	4	400π	1
radTmed	100	3	300π	3
radTdist	200	2	400π	3
obl1_1	100	4	400π	1
obl1_2	100	4	400π	1
obl2_1	100	2	200π	3
obl2_2	100	2	200π	3
lm_thin1	50	1	50π	1
lm_medium1	100	1.5	150π	3
lm_thick1	100	2	200π	3
lm_thin2	50	1	50π	1
lm_medium2	100	1.5	150π	3
lm_thick2	100	2	200π	3

Table A.1: The section names, lengths, diameters, surfaces, and number of segments of the reduced-morphology model (CP15TK21) corresponding with Figure 4.1 (Cutsuridis and Poirazi, 2015; Tomko et al., 2021).

	Somatic	Axonal	Basal	Apical	Trunk
C_m ($\mu\text{F}/\text{cm}^2$)	1	1	1	1	1
R_A (Ω/cm^2)	115.3958	85.2024	115.3958	115.3958	115.3958
g_{Na} (S/cm^2)	0.0350	0.0350	0.0383	0.0380	0.0250
g_{Kdr} (S/cm^2)	1.50e-03	0.0117	4.30e-03	4.30e-03	0.0200
g_{Kmb} (S/cm^2)	1.00e-03	0.0265	-	-	-
g_{Kca} (S/cm^2)	1.50e-03	-	9.03e-05	9.03e-05	9.03e-05
g_{Kcagk} (S/cm^2)	4.48e-05	-	4.48e-05	4.48e-05	4.48e-05
g_{Cal} (S/cm^2)	5.00e-04	-	8.03e-06	8.03e-06	8.03e-06
g_{Can} (S/cm^2)	2.26e-06	-	2.26e-06	2.26e-06	2.26e-06
g_{Cat} (S/cm^2)	5.00e-05	-	1.18e-07	1.18e-07	1.18e-07
g (S/cm^2)	9.03e-05	1.29e-04	9.03e-05	9.03e-05	9.03e-05
$[\text{Ca}^{2+}]_o$ (mM)	50e-6	-	50e-6	50e-6	50e-6
τ_{Ca} (ms)	100	-	100	100	100
E_{Na} (mV)	50	50	50	50	50
E_{K} (mV)	-90	-90	-90	-90	-90
E_{H} (mV)	-30	-30	-30	-30	-30

Table A.2: The model parameters of the M18 and CP15TK21 model: uniformly distributed passive parameters, active ionic conductances, and reversal potentials of channels for each section (Tomko et al., 2021; Migliore et al., 2018).

CP15TK21		M18	
Section	Distance soma (μm)	Section	Distance soma (μm)
axon	140.0	axon[1]	66.1
oridist	285.0	dend[75]	238.3
radTmed	188.3	apic[19]	192.2
obl2	288.3	apic[24]	296.6
lm_thin	630.0	apic[44]	661.8

Table A.3: The stimulation and recording sites of CP15TK21 and their corresponding distances to the soma. The equivalent sections of M18 that have similar distances to the soma.

Appendix B

Ethics and scientific integrity

For this dissertation, no data was used because it consists of a computational study in which models were used to simulate the response of a neuron to optogenetic stimuli. The models have been validated by the authors based on experimental data to assure high accuracy and simulations that are as close to reality as possible. The neuronal model of Migliore et al. (2018) is based on a set of morphological reconstructions of neurons and somatic voltage traces obtained from in vitro slice preparations of rat hippocampal tissue. The double two-state opsin model of Schoeters et al. (2021) is fit to the data reported by Williams et al. (2013) and the performance is tested by comparing the neural response in a regular spiking neuron and the response obtained by the model derived by Williams et al. (2013). The experimental dataset of Williams et al. (2013) was collected in a ChR2(H134) HEK293 stable cell line and consists of the response of the ion channel to different irradiances and voltages. Their model was experimentally validated by comparison of the results and the ChR2 behavior in guinea pig ventricular myocytes. The neuronal model is based on experiments with rat hippocampal cells while the opsin model is indirectly validated by experiments done using guinea pig ventricular myocytes. This shows the variability in datasets and origin of the cells on which the validation of the different models was based. So, in the interpretation of the results of a computational study, one must always consider the strengths and weaknesses of the model. They are made for a specific study or sometimes tuned for a limited set of experiments. In this dissertation, the influence of the morphology of the neuronal model on the outcome was tested. The simulations done with a morphological simple model were repeated for one that is much closer to a real pyramidal CA1 neuron observed in the human brain. Some of the findings were observed in both cases, however, experimental validation is still needed to really confirm the observations.

The long-term impact of this dissertation would ideally be that the optogenetic activation of cells becomes more efficient by controlling the opsin distribution in a cell. If the findings can be extended to other neuron types, this could potentially be a step forward in the optimization of optogenetic techniques. When all technological hurdles are overcome, optogenetics will evolve to a real therapeutic tool and emerge in the clinic. However, it still requires both the use of gene therapy techniques to introduce the opsin and the implantation of an electronic device to provide optical stimulation. This involves the risk of the neurosurgical intervention needed to access the brain, the risk of an immune response towards the vector and opsin protein, the risk of implant rejection, and many more (White et al., 2020). All in all, risks will certainly be involved so a proper risk assessment should precede the recommendation of this treatment. In the development and optimization of a novel technique that will possibly become available in the clinic one day, also the most extreme scenarios should be covered. What if optogenetics becomes suitable for not only restoring but also extending the brain function of a person? If this technology is able to provide treatment for neurological and psychiatric diseases like autism, aggression or addiction,

would it also be possible to change someone's character or improve someone's cognitive functions? According to Adamczyk and Zawadzki (2020), optogenetics even has a memory-modifying potential including memory enhancement, modification or recovery. Optogenetics can become a powerful yet highly ambivalent neuromodulation technique. There is definitely a need for ethical rules and regulations before it can become an accepted form of treatment for humans.

Optogenetics is one of the fastest-developing neuromodulation technologies (Adamczyk and Zawadzki, 2020). There is a high availability of papers related to this subject, making it difficult to deal with the large amount of information. The CA1 pyramidal neuron, for example, is a well-studied cell so a selection of the most relevant papers was necessary. I listed the information of the interesting ones and processed it all together in one text. If sentences or ideas were used from these papers, the author was mentioned after the sentence(s) and the reference was added to the bibliography at the end of my dissertation. The response of the neuron to an optogenetic stimuli can be analyzed in many different ways. Multiple features describe the morphology of an action potential or the spiking pattern of a neuron so in the comparison of different optogenetic stimulation locations, a selection of features had to be made. Obviously, features that revealed the difference in response to different stimulation locations were chosen above those that didn't. This can be interpreted as including only the successful results. Different intensities and maximal ChR2(H134R) had to be tested to select a range of values for which activity could be measured in the neuron. Simulation settings that resulted in meaningless responses were therefore omitted. Obviously, limiting the extent of the dissertation is the main reason for not including all these results.

Bibliography

- Adamczyk, A. K. and Zawadzki, P. (2020). The Memory-Modifying Potential of Optogenetics and the Need for Neuroethics. *NanoEthics*, 14(3):207–225.
- Bamann, C., Kirsch, T., Nagel, G., and Bamberg, E. (2008). Spectral Characteristics of the Photocycle of Channelrhodopsin-2 and Its Implication for Channel Function. *Journal of Molecular Biology*, 375(3):686–694.
- Bianchi, D., Marasco, A., Limongiello, A., Marchetti, C., Marie, H., Tirozzi, B., and Migliore, M. (2012). On the mechanisms underlying the depolarization block in the spiking dynamics of CA1 pyramidal neurons. *Journal of Computational Neuroscience*, 33(2):207–225.
- Carnevale, N. T. and Hines, M. L. (2006). *The NEURON Book*. Cambridge University Press.
- Carter, M. and Shieh, J. (2015). Chapter 8 - Manipulating Neural Activity. In Carter, M. and Shieh, J., editors, *Guide to Research Techniques in Neuroscience (Second Edition)*, pages 185–201. Academic Press, San Diego.
- Chauhan, P., Jethwa, K., Rathawa, A., Chauhan, G., and Mehra, S. (2021). The Anatomy of the Hippocampus. In Laboratory of Ischemic and Neurodegenerative Brain Research, Mossakowski Medical Research Institute, Polish Academy of Sciences, Warsaw, Poland and Ryszard, P., editors, *Cerebral Ischemia*, pages 17–30. Exon Publications.
- Cutsuridis, V. and Poirazi, P. (2015). A computational study on how theta modulated inhibition can account for the long temporal windows in the entorhinal-hippocampal loop. *Neurobiology of Learning and Memory*, 120:69–83.
- Deleanu, R. (2021). From human pluripotent stem cells to cerebral cortical neurons. In *Recent Advances in iPSC-Derived Cell Types*, pages 69–96. Elsevier.
- Dewell, R. B. and Gabbiani, F. (2018). Active membrane conductances and morphology of a collision detection neuron broaden its impedance profile and improve membrane synchrony. Technical report, bioRxiv. Section: New Results Type: article.
- Fakhoury, M. (2021). Optogenetics: A revolutionary approach for the study of depression. *Progress in Neuro-Psychopharmacology and Biological Psychiatry*, 106:110094.
- Fenno, L., Yizhar, O., and Deisseroth, K. (2011). The Development and Application of Optogenetics. *Annual Review of Neuroscience*, 34(1):389–412.
- Fogwe, L. A., Reddy, V., and Mesfin, F. B. (2022). Neuroanatomy, Hippocampus. In *StatPearls*. StatPearls Publishing, Treasure Island (FL).
- Gasparini, S. (2004). On the Initiation and Propagation of Dendritic Spikes in CA1 Pyramidal Neurons. *Journal of Neuroscience*, 24(49):11046–11056.

- Gasparini, S. (2006). State-Dependent Dendritic Computation in Hippocampal CA1 Pyramidal Neurons. *Journal of Neuroscience*, 26(7):2088–2100.
- Gasparini, S. and Migliore, M. (2013). Action Potential Backpropagation. In Jaeger, D. and Jung, R., editors, *Encyclopedia of Computational Neuroscience*, pages 1–6. Springer, New York, NY.
- Georgiev, D. (2009). Tubulin-bound GTP cannot pump microtubule coherence in stable microtubules: towards a revision of microtubule based quantum models of mind. *NeuroQuantology*, 7:538–547.
- Gerstner, W., Kistler, W. M., Naud, R., and Paninski, L. (2014). *Neuronal Dynamics: From Single Neurons to Networks and Models of Cognition*. Cambridge University Press, Cambridge.
- Golding, N. L., Kath, W. L., and Spruston, N. (2001). Dichotomy of Action-Potential Backpropagation in CA1 Pyramidal Neuron Dendrites. *Journal of Neurophysiology*, 86(6):2998–3010.
- Gradinaru, V., Thompson, K. R., Zhang, F., Mogri, M., Kay, K., Schneider, M. B., and Deisseroth, K. (2007). Targeting and Readout Strategies for Fast Optical Neural Control In Vitro and In Vivo. *Journal of Neuroscience*, 27(52):14231–14238. Publisher: Society for Neuroscience Section: Toolbox.
- Grossman, N., Poher, V., Grubb, M. S., Kennedy, G. T., Nikolic, K., McGovern, B., Palmini, R. B., Gong, Z., Drakakis, E. M., Neil, M. A. A., Dawson, M. D., Burrone, J., and Degenaar, P. (2010). Multi-site optical excitation using ChR2 and micro-LED array. *Journal of Neural Engineering*, 7(1):016004.
- Grossman, N., Simiaki, V., Martinet, C., Toumazou, C., Schultz, S. R., and Nikolic, K. (2013). The spatial pattern of light determines the kinetics and modulates backpropagation of optogenetic action potentials. *Journal of Computational Neuroscience*, 34(3):477–488.
- Grubb, M. S. and Burrone, J. (2010). Channelrhodopsin-2 Localised to the Axon Initial Segment. *PLOS ONE*, 5(10):e13761. Publisher: Public Library of Science.
- Guillaumin, A., Serra, G. P., Georges, F., and Wallén-Mackenzie, (2021). Experimental investigation into the role of the subthalamic nucleus (STN) in motor control using optogenetics in mice. *Brain Research*, 1755:147226.
- Hamada, S., Nagase, M., Yoshizawa, T., Hagiwara, A., Isomura, Y., Watabe, A. M., and Ohtsuka, T. (2021). An engineered channelrhodopsin optimized for axon terminal activation and circuit mapping. *Communications Biology*, 4(1):1–11. Number: 1 Publisher: Nature Publishing Group.
- Hammond, C. (2015). Chapter 19 - The adult hippocampal network. In Hammond, C., editor, *Cellular and Molecular Neurophysiology (Fourth Edition)*, pages 393–409. Academic Press, Boston.
- Hay, E., Hill, S., Schürmann, F., Markram, H., and Segev, I. (2011). Models of Neocortical Layer 5b Pyramidal Cells Capturing a Wide Range of Dendritic and Perisomatic Active Properties. *PLoS Computational Biology*, 7(7):e1002107.
- He, B., editor (2020). *Neural Engineering*. Springer International Publishing, Cham.
- Hegemann, P., Ehlenbeck, S., and Gradmann, D. (2005). Multiple Photocycles of Channelrhodopsin. *Biophysical Journal*, 89(6):3911–3918.

- Hines, M. (1993). NEURON - A Program for Simulation of Nerve Equations.
- Hines, M. L. and Carnevale, N. T. (1997). The NEURON Simulation Environment. *Neural Computation*, 9(6):1179–1209.
- Huynh, T. D., Ashraf, O., Craig, H., Larmeu, L., Barker, B., Stephenson, C., Murcia, D., Howard, B., and Sun, H. (2020). Optogenetic activation of CA1 pyramidal neurons *in vivo* induces hypersynchronous and low voltage fast seizures. preprint, Neuroscience.
- Izhikevich, E. M. (2006). *Dynamical Systems in Neuroscience: The Geometry of Excitability and Bursting*. The MIT Press.
- Jarsky, T., Roxin, A., Kath, W. L., and Spruston, N. (2005). Conditional dendritic spike propagation following distal synaptic activation of hippocampal CA1 pyramidal neurons. *Nature Neuroscience*, 8(12):1667–1676.
- Kiernan, M. C. and Lin, C. S. Y. (2012). Nerve Excitability. In *Aminoff's Electrodiagnosis in Clinical Neurology*, pages 345–365. Elsevier.
- Káli, S. and Zemankovics, R. (2012). The effect of dendritic voltage-gated conductances on the neuronal impedance: a quantitative model. *Journal of Computational Neuroscience*, 33(2):257–284.
- Lewis, T. L., Mao, T., Svoboda, K., and Arnold, D. B. (2009). Myosin-dependent targeting of transmembrane proteins to neuronal dendrites. *Nature Neuroscience*, 12(5):568–576. Number: 5 Publisher: Nature Publishing Group.
- Losonczy, A. and Magee, J. C. (2006). Integrative Properties of Radial Oblique Dendrites in Hippocampal CA1 Pyramidal Neurons. *Neuron*, 50(2):291–307.
- Magee, J. C. and Cook, E. P. (2000). Somatic EPSP amplitude is independent of synapse location in hippocampal pyramidal neurons. *Nature Neuroscience*, 3(9):895–903.
- McDougal, R. A., Morse, T. M., Carnevale, T., Marengo, L., Wang, R., Migliore, M., Miller, P. L., Shepherd, G. M., and Hines, M. L. (2017). Twenty years of ModelDB and beyond: building essential modeling tools for the future of neuroscience. *Journal of Computational Neuroscience*, 42(1):1–10.
- McNally, J. M., Aguilar, D. D., Katsuki, F., Radzik, L. K., Schiffrino, F. L., Uygun, D. S., McKenna, J. T., Strecker, R. E., Deisseroth, K., Spencer, K. M., and Brown, R. E. (2021). Optogenetic manipulation of an ascending arousal system tunes cortical broadband gamma power and reveals functional deficits relevant to schizophrenia. *Molecular Psychiatry*, 26(7):3461–3475.
- Migliore, R., Lupascu, C. A., Bologna, L. L., Romani, A., Courcol, J.-D., Antonel, S., Geit, W. A. H. V., Thomson, A. M., Mercer, A., Lange, S., Falck, J., Rössert, C. A., Shi, Y., Hagens, O., Pezzoli, M., Freund, T. F., Kali, S., Muller, E. B., Schürmann, F., Markram, H., and Migliore, M. (2018). The physiological variability of channel density in hippocampal CA1 pyramidal cells and interneurons explored using a unified data-driven modeling workflow. *PLOS Computational Biology*, 14(9):e1006423. Publisher: Public Library of Science.
- Mogyoros, I., Kiernan, M. C., and Burke, D. (1996). Strength-duration properties of human peripheral nerve. *Brain*, 119(2):439–447.
- Moor, R. and Geit, W. V. (2015). Electrophys Feature Extraction Library (eFEL). page 44.

- Nagel, G., Szellas, T., Huhn, W., Kateriya, S., Adeishvili, N., Berthold, P., Ollig, D., Hegemann, P., and Bamberg, E. (2003). Channelrhodopsin-2, a directly light-gated cation-selective membrane channel. *Proceedings of the National Academy of Sciences*, 100(24):13940–13945. Publisher: National Academy of Sciences Section: Biological Sciences.
- Neher, E. and Sakmann, B. (1976). Single-channel currents recorded from membrane of denervated frog muscle fibres. *Nature*, 260(5554):799–802.
- Nikolic, K., Degenaar, P., and Toumazou, C. (2006). Modeling and engineering aspects of channelrhodopsin2 system for neural photostimulation. *Conference proceedings: ... Annual International Conference of the IEEE Engineering in Medicine and Biology Society. IEEE Engineering in Medicine and Biology Society. Annual Conference*, 2006:1626–1629.
- Nikolic, K., Grossman, N., Grubb, M. S., Burrone, J., Toumazou, C., and Degenaar, P. (2009). Photocycles of Channelrhodopsin-2. *Photochemistry and Photobiology*, 85(1):400–411. eprint: <https://onlinelibrary.wiley.com/doi/pdf/10.1111/j.1751-1097.2008.00460.x>.
- Nikolic, K., Jarvis, S., Grossman, N., and Schultz, S. (2013). Computational models of optogenetic tools for controlling neural circuits with light. *Annual International Conference of the IEEE Engineering in Medicine and Biology Society. IEEE Engineering in Medicine and Biology Society. Annual International Conference*, 2013:5934–5937.
- Petersen, C. (2016). Cellular Mechanisms of Brain Function.
- Poirazi, P., Brannon, T., and Mel, B. W. (2003a). Arithmetic of Subthreshold Synaptic Summation in a Model CA1 Pyramidal Cell. *Neuron*, 37(6):977–987.
- Poirazi, P., Brannon, T., and Mel, B. W. (2003b). Pyramidal Neuron as Two-Layer Neural Network. *Neuron*, 37(6):989–999.
- Ranck, J. B. (1975). Which elements are excited in electrical stimulation of mammalian central nervous system: A review. *Brain Research*, 98(3):417–440.
- Rattay, F., Paredes, L., and Leao, R. (2012). Strength–duration relationship for intra- versus extracellular stimulation with microelectrodes. *Neuroscience*, 214:1–13.
- Rost, B. R., Schneider-Warme, F., Schmitz, D., and Hegemann, P. (2017). Optogenetic Tools for Subcellular Applications in Neuroscience. *Neuron*, 96(3):572–603.
- Sahel, J.-A., Boulanger-Scemama, E., Pagot, C., Arleo, A., Galluppi, F., Martel, J. N., Esposti, S. D., Delaux, A., de Saint Aubert, J.-B., de Montleau, C., Gutman, E., Audo, I., Duebel, J., Picaud, S., Dalkara, D., Blouin, L., Tsiel, M., and Roska, B. (2021). Partial recovery of visual function in a blind patient after optogenetic therapy. *Nature Medicine*, 27(7):1223–1229.
- Schoeters, R., Tarnaud, T., Martens, L., Joseph, W., Raedt, R., and Tanghe, E. (2021). Double Two-State Opsin Model With Autonomous Parameter Inference. *Frontiers in Computational Neuroscience*, 15.
- Spruston, N. (2008). Pyramidal neurons: dendritic structure and synaptic integration. *Nature Reviews Neuroscience*, 9(3):206–221. Number: 3 Publisher: Nature Publishing Group.
- Stamatakis, A. M. and Stuber, G. D. (2012). Optogenetic Strategies to Dissect the Neural Circuits that Underlie Reward and Addiction. *Cold Spring Harbor Perspectives in Medicine*, 2(11):a011924–a011924.
- Stehfest, K. and Hegemann, P. (2010). Evolution of the Channelrhodopsin Photocycle Model. *ChemPhysChem*, 11(6):1120–1126.

- Stern, S., Agudelo-Toro, A., Rotem, A., Moses, E., and Neef, A. (2015). Chronaxie Measurements in Patterned Neuronal Cultures from Rat Hippocampus. *PLOS ONE*, 10(7):e0132577.
- Stujenske, J., Spellman, T., and Gordon, J. (2015). Modeling the Spatiotemporal Dynamics of Light and Heat Propagation for In Vivo Optogenetics. *Cell Reports*, 12(3):525–534.
- Sáray, S., Rössert, C. A., Appukuttan, S., Migliore, R., Vitale, P., Lupascu, C. A., Bologna, L. L., Van Geit, W., Romani, A., Davison, A. P., Muller, E., Freund, T. F., and Káli, S. (2021). HippoUnit: A software tool for the automated testing and systematic comparison of detailed models of hippocampal neurons based on electrophysiological data. *PLOS Computational Biology*, 17(1):e1008114.
- Takata, N., Yoshida, K., Komaki, Y., Xu, M., Sakai, Y., Hikishima, K., Mimura, M., Okano, H., and Tanaka, K. F. (2015). Optogenetic Activation of CA1 Pyramidal Neurons at the Dorsal and Ventral Hippocampus Evokes Distinct Brain-Wide Responses Revealed by Mouse fMRI. *PLOS ONE*, 10(3):e0121417.
- Tomko, M., Benuskova, L., and Jedlicka, P. (2021). A new reduced-morphology model for CA1 pyramidal cells and its validation and comparison with other models using HippoUnit. *Scientific Reports*, 11(1):7615.
- Tung, J. K., Berglund, K., and Gross, R. E. (2016). Optogenetic Approaches for Controlling Seizure Activity. *Brain Stimulation*, 9(6):801–810.
- Tønnesen, J. and Kokaia, M. (2017). Epilepsy and optogenetics: can seizures be controlled by light? *Clinical Science*, 131(14):1605–1616.
- Weiss, G. (1990). Sur la possibilite de rendre comparables entre eux les appareils servant a l'excitation électrique. *Archives Italiennes De Biologie*, 35:413–445.
- White, M., Mackay, M., and Whittaker, R. G. (2020). Taking Optogenetics into the Human Brain: Opportunities and Challenges in Clinical Trial Design. *Open Access Journal of Clinical Trials*, Volume 12:33–41.
- Williams, J. C., Xu, J., Lu, Z., Klimas, A., Chen, X., Ambrosi, C. M., Cohen, I. S., and Entcheva, E. (2013). Computational Optogenetics: Empirically-Derived Voltage- and Light-Sensitive Channelrhodopsin-2 Model. *PLOS Computational Biology*, 9(9):e1003220. Publisher: Public Library of Science.
- Yawo, H., Kandori, H., Koizumi, A., and Kageyama, R., editors (2021). *Optogenetics: Light-Sensing Proteins and Their Applications in Neuroscience and Beyond*, volume 1293 of *Advances in Experimental Medicine and Biology*. Springer Singapore, Singapore.

Influence of the Channelrhodopsin-2 Distribution on Optogenetic Excitability in a CA1 Pyramidal Neuron

Maren Baltussen

Student number: 01702039

Supervisors: Prof. dr. ir. Emmeric Tanghe, Prof. dr. ir. Wout Joseph
Counsellors: Ir. Ruben Schoeters, Dr. ir. Thomas Tarnaud

Master's dissertation submitted in order to obtain the academic degree of
Master of Science in Biomedical Engineering

Academic year 2021-2022

